GOLD AND IRON LOADED MICELLES: A MULTIFUNCTIONAL APPROACH FOR COMBINED IMAGING AND THERAPY, WITH IMPROVED PHARMACOKINETICS

Ajlan Al Zaki

A DISSERTATION

in

Bioengineering

Presented to the Faculties of the University of Pennsylvania

in

Partial Fulfillment of the Requirements for the

Degree of Doctor of Philosophy

2014

_____

Andrew Tsourkas, Ph.D., Associate Professor of Bioengineering - Supervisor of Dissertation

_____

Jason Burdick, Ph.D., Professor of Bioengineering - Graduate Group Chairperson

Dissertation Committee

Jim Delikatny, Ph.D., Associate Professor of Radiology

Andrew Maidment, Ph.D., Associate Professor of Radiology

Jay Dorsey, M.D., Ph.D., Assistant Professor of Radiation Oncology

David Cormode, Ph.D., Assistant Professor of Radiology

This thesis is dedicated to my parents, Waheed Al Zaki and Madonna Irvin

Thank you for supporting me in everything that I aspire to become and everything that I choose to do.
Without their love, guidance, and support this thesis would not have been possible…

AKNOWLEDGEMENTS

I would like to thank my advisor Andrew Tsourkas for always taking the time out of the day to sit down and formulate alternative strategies, for teaching me that failed experiments are often more valuable than successful ones, for giving me the flexibility to pursue new ideas and expand my imagination, for allowing me to reach my full potential, for encouraging me to collaborate with people from various disciplines, and for being an extremely patient. But most of all I would like to thank him for exemplifiying an outstanding teacher, mentor, and scientist. It truly has been a privelage to graduate from his lab.

I would also like to thank all the members of my committee including Jim Delikatny, Andrew Maidment, Jay Dorsey, and David Cormode for their continuous support during my journey to become an independent thinker. Without their guidance, support, and mentorship this would not have been possible.

I would like to thank the Scholarship Coordination Office in The United Arab Emirates for their continuous support and providing me with a fellowship throughout my grauduate school education. It is an honor to be among the selected few to receive this prestigious support.

ABSTRACT

GOLD AND IRON LOADED MICELLES: A MULTIFUNCTIONAL APPROACH FOR COMBINED IMAGING AND THERAPY, WITH IMPROVED PHARMACOKINETICS

Ajlan Al Zaki

Andrew Tsourkas, Ph.D.

Radiation therapy is an important component in the treatment and management of cancer patients. Despite current advances in imaging technologies and treatment planning strategies, a major limitation persists in accurately delineating tumor from normal tissue resulting in radiation-induced damage to healthy structures. Therefore, the frequency and dose of radiation exposure is limited by the generated toxicity in healthy tissues. The use of nanoparticles for contrast-enhanced imaging could improve the accuracy of therapeutic delivery and guide radiation treatments to maximize delivery to disease target tissues while sparing adjacent normal structures. Further, advancements in radiation therapy focus on the use of radiosensitizers that are intended to enhance tumor cell killing while minimizing effects on normal tissue. We have developed multifunctional nanoplatforms, containing sub-nanometer gold and iron nanoparticles that can provide contrast enhancement using computed tomography and magnetic resonance imaging, while also serving as radiosensitizers for X-ray therapy. The effectiveness of these nanoparticles

was evaluated *in vivo* demonstrating an improvement in both tumor margin visualization for image-guided radiation therapy and overall survival in tumor bearing mice. Importantly, we found that measurements of contrast enhancement in imaging correlated strongly with tumor response after radiation therapy. Furthermore, we have found that by encapsulating sub-nanometer gold particles within micelles we are able achieve improved excretion profiles compared to larger gold particles, with gold detected in both urine and feces suggesting that particles within this size range are more efficiently removed by the kidneys and liver. Finally, the use of an actively targeted nanoplatform can achieve higher tumor retention, facilitate nanoparticle internalization, and improve tumor specificity. To facilitate the introduction of targeting molecules onto micelle formulations, a naturally occurring surfactant protein oleosin was used to stabilize superparamagnetic iron oxide clusters. Functionalization with targeting ligands (e.g. Her2/neu affibody) was achieved by fusing the biologically relevant motifs to oleosin using standard cloning techniques, and cell specific targeting was confirmed using magnetic relaxation techniques. In the future, we envision that strategies like this will minimize the off-target effects of radiation, reduce tumor burden, provide information on the likelihood of tumor regression in response to therapy and reduce long-term nanoparticle retention.

TABLE OF CONTENTS

LIST OF TABLES

LIST OF FIGURES

Chapter 1: Introduction to Radiation therapy, Nanotechnology, and Radiosensitizers

1.1 X – Ray Radiation Therapy

The discovery of X-rays in 1895 by Wilhelm Rontgen has paved the way for many advancements in medical imaging. In 1896, Emil Grubbe was one of the first physicians to administer X-rays for the treatment of cancer. Since then there have been many parallels in X-ray imaging and therapy that continues to be an integral component in healthcare. Radiation therapy, an important cornerstone in cancer therapy, is one of the most common and efficient treatments for many types of cancer. It is estimated that approximately 50% of patients diagnosed with cancer will undergo radiation therapy during the course of their treatment.[1] In particular radiation therapy with ionizing radiation (IR) such as X-rays, gamma rays and charged particles are used to cause lethal damage to cancer cells.

For diagnostic imaging, X-rays are generated by accelerating electrons across a potential difference. These electrons leave the negative cathode and strike a positively charged metal target. At the anode, X-rays are created as the electrons strike the metal target losing their kinetic energy either through inelastic scattering with nuclei resulting in the production of bremsstrahlung radiation, or by scattering inner electrons resulting in Auger electrons and characteristic radiation. The energy range of diagnostic X-rays are typically in the range of 10 – 150 kV.[2] X-rays with an energy range of 150-500 kV are called ortho-voltage and occasionally used for the treatment of tissues with depths between 4-6 cm.[3] Megavoltage X-rays, produced by linear accelerators (linacs), contain the highest energies ranging from 1-25 MV and are the most commonly used in

radiotherapy as they have a higher penetration depth (in cm). As a rule of thumb, 80% of the maximum dose lies at a depth (cm) that is roughly one third of the electron energy (MV).

1.1.1 Conventional External Beam Radiation Therapy

A Conventional or two-dimensional radiotherapy arrangement, also known as box radiotherapy, typically consists of one or more beams of radiation delivered to the patient from various directions. Two-dimensional treatment planning is performed using radiation simulators in conjunction with diagnostic X-ray tubes. Using these simulators, the dose distribution is calculated and the treatment fields necessary to encompass the target tissue while sparing normal tissue are determined.[4]

Unfortunately, conventional therapy lacks accurate tissue localization,[5] especially with tissues of complex contours making it difficult to spare radiation doses to uninvolved healthy tissues. As a result, high dose therapies are limited by the radiation tolerability of healthy tissues adjacent to target tumor regions.[6] Furthermore, treatment planning is limited to estimating dose distributions in one or few planes of the patients target volume.

1.1.2 Stereotactic Radiation

Stereotactic radiation is a specialized technique of external beam radiotherapy. In this procedure beams of ionizing radiation coming from various directions converge at a target that is spatially localized in a three-dimensional coordinate system. This is achieved using state of the art computer and imaging systems to guide ablative radiation beams with precision to tumors previously not achievable using conventional external beam therapy.[7]

Stereotactic radiation can be categorized into two different types. The first is stereotactic radiosurgery (SRS), first introduced by a Swedish neurosurgeon named Lars Leksell,[8] which involves the use a single or multiple stereotactic radiation treatments for ailments of the central nervous system. Typically a head frame is fixed to the skull to provide an external three-dimensional frame of reference for precise localization of intracranial radiotherapies.[7] The second is called stereotactic body radiation therapy (SBRT) and is an extension of SRS used to treat extra-cranial diseases.

However there are limitations to stereotactic radiation. About one-third of patients experience potential side-effects immediately post SRS.[9] Furthermore, even with the improved precision of beam delivery, there is the potential for long term side effects ranging from neurological toxicity to death.[10-13] There have also been reported cases of the long-term neuropsychological effects of SRS with patients exhibiting cognitive decline and memory impairment.[14] Another concern of using high-energy ionizing radiation in SRS is the potential risk of radiation-induced malignancies such as glioblastomas.[15-20]

For SBRT applications, immobilization is one critical factor that must be taken into consideration when administering radiotherapy. Tumor motion during respiration can pose challenges exposing surrounding tissues to radiation as the tumor changes position. As a result, several immobilization and positioning strategies are employed such as body frames,[21-23] real time tracking of fiducial makers,[24] and respiratory holding and gating.[25]

1.1.3 3-Dimensional and Intensity-Modulated Radiation Therapy

As the name suggests 3-dimensional conformal radiotherapy (3DCRT) is performed such that the profile of the radiation beams is molded to match that of the shape of the tumor. This can be achieved through the use of specialized planning software and imaging systems such as computed tomography (CT), and magnetic resonance imaging (MRI) enabling physicians to take into account axial anatomy, and complexities in tumor morphology. As this type of treatment conforms to the gross tumor volume (GTV), radiation doses to the tumor can be increased with relatively lower increases in radiation toxicity of surrounding tissue structures. While 3DCRT enabled the planning and delivery of radiation to irregular structures, it is limited in modulating the intensity of radiation within a single field(i.e single uniform intensity).[26-28]

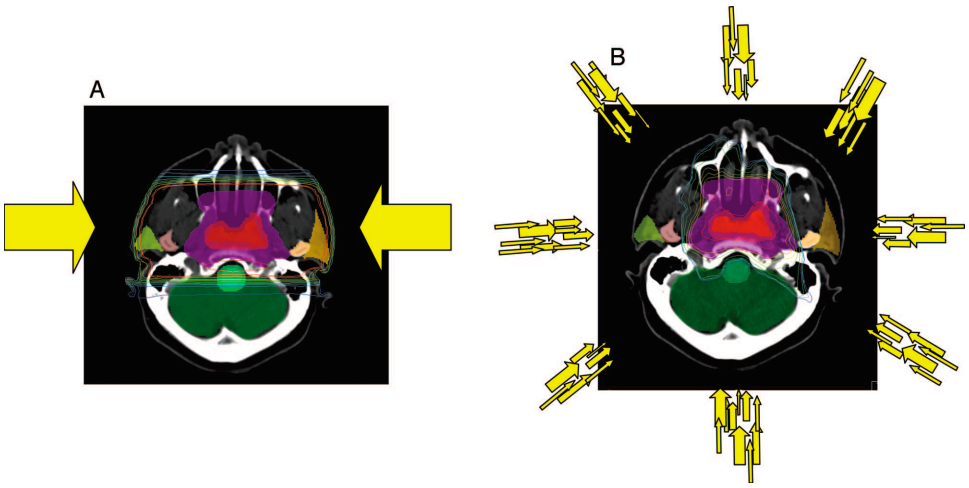

Figure 1.1. (A) Schematic of 2-dimensional radiotherapy showing two beams with single intensities and (B) intensity modulated radiation therapy showing multiple beams with varying intensities applied from any angle.(adapted from Bucci et al.)[5]

Intensity-modulated radiation therapy (IMRT) is an advanced high precision radiation modality that builds on 3DCRT with the ability to customize radiation doses within a single field.[29] Treatment plans are generated using inverse planning software

and computer controlled intensity modulation to produce non-uniform radiation beam intensities throughout the tumor during treatment.[30] Therefore, the radiation dose is elevated within the GTV and minimized or negligible among the neighboring healthy tissue. Therefore IMRT can provide more selective tumor targeting with reduced radiation toxicity as compared to 3DCRT.[31]

1.1.4 Other forms of Radiation Therapy

Gamma rays are also commonly used as a radiation source in the clinic. They are generally produced through decay of radioactive substances (e.g. radium, technetium-99m, cobalt-60). Particle therapy is another emerging technique in the field of radiotherapy and is increasing in popularity worldwide. With X-rays the dose absorbed decreases exponentially as the tissue depth increases. On the other hand, for heavier ions, the dose increases as the particle travels through tissue and loses energy continuously as it starts to slow down (Figure 1.2).

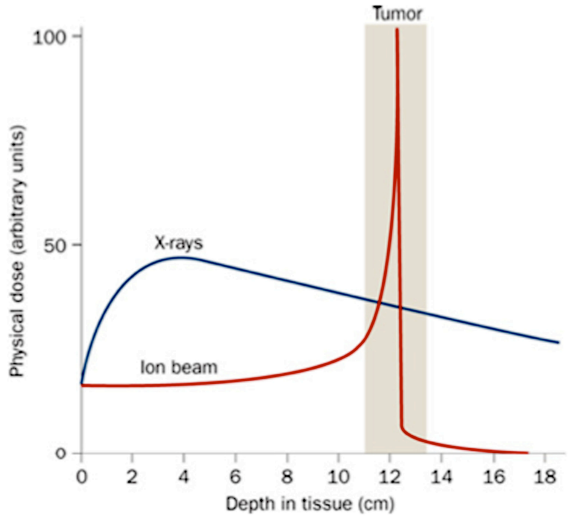

Figure 1.2. Comparison of physical dose as a function of tissue depth for X-rays and high energy particles.(adapted from Durante et al.)[32]

External beam radiation therapy can be carried out using a variety of charged particles including electrons, protons, neutrons, and other heavy ions (carbon, helium, neon).[32, 33] One distinction of this type of therapy from X-rays is the linear energy transfer (LET), which is a measure of the number of ionizations generated per unit distance, and is a function of both charge and velocity. Fast moving light particles have a low LET compared to slow moving heavy particles resulting in reduced biological effectiveness. Compared to X-rays, charged particles have a high linear energy transfer (LET) radiation, that is they deposit larger amounts of energy as they move across a tissue section. Electrons have a finite range after which the dose drops off rapidly and are generally reserved for the treatment of superficial tumors (lymphomas, melanomas) since they poorly penetrate into deep sites within the body.[33] Protons beams produce characteristic dose-tissue absorption profiles called the Bragg peak. Hence the radiation dose increases with increasing tissue thickness up to the Bragg peak occurring near the end of the particle trajectory (Figure 1.2). Beyond the Bragg Peak, the dose drops to zero and can be finely tuned to coincide with target tissues such that the radiation payload is released almost entirely within the tumor while sparing normal healthy tissues. Proton therapy is already used for the treatment of pediatric tumors located adjacent to critical structures where radiation exposure could be detrimental.[34] Neutrons are classified as indirectly ionizing radiation exerting their biological effect almost entirely due to the generation of secondary electrons within tissues. However, they have not gained widespread use due to the difficulty in generating neutrons, and the associated costs.

1.2 Mechanism of Radiotherapy

The primary objective of radiation therapy is to deprive cancer cells of their mitotic potential and ultimately promote cancer cell death. The main interaction of X-rays in cells is by Compton scattering, producing secondary high-energy electrons that exert their effects on biological structures. In the cell, DNA is the desired biological target of ionizing radiation. There are two mechanisms by which radiation can interact with DNA. The first is known as direct action where ionizing radiation interacts directly with DNA to cause damage. The second is known as indirect action where ionizing radiation interacts with the surrounding water molecules, generating free radicals, notably hydroxyl radicals,[35] which cause lethal damage to cellular DNA. Hydroxyl radicals are generated either directly by the oxidation of water by ionizing radiation, or indirectly by the formation of secondary partially reactive oxygen species (ROS). ROS include superoxide (O_2^-), hydrogen peroxide (H_2O_2), and hydroxyl radicals (OH^-). The damage incited can include DNA strand breaks that are initiated by the removal of a deoxyribose hydrogen atom by the activated hydroxyl radical.[36]

Excessive damage to cells exposed to radiation can lead to either double strand breaks (DSB) or single strand breaks (SSB). DSBs are the not the most common type of radiation induced damage but are regarded as the most serious and potentially lethal. At this stage, some cells will arrest their cell cycle to repair the damage. If the damage is beyond repair then the cell will undergo apoptosis. Alternatively, some cancer cells with mutations in cell cycle checkpoints can continue to proliferate following radiation exposure. However, the majority of these cells will undergo cell death during mitosis as a result of sustained DNA damage and chromosomal defects. The post mitotic or

reproductive mode of cell death is considered to be the most prevalent mechanism in cells exposed to ionizing radiation.[37-39] The apoptotic signaling pathway can be initiated in various cellular compartments that include the plasma membrane, cytoplasm and nucleus.[40] In the plasma membrane, ionizing radiation can promote lipid oxidative damage through interactions with radiation induced free radicals resulting in altered ion channels, a build up in arachidonic acid, and the production of ceramide which is involved in mediating cellular death. Cell death occurs via free radical molecules eliciting cumulative un-repairable lipid oxidative damage.[41]

1.3 Types of Cell Death – Cell Response to Radiation Therapy

1.3.1 Apoptosis

Apoptosis, derived from ancient Greek implying "leaves falling from a tree",[42-44] also known as programmed cell death is a regulatory cellular mechanism that eliminates unwanted cells occurring during embryonic development, cellular regeneration, growth and differentiation.[42] It is characterized by specific morphological events such as cell shrinkage as the cytoskeleton is broken down, chromatin condensation, DNA fragmentation, membrane blebbing and the formation of apoptotic bodies as the cell breaks apart.[45] Apoptosis can also be characterized by biochemical events (elevated TNF cytokines, activated caspases, mitochondrial release of apoptosis-inducing factor).[46-48] Physiological or pathological stress factors such as receptor mediated processes, oxidative stress, chemotherapeutic drugs and radiation can trigger apoptotic signaling pathways.[49, 50]

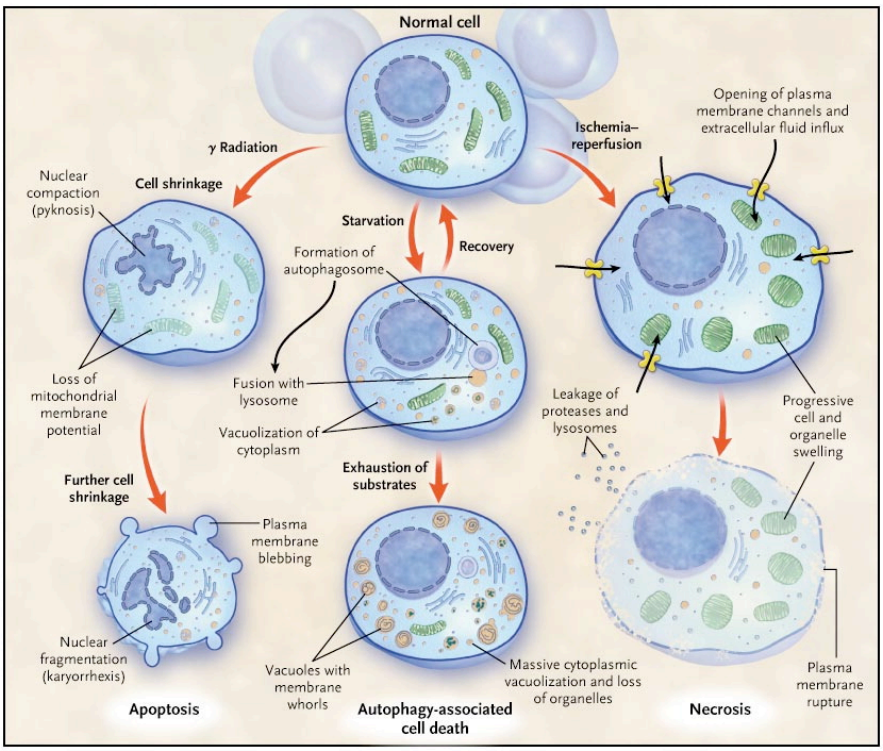

Figure 1.3. Three Pathways of Cell Death. Among the three major pathways of cell death — apoptosis, autophagy, and necrosis — a particular mode of cell death may predominate, depending on the injury and the type of cell. Cross-talk among the different types of cell-death pathways exists at multiple levels and is not shown.(adapted from Hotchkiss et al. [51])

Radiation induced apoptosis is regarded as a significant component in the mechanism of cell death after exposure to ionizing radiation.[49] Further findings suggest that plasma membrane damage may activate intracellular transduction pathways that are responsible for the regulation of the apoptotic pathway.[52, 53] In the cytoplasm, ionizing radiation can generate cytosolic stimuli such as reactive oxygen intermediates, and Bcl-2-associated X protein that can induce mitochondrial damage that activates mitochondrial release of caspase-activating factors promoting apoptosis.[54] In response to radiation-induced nuclear DNA damage, tumor suppressor protein p53 is activated which halts cell cycle progression allowing DNA repair to take place prior to replication and cell

division.[55, 56] However, if DNA repair is unsuccessful, p53 may trigger cell death through apoptosis. *In vivo*, apoptosis is generally seen as individual cells that are subsequently phagocytosed by macrophages or neighboring cells.[57]

1.3.2 Mitotic-Linked Death

Numerous studies quantitatively comparing apoptotic death with mitotic-linked death in irradiated cells have shown that the primary mechanism of cell death is associated with mitotic catastrophe.[50] Specifically, this type of cell death occurs during or after abnormal mitosis, characterized by various morphological changes such as missegregated chromosomes, multinucleated giant cells and resulting in cell death.[58] Combined apoptosis and mitotic-linked cell death account for most of the ionizing radiation induced cell death.[33]

1.3.3 Senescence

Another mechanism of cell death in response to radiotherapy is known as senescence which is a cellular processes that results in an irreversible cell cycle growth arrest.[59] These cells are viable and primarily characterized by a reduction in proliferative capacity, no longer synthesize DNA, acquire distinct changes in shape by flattening out with an increase in cytoplasmic vacuolization, and can be identified biochemically by an increase in senescence associated β-galactosidase (SA-β-gal) activity.[60]

1.3.4 Necrosis

Necrosis, originating from Greek “necros” for corpse, differs from apoptosis in cells exposed to ionizing radiation by the loss of plasma membrane integrity prior to randomized DNA degradation.[57] In necrosis, there is a characteristic swelling of cells and their organelles, which is a consequence of an early disruption in membrane intactness

allowing the influx of extracellular ions and fluid.[51] Ultimately, plasma and organelle membranes swell so much that they rupture allowing lyososomal proteolytic enzymes to escape into and out of the cytosol causing cellular damage.[61, 62] Generally, necrosis is initiated in events associated with metabolic stress such as the rapid depletion of ATP that can occur in ischemic scenarios.[63, 64] Although not as frequent, necrosis can also occur in irradiated cells mediated by the generation of reactive oxygen species.[33] *In vivo*, necrosis usually presents as clumps of cells surrounded by an infiltrating inflammatory response resulting from intracellular release of compromised cells.[65]

1.3.5 Autophagy

Autophagy, originating from Greek self "auto" and eating "phagy", is another type of programmed cell death in which the cell eats itself. It is characterized by the presence of autophagosomes,[61, 66] double membrane vacuoles that engulf cytosolic proteins and organelles, which are delivered to and fused with lysosomes for degradation.[67, 68] The autophagic response in cells receiving ionizing radiation is controversial.[69] Recently, this mechanism of cell death has been reported in irradiated cancer cells lacking various apoptotic regulators.[70, 71] However, autophagy may also elicit a protective mechanism against radiation-induced injury by sequestering damaged proteins and organelles.[72]

1.4 Radioresistant Cancer Cells

Although ionizing radiation is an integral component in antineoplastic management and control, malignancies resistant to radiation often relapse and continue to pose major challenges and limitations to this type of therapy. During the early 20th century, Bergonié and Tribondeau proposed radioresistant cells are characterized by a high mitotic rate, evade normal cellular senescence, and have an undifferentiated phenotype.[3] More recently, this has been attributed to cells in metabolic statuses associated with high levels of free radical scavengers, low proteosome activation and activated DNA checkpoints.[73]

Originally described by Withers, the fundamental principles of radiobiology, also known as the "four R's", help to explain some mechanisms for cells that are resistant to radiation damage. These are: repair, redistribution, repopulation and reoxygenation.[73]

1.4.1 Repair

Chromatin is the molecular complex that contains nuclear DNA within the cell and is composed of nucleosomes that play an important role in providing structure and function in DNA packaging. The nucleosome is made up of a base pair strand of DNA that is wound around eight histone protein cores (a pair of H4, H3, H2B, and H2A). Evidence suggests that the nucleosome is not only involved in the essential packaging of DNA, but also in the regulation of information transfer from DNA including transcription, meiosis and mitosis, and the maintenance of genomic integrity.[74-76] Specifically, these functions are carried out through the modification of specific amino acid residues on histones.[74]

The H2A histone family member X (H2AX) is involved in the localization and repair of DNA DSBs. One of the hallmarks in radiobiology for DNA DSB, occurring

within three minutes after irradiation,[77] is the phosphorylation on serine 139 of H2AX, primarily by the kinases ataxia telangiectasia mutated (ATM), ataxia telangiectasia and Rad3-related protein (ATR).[78] This phosphorylation at the specific serine site is called γ-H2AX and it is believed that phosphorylation decondenses DNA providing repair proteins space during recruitment. γ-H2AX nuclear foci can be quantitatively determined immunohistochemically using an antibody to the phosphorylated serine of γ-H2AX. Furthermore, the extent of DSBs is proportional to the number of γ-H2AX foci with each foci corresponding to a single DSB.[79, 80] Several groups have shown that resistant cancer cell lines tend to have lower γ-H2AX foci and appear to resolve faster after radiation.[81, 82] In this thesis, I use the γ-H2AX assay to quantify the amount of DSBs in cells lines the presence or absence of X-ray radiation therapy.

A considerable amount of cell death is based on the ability of ionizing radiation to inflict sufficient damage to induce un-repairable DSBs. However, at low doses the majority of radiation induced DNA damage is sublethal enabling cells to repair the breaks and proliferate. The interaction of ionizing radiation with water molecules generates reactive oxygen species (ROS) that rapidly interact with molecules in cells. These ROS generated are more efficient in causing DNA damage than the direct interaction of DNA with ionizing radiation.[73] Therefore the presence of free radical scavengers within the cell is a major determining factor on the fate of irradiated cells. A study on $CD24^{-/low/}CD44^{+}$, a breast cancer cell line with low levels of ROS and high free radical scavengers, was found to have low levels of DSBs with increased tumorigenicity.[83] Further studies verify this hypothesis by reversing radiation resistances after the depletion of glutathione, an important intracellular free radical scavenger.[84] Thus, the level of radiation generated

ROS within a cancer cell may help in determining the responsiveness to radiation. In glioblastomas, Bao et al. showed that $CD133^+$ cancer stem cells can become radioresistant by activating DNA damage checkpoints that increase their ability to repair DNA.[85] Other groups have proposed alternative mechanisms of radioresistance, such as increased autophagy related proteins in $CD133^+$ cells after irradiation as alternative explanations for their radioprotective mechanisms.[86]

1.4.2 Redistribution

The resistance to radiation damage is determined largely by what phase of the cell cycle a cell is experiencing, with cells in mitosis being the most sensitive to DSBs and cells in the S phase being the least sensitive.[87] This is modulated by the activation of cell cycle checkpoints, which can be induced in the G_1, S, and G_2 phases of the cell cycle, to allow the cell to repair possible defects. Therefore, attempts to synchronize tumor cells in a specific phase of the cell cycle are regarded as a potentially beneficial strategy to enhance the efficacy of radiation therapy.[88-90]

After a dose of radiation, most surviving cells will be those that were in the S phase of the cell cycle (Figure 1.4). Sufficient time must be allowed for cells to redistribute before another dose is administered. This timed treatment, termed dose fractionation, allows the redistribution of cells in radioresistant phases of the cell cycle into more sensitive phases and is especially therapeutically beneficial for slower cycling tumor cells.[91]

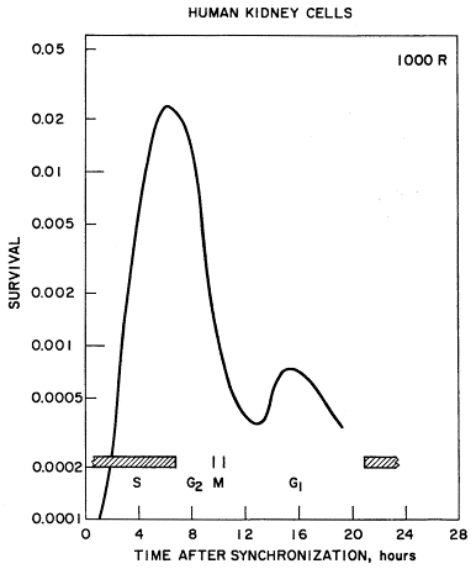

Figure 1.4. Synchronized human kidney cells show a differential survival depending on cell cycle phase in which they are irradiated. Cells are most sensitive to irradiation during mitosis and in G2, less sensitive in G1, and least sensitive during the latter part of S phase.(adapted from Sinclair et al.)[92]

1.4.3 Repopulation (Regeneration)

The concept of cellular repopulation is an important biological predictor of clinical outcome of fractionated radiation therapy.[93, 94] The administration of radiation therapy is usually divided into multiple doses and spaced out over several weeks. This strategy provides normal tissues with some time to recover and regenerate during prolonged treatment regimens. Although this temporal modulation of therapy allows normal cells to repopulate, repopulation of cancer cells also occurs, increasing the number of cells that need to be eliminated. It is this process of cancer cell proliferation that is one of the main causes of treatment failures in radiation therapy.[95]

There are numerous studies that suggest accelerated repopulation during fractionated radiation therapy in humans. In squamous cell carcinomas of the head and neck, it was shown that the total radiation doses required to control 50% of tumors

(TCD_{50}) increased when the treatment lasted more than 4 weeks.[96] Furthermore, the doubling time of these cancers cells decreased from 2 - 3 months to 4 days after radiation therapy. Other studies demonstrate that for every daily increase in the duration of therapy, the likelihood that tumors will grow out of control increase by 1 – 1.5%, and the radiation dose required to combat repopulation increases by about 0.5 – 1 Gy.[97-99] Hence there may be detrimental effects of prolonging treatment time for tumor control but this may be tumor specific.

Clinical outcomes could potentially be improved by attempts to inhibit or limit repopulation during radiotherapy. This can be achieved by using a modified dose-schedule of treatment. Accelerated fractionation is a fractionation technique that shortens the overall treatment time, to minimize tumor growth during treatment and prevent tumor cells from repopulating.[96, 100] This strategy has shown promise in tumor control for both Burkitt's lymphoma and squamous cell carcinomas of the head and neck.[101-103] Other studies comparing accelerated therapies and conventional therapies have concluded that the accelerated schedule leads to an improvement in tumor control and overall survival.[104, 105]

1.4.4 Reoxygenation

The level of oxygenation of a tumor is a major determinant of the effectiveness of radiation therapy. Numerous studies have shown that poorly perfused hypoxic tumors are two to three times more resistant to radiation and are associated with poor prognosis and recurrence.[106-110] This phenomenon is known as the oxygen enhancement ratio. Within a tumor there is a dynamic and heterogeneous distribution of oxygen levels that exist largely because of insufficient vascularization and unevenness of supporting stromal

tissue.[111] Oxygen is thought to behave as a direct radiosensitizer, inflicting DNA damage through the generation of free radicals. Specifically, according to the "oxygen fixation" hypothesis, exposure of ionizing radiation generates free radicals in water and DNA. The DNA formed free radicals are able to react with O_2 to generate peroxy radicals, modifying the DNA by fixing O_2. However, if O_2 is absent, the DNA free radical will be reduced to its original form.[112]

Strategies focusing on increasing tumor oxygenation through the use of hyperbaric O_2,[113, 114] erythropoietin infusions,[115, 116] and red blood cell transfusion have been attempted.[117] Unfortunately these approaches did not gain widespread clinical use since these techniques are difficult to implement and studies were inconclusive. Furthermore, the use of nitroimidazoles that mimic the effect of O_2 are associated with dose-limited toxicities.[118] More recently, alternative strategies have been aimed at selectively killing hypoxic tumor cells by using drugs that are known to be cytotoxic for cells in hypoxic environments.[119] Tirapazamine is one example of a an anticancer drug that is readily reduced in hypoxic cells, forming free radicals that give rise to DNA DSBs in a topoisomerase II dependent fashion.[120] The specific mechanism of action is uncertain but it is hypothesized that the drug acts a substrate for intracellular reduction. In the presence of O_2, the drug radical transfers its electron to molecular oxygen forming superoxide and regenerating the initial drug. However, in the absence of O_2, the drug radical accumulates and can either itself cause cytotoxic damage or undergo further reactions to generate more substantial toxins.[120] Clinical trials with this compound demonstrate therapeutic efficacy in patients with head and neck cancer or non-small cell lung cancer.[121, 122]

1.5 Clonogenic Assays

A clonogenic cell is a term that is given to a single cell that is capable of proliferating and producing a substantial number of progeny. The radiation sensitivity of this cell is experimentally determined using an *in vitro* clonogenic cell survival assay or colony formation assay.[123, 124] This type of assay is the gold standard in determining cell reproductive death after radiation therapy and describes the relationship between the radiation dose with the fraction of cells that survive. This type of assay can also be used to assess the tumoricidal effectiveness of other cytotoxic agents. Generally, cells are seeded into culture dishes before or after irradiating at different doses and allowed to form colonies between 1 – 3 weeks. After this time has elapsed, the colonies are fixed, stained with crystal violet, and counted using a light microscope. Clonogenic assasys were used in this thesis to assess the *in vitro* survival of cell lines in response to various doses of X-ray radiation in the presence or absence of the radiosensitizer.

Colonies with less than 50 cells are not counted for the survival calculation. These cells may be physically present and struggle through 2-3 cell divisions, but if they have lost the capacity to divide indefinitely and produce small colonies (< 50), then they are by definition dead. On the other hand, surviving cells are those cells that have retained their reproductive potential and proliferate indefinitely producing large clonogenic colonies. It is these colonies that are included in the survival analysis.

A survival curve is a plot of the fraction of surviving cells on a logarithmic scale against the cumulative radiation dose on a linear scale. At low doses, survival curves typically have an initial shoulder representing an accumulation of sublethal damage. As the radiation dose increases, the curve bends as the surviving fraction exponentially

decreases with further dose increments. The type of cell undergoing ionizing radiation, recovery from sublethal injury, reoxygenation of hypoxic cells, redistribution of the cell cycle and repopulation all affect the survival curve.

1.6 Complications from Radiotherapy

While the pathological mechanisms of radiation injury begin immediately following radiation therapy, the clinical and histological signs may take days, weeks, months or even years after administration. For example, changes in the lung 6 weeks after high dose therapy are mild compared to widespread fibrosis detected 6 months later.[6] The tolerance of normal tissues to radiation varies and dictates the dose that is prescribed in a specified treatment regimen. Thus, an important distinction in radiation injury that must be taken into account is the difference between early and late effects of normal tissues.

1.6.1 Acute (Early) Effects

Acute or late effects are a form of radiation induced normal tissue damage that usually presents weeks after therapy. This type of radiation damage is most pronounced in tissues with cell populations that are rapidly proliferating such as skin or mucosal membranes. Symptoms arise when functional cells are compromised as part of cell death and not regenerated. Some cells such as those in skin and the alimentary tract are generally more tolerant to radiation and usually heal rapidly. As a result, acutely developed symptoms are often self-limiting over the course of radiotherapy.

Other acute reactions, such as edema and erythema, can arise from mechanisms that do not involve cell death. For example, ionizing radiation may activate multiple cellular signaling pathways that stimulate pro-inflammatory cytokine release,[125-127] down-regulate physiological anticoagulants,[128] and cause organ damage secondary to vascular injury.[129] These reactions may be responsible for the initiation of an inflammatory response, increased vascular permeability leading to swelling, and the activation of the coagulation cascade.

1.6.2 Chronic (Late) Effects

Unfortunately, radiation is the gift that keeps on giving. Late effects are described as radiation induced normal tissue damage occurring months, years or even decades after radiation exposure.[130, 131] The severity of symptoms vary, developing suddenly or gradually over time, and are generally associated with tissues of cell populations with slow turnover, such as brain, bones, muscle, kidneys, and liver.[6] The underlying mechanisms behind late effects are multifactorial and poorly understood, but it is believed that damage to vasculature and immune reactions are main components in exacerbating late effects including lesions such as fibrosis, necrosis, atrophy, and fractures.

Radiation induces blood vessel injury resulting in increased permeability and vasoactive cytokine release.[132-134] This allows fibrin in the bloodstream to extravasate out into surrounding tissues promoting collagen formation.[126, 135] In addition, activated lymphocytes in the circulation can adhere to damaged endothelial cells and narrow the lumen restricting blood supply to downstream cells.[6]

1.7 Radiation Dose Fractionation

Fractionation is a technique of treating malignancies with radiation therapy. In this strategy the total dose of radiation to be administered is divided into several discrete dose fractions and is often delivered over period of five to seven weeks. Conventional fractionation is typically delivered once a day on weekdays at a dose per fraction of 2 Gray. This schedule of five fractions per week allows the recovery of normal cells from radiation damage thereby avoiding severe toxic reactions and maximizing the effect of radiation on cancer cells while minimizing off target toxicity.[95] In general when more than one fraction is administered per day, an inter-treatment interval of at least 6 hours should be used. The benefit of this approach has been demonstrated with *in vivo* studies, which have concluded that five daily fractions of 2.5 Gy result in higher levels of apoptosis than either a single dose of 25 Gy or two fractions of 12.5 Gy separated by 5 days.[136] Their rationale is that after each fraction of radiation, a new subpopulation of radiosensitive cells is primed for radiation-induced apoptosis. Numerous other reports are consistent with these findings.[137, 138]

Various dose fractionation strategies can be designed by adjusting either the treatment duration or the radiation dose received per fraction. Most strategies however, avoid increasing the dose per fraction, as these are associated with poor tolerability and increased toxicity.[96]

1.7.1 Hyperfractionation

Hyperfractionation, is when the total radiation dose is divided into small doses (smaller than conventional i.e 1.15 – 1.25 Gy) while keeping the duration of therapy constant (treatments are given more than once a day). Patients selected for

hyperfractionation therapy are those where treatment is limited by the dose tolerance of late effect tissues. The rationale behind hyperfractionation is differential repair, in that slowly responding tissues have a greater capacity of repairing sub-lethal damage (at reduced dose fraction) than tumors. By significantly reducing the size per fraction and increasing the number of fractions, resistant cells are allowed to redistribute themselves through the cycle increasing the likelihood that they are in a relatively more radiosensitive state by the next cycle.[139, 140] However, redistribution also occurs in normal cells and so no therapeutic benefit will be observed relative to acute normal tissue responses. Cells responsible for late reactions tend to be slower cycling normal cells or late responding tissues and are less sensitive to redistribution resulting in lower late toxic events for a given level of tumor control.

1.7.2 Accelerated Fractionation

Patients whose tumors have a high proliferative capacity such as Burkitt's lymphoma and inflammatory carcinoma of the breast may benefit from accelerated fractionation.[139] This regimen uses shorter treatment durations while maintaining similar doses as conventional radiation therapy. It often involves fewer than ten fractions per week, but any number above five per week will accelerate the treatment time. For example, a patient may receive seven 2 Gy treatments over the course of 5 days or be treated 6 days a week. The main objective of this treatment strategy is to limit growth of rapidly proliferating cells by applying radiation treatments with shortened inter-treatment intervals in order to reduce the ability for tumor cell regeneration.[96, 139] As this treatment is accelerated, acute tissue toxicity can be worse, limiting the tolerance dose. Thus, on days with multiple treatments, fractionation intervals must be as long as possible to allow

repair of sub-lethal damage in slowly responding tissues and maximize the redistribution of tumor cells. Also, because the fraction size remains unchanged, one would expect little or no changes in slowly cycling cells for late responses especially since these cells do not undergo rapid repopulation.

1.7.3 Accelerated Hyperfractionation

This strategy aims to improve the therapeutic ratio by combining both accelerated and hyperfractionated treatment protocols. Here there is a decrease in both the dose received per fraction, typically higher than hyperfractionation but lower than conventional dose fractions, and the total treatment duration. However this approach is limited by acute tissue toxicity as both of these strategies independently increase early tissue responses necessitating breaks between fractions. Clinical trials comparing continuous, hyperfractionated accelerated radiotherapy (CHART) with conventional radiotherapy demonstrate a statistically significant improvement in the survival of patients with locally advanced non-small cell lung cancer.[141, 142]

1.7.4 Hypofractionation

Historically, there were two main reasons for the introduction of clinical hypofractionation. First, increased demand for radiotherapy and a shortage of treatment units meant that patients received larger but fewer fractions so more patients could be treated over time. Second, this strategy could lower the burden on patients who would not have to frequent the hospital on a daily basis for several weeks.[143, 144] With hypofractionation the total dose of radiation is divided into doses that are larger than conventional therapies (> 2 Gy). A larger dose fraction results in a shortened treatment period counterbalancing the principal disadvantage of delivering large fraction sizes. The

therapeutic benefit of hypofractionation is controversial with many studies raising concerns of injury,[145, 146] and little evidence to support its superiority to conventional methods.[147] However recently, Whelan and colleagues demonstrated that accelerated hypofractionated whole breast irradiation was on par with standard radiation treatment in women who had undergone breast conserving surgery for invasive breast cancer.[148] The implications of this study is that it will conserve large amounts of time and money for patients while maintaining similar outcomes and side effects as the current standard.

1.8 Limitations of Radiation therapy

The overall objective of radiation therapy is to maximize the dose of total radiation delivered to the tumor. In theory, achieving a tumoricidal dose of radiation can be achieved by exposing the tumor to large doses of radiation. However, this comes at the expense of exposing surrounding normal tissues within the treatment boundaries ultimately limiting the radiation doses that can be utilized. In general late tissue effects are sensitive to changes in fraction size,[140] while early tissue effects are more sensitive to overall treatment time.[149] Furthermore, there is patient-to-patient variability in the severity of side effects after a session of radiotherapy, which can usually never be predicted prior to treatment. As mentioned previously, these side effects can either subside over time or limit future radiotherapy exposures. For example, patients with genetic mutations like ataxia telangiectasia present with serious radiation reactions due to repair in DNA after radiation exposure.[150, 151] Moreover, ionizing radiation can be carcinogenic with the possibility of malignancies developing when patients are exposed to either diagnostic or therapeutic doses of radiation. However, patients receiving higher doses of radiation are at most risk for radiation-induced malignancies. Many studies have reported patients developing second malignancies after receiving radiotherapy.[152-155] Finally, through technological advances and image guided radiotherapy, geometric radiation targeting can be administered with high precision, however, a major limitation is the treatment of microscopic lesions and tumor margins that can be very difficult to detect. While most of these techniques incorporate CT, MR and/or other imaging techniques, there are no tools that measure the biological change or healthy tissue function during the course of radiotherapy. Such advances in functional imaging using

MRI and PET may lead to improvements in radiotherapy planning and tumor responses while minimizing off target effects.[156]

1.9 Radiosensitizers

Since current irradiation strategies may fail to kill all cancer cells within an irradiation volume, it may be beneficial to selectively enhance radiation at the cellular level. Consequently, many approaches have been developed to enhance the radiation effects specifically within tumors. A radiosensitizer is an agent or drug that increases the cytotoxic susceptibility of cancer cells to radiation therapy. Ideally a radiosensitizer would act specifically on tumor cells sparing normal tissues, have favorable pharmacokinetic profiles for tumor accumulation prior or during radiation therapy, and be nontoxic.

In general radiosensitizers can be categorized into five groups: (i) oxygen mimicking agents, (ii) sensitization by the structural incorporation of thymine analogues into DNA, (iii) inhibitors of cellular repair processes and cell signaling processes, (iv) agents that suppress intracellular thiols or other free radical scavengers, and (v) agents that generate cytotoxic substances via radiation interaction with sensitizer.[157]

1.9.1 Oxygen Imitators

Oxygen, one of the most important physiological radiosensitizers, has two unpaired electrons that can rapidly add to other free radicals to generate new reactive radicals that can cause DNA strand breaks. Many approaches have attempted to take advantage of this by increasing the oxygen supply to the tumor. Hyperbaric oxygen was one of the earliest strategies to be used clinically that demonstrated the value of increasing blood oxygen levels, however, difficulties in simultaneous application of hyperbaric oxygen and radiotherapy, as well as severe tissue radiation injury have limited their clinical use.[158] Studies using efaproxial, a

drug that non-covalently interacts with and lowers the affinity of hemoglobin for oxygen thereby increasing the partial pressure of O_2 in tissues and tumors, demonstrates an increase in responsiveness for patients with brain metastasis.[159] Furthermore, vasoactive agents such as nicotinamide in combination with carbogen (95% oxygen and 5% carbon dioxide) that are capable of eliminating acute hypoxia have shown promise in some clinical studies.[160]

Nitroimidazoles are an electron affinic (i.e ability to capture electrons) class of drugs and commonly known as oxygen mimetics as they react similarly to DNA base radicals. This type of drug is shown to be particularly useful in radiosensitizing hypoxic cells with no detectable effect on normoxic cells.[161] The most plausible explanation for this is the abundance of oxygen in normal cells out-competes with nitroimidazole radiosensitizers. 5-nitroimidazole is currently used for head and neck cancer treatments in Denmark,[160] and several nitroimidazole derviatives (2-nitroimidazole) have yielded attractive sensitization enhancement ratios.[162-164] Finally, nitric oxide, like oxygen is highly reactive towards free radicals, and has also been shown to enhance the formation of DSBs, although the mechanisms are not yet clearly understood.[160]

1.9.2 Thymine Analogues as Radiosensitizers

Some thymine analogues can serve as electron sinks during irradiation forming DNA free radicals (Figure 1.5). During cellular DNA synthesis, cells are unable to recognize the difference between thymidine and halogenated forms as the molecular size of the halogens are similar to the methyl group of the thymine. Cells incubated with these analogues start to incorporate them into their DNA. After irradiation, the halogen is released resulting in a carbon free radical that can lead to DNA strand breaks.[157]

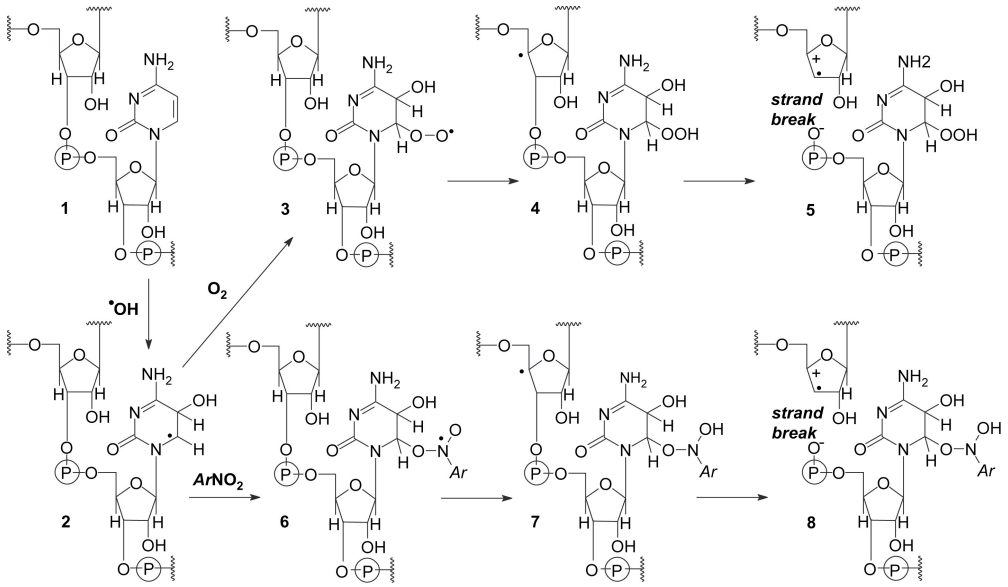

Figure 1.5 Possible pathways by which hydroxyl radicals can add to the 5,6-double bond of pyrimidines (1) to form a carbon-centred radical (2) that can either add oxygen to form a peroxyl radical (3) or add to the oxygen atom in the nitro moiety of a nitroaromatic radiosensitizer ($ArNO_2$) to form a radical adduct (6). In either case the intermediate radical (3) or (6) might abstract hydrogen from a neighbouring sugar C–H bond (5′ in this example, although 3′-abstraction may occur) to transfer radical damage from base to sugar (4) or (7), leading to a strand break (5) or (8).(adapted from Wardman et al.)[157]

1.9.3 Inhibitors of Cellular Repair and Cellular Processes

There are many different classes of DNA-targeted radiosensitizing agents that have shown to be efficacious including 5-fluorouracil through inhibiting thymidilate synthase,[165] a key enzyme responsible in regulation of the supply of DNA precursors, platinum containing compounds that inhibit DNA repair and enhance the formation of platinum intermediates via radiation induced free radicals,[166-168] gemcitabine which is a strong radiosensitizer that inhibits the action of ribonucleotide reductase, an enzyme responsible for producing deoxyribonucleotides that are used in DNA replication and repair,[169] and topoisomerase I targeted drugs that interfere with rejoining of DNA

strands.[170] Recently, new approaches have been aimed at targeting cell signaling and growth factor receptors for radiosensitzation.[157] The Ras family, an important regulator of cellular growth and differentiation, is one of the most widely studied signaling pathways with respect to radioresistance. Through inhibition of Ras functionality, radioresistance can be reversed in cells over-expressing the Ras oncogene.[157] The inhibition of epidermal growth factor receptor (EGFR) and cyclooxygenase (COX) 2 are two other approaches that are currently being investigated in pre-clinical studies.[165]

1.9.4 Depletion of Radioprotective Compounds

An alternative approach to increasing cellular radiosensitivty is to deplete or inactivate the cells capacity to absorb/neutralize activated radiation intermediates. Intracellular thiols in particular are important antioxidants that mitigate the damaging effects of reactive oxygen species preventing many cellular components from damage. Specifically, thiol-containing compounds, such as glutathione, are able to donate electrons to unstable molecules such as free radicals. Therefore, initial attempts were geared towards the depletion of intracellular thiols particularly through oxidation. While *in vitro* studies seemed very promising, the *in vivo* concentration of thiols is much higher than the tolerable doses of many agents outcompeting the oxidative effect.[157] A much more realistic approach of thiol depletion is through the inhibition of intracellular biosynthesis. One example is L-S-buthionine sulphoximine, an inhibitor of gamma-glutamylcysteine synthetase, which is responsible for the first step of glutathione synthesis. *In vitro* analysis showed significant enhancement in radiosentization but unfortunately this was not corroborated in *in vivo* evaluations.[171-174] A likely explanation for poor *in vivo* enhancement is that other than glutathione, cells contain many other

antioxidants and thiols such as ascorbate, cysteine, and protein thiols.[157] Circumin, the yellow pigment of turmeric, has also been shown to confer radiosensitizing effects in cancer cells.[175] It has been suggested that a possible mechanism of radioprotection is through the enhancement of ROS production by down-regulating Prp4K, a serine–threonine protein kinase that plays a central role in cell signaling and proliferation, and through the suppression of antioxidant enzymes.[176, 177]

1.9.5 Radiation Induced Radiosensitizers

Radiation induced radiosensitizers have recently attracted a lot of interest. These agents primarily take advantage of the reactive chemical intermediates that are generated within an irradiated region of interest. For example, Tanabe et al. showed that a prodrug conjugate of fluoro-2′ deoxyuridine with a strong electrophile was released after ionizing radiation,[178] and Sykes et al attached DNA alkylating agents to 2,6-dintrophenyl that were released following radiolytic reduction resulting in enhanced cell death.[179] Redox metals such as cobalt (III) and copper (II) have been investigated for their use as radiosensitizers. Ahn et al. used cobalt (III) complexes, containing 8-hydroxyquinoline or tetradentate macrocycles, as a redox target for radiation induced reducing radicals. Once reduced, 8-hydroxyquinoline can alkylate DNA and inhibit cell proliferation.[180]

Many studies have indicated that molecules containing high atomic number (Z) elements might serve as radiosensitizers.[181] The number of DNA DSBs was found to increase when radiation was applied in the presence of platinum containing compounds.[182] Furthermore, gadolinium, which has reached clinical trials, has shown improved neurological time to progression in patients with brain cancer metastasis.[183] With recent advances in nanotechnology and chemistry, various novel and effective

nano-sensitizers have been developed and evaluated in biological systems including carbon nanotubes,[184] and platinum,[185] gadolinium[186, 187] and gold nanoparticles.[186, 188] Of these elements, gold is by far the most popularly examined nanoplatform in radiosensitization and it was adapted for use in the work described in this thesis.

1.10 Gold Nanoparticles

Nanoparticles are generally defined to be anything on the scale of 1 – 200 nm in diameter and are being extensively investigated for their use in prevention, diagnosis, and treatment of disease. This technology has the potential to extend life expectancy, improve the quality of life, lower healthcare costs, and ultimately patient outcome.[189] Nanotechnology has moved towards clinical translation in many fields including drug delivery,[190] immunizations,[191, 192] image-guided surgery,[193, 194] and imaging.[195, 196] With the growing number of nanoparticle formulations, the variety of materials used, the number of distinct nano-platforms is too numerous to count.

Gold nanoparticles (AuNPs) have attracted considerable interest in the field of medicine. Due to their unique chemical and physical properties, AuNPs have been shown to be beneficial in many applications including catalysis, biosensors, cancer imaging, photothermal therapy, and drug delivery.[197, 198] AuNPs can be finely tuned to many different shapes and sizes, decorated with stealth-like features for immune system evasion and improve stability, functionalized with various targeting moieties to improve tumor specificity, and are considered to be nontoxic.[199, 200] In fact, aurothiolate and colloidal gold have been historically used in medical practice as a treatment for rheumatoid arthritis.[201] Recently, studies have proposed the use of AuNPs as novel radiosensitizers that can selectively enhance radiation therapy efficacy leading to increased DNA damage and cell death.[202, 203]

1.10.1 Limitations to Clinical Translation

Currently, a major obstacle that must be overcome before AuNPs (and many other nanoparticulate systems) can be translated to the clinic is slow elimination. It has been

found that there is only a 9% fall in the content of gold in the liver from day 1 to 6 months, following the intravenous injection of 40nm AuNPs.[204] This is consistent with a number of similar studies, which saw little to no clearance of ~20 nm AuNPs over shorter time periods (1 to 4 months).[205, 206] It has been shown that whole-body clearance can be improved through the use of small AuNPs (<6 nm), since these particles are small enough to undergo glomerular filtration.[207, 208] However, smaller AuNPs possess a smaller cross-sectional area and shorter path length for x-ray attenuation and are much more rapidly excreted through the kidneys.[209] Therefore, they are expected to be less favorable for both enhanced permeability and retention mediated tumor accumulation and targeted studies, where AuNP accumulation is governed by blood residence time or the number of cell surface receptors at the target site, respectively. Larger AuNPs are expected to provide superior circulation, higher contrast-to-noise ratio, and better radioenhancement in these applications. Larger AuNPs are also expected to have longer circulation times for CT angiography. A major goal of this thesis was to develop a nanoformulation containing AuNPs that exhibited a long circulation time but was still capable of being efficiently excreted.

1.10.2 Mechanism of Gold Dose Enhancement in X-ray Therapy

The mechanism of gold enhancement, in X-ray therapy, is dependent on the energy of incident ionizing photons and different interactions between the photons and AuNPs. Here, I will discuss three fundamental mechanisms of radiation enhancement photoelectric effect, Compton scattering, and pair prodcution. The photoelectric effect is the predominant mechanism of radiosensitization of high atomic number (Z) elements,

for photons with energies in the range of 10 to 500 keV.[210] The cross section of the photoelectric effect varies with the atomic number approximately as Z^3, meaning that higher Z atoms will have a larger absorption cross section. The photoelectric effect is also dependent on the energy of the photon, with a maximum cross section when the photon energy is equal to the binding energy of orbital electrons. This effect decreases sharply as energy is increased and varies as E^{-3} (Figure 1.6). The binding energies of electrons bound to gold are 79 keV for the inner shells, 13 keV, and 3 keV for outer shells, while those of soft tissue are on the order of 1 keV or lower resulting from the lower atomic number of organic matter. Therefore gold would absorb significantly more energy than soft tissue in the kilovoltage energy range. When photons with energies in these ranges interact with AuNPs, they can produce electrons, characteristic X-rays of gold atoms, or Auger electrons. Once an atom absorbs a photon an electron may be emitted resulting in an ionized atom.

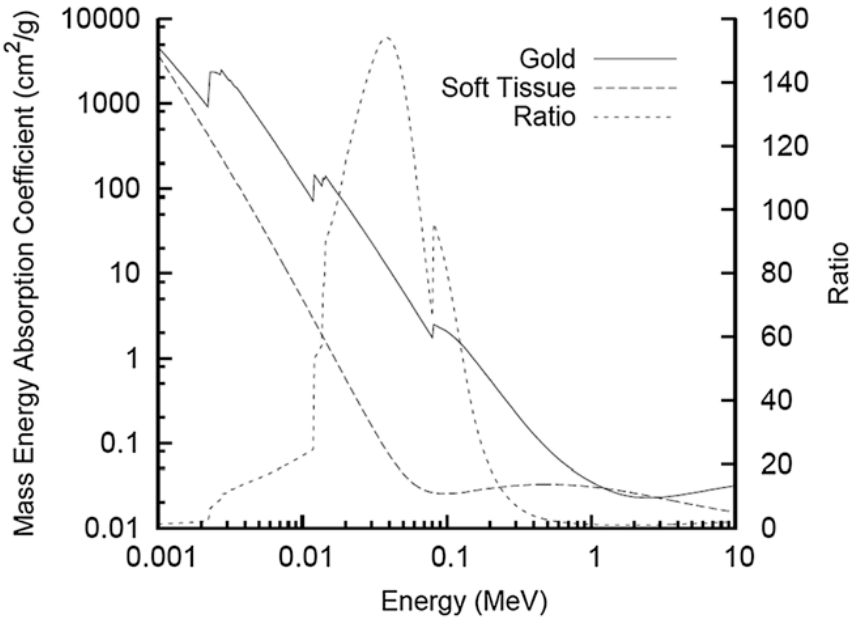

Figure 1.6. Comparison of mass energy absorption coefficients as a function of photon energy.[211] (adapted from Butterworth et al.)

When photons of energy greater than the binding energy of an inner shell electron collide, that electron is ejected leaving behind a vacancy in an orbital electron shell. As a result, outer electrons in a higher energy state fill the vacancy in the lower energy orbital. This process is accompanied by either a fluorescent photon or an Auger electron ejected from an outer shell with an energy equal to the difference between the two orbital shells. If multiple shells exist within an atom then further auger electrons can be generated as outer shell electrons fill in the vacancies. This phenomenon is known as the Auger cascade. The number of Auger electrons emitted is directly proportional to the atomic number. Therefore high Z atoms are expected to generate much more Auger electrons.[181] The range of these emitted electrons have been calculated to be around tens of nanometers depositing their energy along their path and distributing radiation throughout the system.[181] Furthermore, the Auger electron "shower" can produce highly positively charged ions, causing local Coulomb-force fields that can disrupt nearby cellular strcutures.

The enhancement of radiation with high-Z material was first realized when DNA damage was detected in lymphocytes isolated from patients receiving iodinated contrast agents for X-ray imaging.[212] Since then many other studies have demonstrated that radiation therapy in combination with iodine suppressed tumor growth and improved survival in animal models.[213] Another interesting approach was the incorporation of iodine into cellular DNA yielding a 3-fold improvement in *in vitro* radiosensitization.[214] However this strategy is not as effective if insufficient levels of iododeoxyuridine is substituted with thymine. Although the mechanisms of radiation enhancement of gold nanoparticles are not well understood, it is currently believed that the interaction of X-

rays with high Z atoms induces the release of photoelectrons and Auger electrons.[210] Given that gold has a higher Z number, it is likely that gold as a radiosensitizer would be much more effective than iodine.

When photon energies are greater than 500 keV, Compton effects begin to dominate. The Compton effect is the incoherent or inelastic scattering between an X-ray photon and an electron of an atom. In this interaction, only a part of the energy is transferred to the electron. The resulting emitted electron is known a Compton electron leaving behind an ionized atom or molecule. In contrast to photoelectric interactions where most photoelectrons are inner electrons, Compton interactions increase for loosely bound electrons. So most of the Compton electrons are valence electrons. In contrast to Auger electrons, Compton electrons are capable of travelling several hundred microns.

For incident photons with energies higher than 1.02 MeV, a process known as pair production dominates where the photon is absorbed by the nucleus with the production of a positron and electron pairs. The probability of pair production increases with the atomic number as Z^2 and linearly with the energy of incident photons.

In this thesis, I evaluate the radiosensitizing capabilities of AuNPs using orthovolatge energy ranges with the hope that it applies to the clinically relevant megavoltage energies. The interaction of charged particles is more complex and beyond the scope of this thesis, however, some studies have speculated that proton-AuNP interactions lead to increased production of low energy delta-ray electrons producing a high degree of lethal damage within the cells thus lowering the surviving fraction of cells.[215]

While most AuNP radiosensitization has primarily been attributed to their photon absorption capabilities, recent studies highlight that a significant biological component may be responsible for radiosensitization. In the absence of radiation, AuNPs have been reported to induce ROS that cause oxidative DNA damage.[211] In addition, AuNPs have been shown to cause alterations in the cell cycle with an increase in cells at the G2/M phase.[216] In a recent study by Kang et al., the nuclear targeting of AuNPs has been shown to cause cytokinesis arrest leading to the failure of complete cell division and apoptosis.[217] Although experimental evidence may suggest the involvement of biological components in radiosensitization, the exact mechanisms are still not clearly understood.

1.10.3 Modeling Dose Enhancement of AuNPs

Clinically, most X-ray radiotherapy is administered in the MV energy range as these energies have superior penetration capabilities along with a reduced dose delivered to surrounding normal tissues. Until recently, most preclinical studies performed with AuNPs were limited to kilovolatge X-rays, which can be attenuated by normal tissues and have poor penetration capabilities, especially for deep-seated tumors. Some preliminary simulations using AuNPs and radiation are suggestive that they may be effective at clinically relevant radiation energies.

Most theoretical studies of high-Z dose enhancement are performed using Monte Carlo modeling.[218] These theoretical experiments simulate the probabilistic interaction of photons and electrons based off the cross-section of different interaction processes. Using these modeled interactions along with parameters that take into consideration the attenuation of the medium, the production of secondary electrons through interaction with biological structures and gold, as well as the irregularities in beam geometry, predictions

regarding the dose distributed can be made.[211] Recent studies have assessed the enhancement effects of radiation in tumors containing high-Z materials. In a study performed by Robar et al., gadolinium and iodine contrast media showed very little dose enhancement between incident photon energies of 6 – 24 MV, however when lower energy filters were removed, there was an improvement in the dose enhancement factor.[219] Ngwa et al. used Monte Carlo simulations to show that AuNPs may be used to ablate tumor endothelial cells using brachytherapy sources of radiation with endothelial dose enhancement factors ranging from 6.4 – 271.5, for AuNP concentrations ranging from 7 to 350 mg/g.[220] Several other studies also validated that AuNPs could be used along with clinical brachytherapy sources for significant tumor dose enhancements.[221, 222] In another study by Cho et al., Monte Carlo simulations were used to determine the dose enhancements using three different gold concentrations at 140 kVp X-rays, 4, and 6 MV.[223] The largest dose enhancement factors observed were those using the highest concentrations of AuNPs (3% Au in tumor). Specifically, 2-MV and 6-MV photon beams yielded enhancements between 1% and 7% depending on the AuNP concentration. However, at 140-kVp dose enhancement effects that ranged from 211% to 560% were obtained. Consistent with this study, other Monte Carlo reports have analyzed the characteristics of secondary electrons when X-rays interact with AuNPs (50 kVp, 250 kVp, cobalt – 60, and 60 MV). It was confirmed that low energy photon beams and larger diameter AuNPs were 2 – 3 fold more efficient in AuNP interaction compared to MV energies. Moreover, secondary electron production increased by 10 to 2000 fold compared to radiation without AuNPs and the electron trajectory for the beams used ranged from 3 μm to 1 mm.[224] Tsiamas et al. investigated the dose enhancement ratio due

to AuNPs using various filtered beam energies (2.5, 4, 6.5 MV) and low Z linac targets. They concluded that 2.5 MV AuNP therapy is possible for deep seated tumors with an increase in the dose enhancement ratio by a factor of 2, as compared to a standard 6.5 MV linac.[225] While most Monte Carlo simulations show little enhancement with AuNPs at the megavoltage energies typically used in radiotherapy, some *in vitro* experiments have reported significant radiosensitization using megavoltage X-ray sources.[213, 226] In an attempt to explain these discrepancies, McMahon et al. used Monte Carlo simulations to calculate the radiation dose on the nanoscale. Their findings suggest that AuNP radiosensitization is governed by dose inhomogenieties on the nanoscale level.[227] Finally, a recent study published by Dorsey et al., concluded that a 1 and 10mg/ml solution of pegylated AuNPs showed 1.8 – 2 fold dose enhancement compared to a PEG solution or water alone using unfiltered beam energies of 6 MV.[200]

1.10.4 *In vitro* Radiosensitization Using AuNPs

By far the majority of *in vitro* and *in vivo* studies analyzing AuNP mediated radioenhancement rely on the enhanced permeability and retention effect (EPR). As a tumor continues to grow, it will reach a level where metabolic requirements exceed the ability of the vasculature supply.[228] Consequently, the tumor will respond by secreting factors to promote the process of angiogenesis resulting in the formation of new blood vessels crucial for continued growth. Many of these rapidly forming blood vessels are characterized by a non-intact basement membrane resulting in an increased permeability to macromolecular structures.[229] In addition, these actively growing tumors are often equipped with impaired and disorganized lymphatic vessels, causing poor lymphatic drainage resulting in retention of material in the tumor interstitium.[228] This phenomenon

of leaky blood vessels and ineffective lymphatic drainage is known as the EPR effect and is a main driving force behind nanoparticle accumulation in malignancies for diagnostic and therapeutic applications. Tumor targeting that relies solely on the nanoparticle's pharmacokinetic profile and EPR effect is most commonly referred to as passive targeting, while strategies that achieve tumor delivery via specific interactions with either cancer cells or their microenvironment is referred to as active targeting.

One of the earliest studies using gold for radioenhancement was performed by Regulla and colleagues.[230] In this study, enhanced radiation effects were observed in mouse embryo fibroblasts that were exposed to gold surfaces compared to those exposed to polymethylmethacrylate. Secondary electrons were found to travel a range of approximately 10 μm. Following this study, numerous other experimental studies using AuNPs over both orthovoltage and megavoltage ranges have been described. Many of these reports are controversial as there are many parameters that must be considered when performing AuNP radiosensitization such as size, shape, surface coating, concentration, radiation type and energy, and origin of cell lines (Table 1.1, adapted from Butterworth et al.). In an attempt to address these issues, Brun and coworkers investigated AuNP radiation enhancement by altering AuNP concentrations, AuNP diameter, and incident X-ray energy (range 14.8 – 70 keV). They determined that the conditions with the most radiation enhancement were those using larger sized AuNPs, high gold concentration, and 50 keV photons providing dose enhancement factors of 6.[231] In a separate study, 1.9 nm AuNPs enhanced the response of bovine aortic endothelial cell damage inflicted by X-ray irradiation, with a dose enhancement factor up to 24.6.[232] While optimal sizes for AuNP radiation therapy may be inconclusive, it is generally

accepted that radiation induced DNA damage will increase with increasing concentrations of AuNPs.[233] *In vitro* experiments using brachytherapy sources and AuNPs have also been reported and initially demonstrated a biological effect with irradiation up to 130% greater than without AuNPs.[234]

Most photoelectrons, Auger electrons, and other secondary electrons have low energies and a short range in tissues (nm to μm) delivering lethal doses in their immediate surroundings.[235] The possibility of having AuNPs target specific cancer cells may increase the production of secondary electrons within the vicinity of DNA molecules, especially if they involve cellular internalization.[236] Chattopadhyay et al. was one of the first to validate this hypothesis by synthesizing trastuzumab-PEG-AuNPs.[237] Briefly, SKBR-3 cells were irradiated after treatment with either phosphate buffered saline, PEG-AuNPs, or trastuzumab-PEG-AuNPs. The DNA DSBs as measured by γ-H2AX foci increased 5.1 and 3.3 times for targeted AuNPs compared to cells treated with PBS or PEG-AuNPs respectively. AuNPs modified with either cysteamine of thioglucose have been shown to have differential accumulation in cancer cells. While cysteamine modified AuNPs were preferentially limited to the cell membrane of MCF-7 breast cancer cells, glucose-AuNPs are internalized and distributed throughout the cytoplasm.[238, 239] Furthermore, glucose-AuNPs exhibited enhanced irradiation (200 kVp) induced cell death compared to cysteamine-AuNPs and irradiation alone. Finally, in another independent study, radiotoxicity of proton therapy with AuNP internalization was increased by approximately 15 – 20% compared to proton therapy without AuNPs.[215] However, these results are inconclusive, as targeted AuNPs were not compared to non-targeted AuNPs.

Table 1.1. Summary of *in vitro* radiosensitzation experiments using AuNPs

*SER- Surface Enhancement Ratio

*DEF- Dose Enhancement Factor

Author	Size (nm)	Concen-tration	Surface coating	Cell model	Energy source	DEF	SER
Geng et al.[239]	14	5 nM	Glucose	SKOV-3	90 kVp 6 MV	1.002 1.00009	1.3 1.2
Jain et al.[226]	1.9	12 μM	Thiol	DU145 MDA-231MB L132	160 kVp 6 MV 15 MV 6 MeV e^- 16 MeV e^-	1.05 1.0005 1.0005 1 1	<1.41 <1.29 1.16 <1.12 1.35
Chithrani et al.[213]	14 74 50	1 nM	Citrate	HeLa	220 kVp 6 MV e^- 662 keV	1.09 1.0008 1.0006	1.17-1.16
Liu et al.[240] 2010	6.1	>1 mM	PEG	CT-26 EMT-6	6 keV e^- 160 kVp 6 MV	1 1.02 1.002	2 1.1 1
Butterworth et al.[241]	1.9	2.4 μM 0.24 μM	Thiol	DU-145 MDA-231MB AG0-1522 Astro L132 T98G MCF-7 PC-3	160 kVp	1.01 1.01 1.01 1.01 1.01 1.01 1.01 1.01 1.01	<1 <1.67 <1.97 <1.04 <1 <1.91 <1.41 <1.07 1.3
Kong et al.[238]	10.8	15 nM	Glucose Cysteamine	MCF-7 MCF-10A	200 kVp 662 keV 1.2 MV	1.01 1.00008 1.00001	1.3 1.6
Rahman et al.[232]	1.9	<1 mM	Thiol	BAEC	80 kV 150 kV 6 MV e^- 12 MV e^-	6.6 5.2 1 1	20 1.4 2.9 3.7
Roa et al.[216]	10.8	15 nM	Glucose	DU-145	662 keV	1.00008	>1.5
Zhang et al.[242] 2008	30	15 nM	Glucose TGS	DU-145	200 kVp	1.0083 1.0083	>1.3 >1.5
Chang et al.[243]	13	11 nM	Citrate	B16F10	6 MV e^-	1	1
Chien et al.[244]	20	<2 mM	Citrate	CT-26	6 MV e^-	1	1.19

Zhang et al.[245] 2009	4.8 12.1 27.3 46.6	0.095 – 3mM	Citrate	K562	2-10 kR gamma	
Liu et al.[246] 2008	4.7	500 μM	PEG	CT-26	6 MV	1.3 – 1.6
Chattopa-dhyay et al.[237] 2010	30	0.3 nM	Trastuzumab PEG	SK-BR-3	300 kVp	5.1
Brun et al.[231]	8.1 20.2 37.5 74 91.7	1 – 5 nM	Citrate	Plasmid DNA	30 kV 80 kV 80 kV 100 kV 120 kV 150 kV	< 3.3

1.10.5 *In vivo* Radiosensitization Using AuNPs

In 2004, Hainfeld et al. performed the first animal study evaluating enhanced tumor radiosensitization using AuNPs. Using 1.9 nm AuNPs in combination with 250 kVp X-rays (30 Gy), overall tumor-xenograft mouse survival was 86% versus 20% for radiation alone and 0% for gold only.[188] Since then AuNPs radiosensitization has been demonstrated *in vivo* with murine mammary ductal carcinoma,[201] murine squamous cell carcinomas,[188] human sarcoma cells,[203] and cervical carcinoma(See Table 1.2).[247] In a study by Zhang and colleagues, *in vivo* radiosensitization was studied using four different sizes of PEG-AuNPs, and demonstrated that while all sizes can decrease tumor volumes after gamma radiation (5 Gy), the smallest (4.8 nm) and largest (46.6 nm) particles tested had weaker sensitization effects than 12.1 and 27.3 nm.[248] However, in a recent study by Zhang et al., glutathione coated AuNPs with sizes less than 2 nm have the ability to accumulate preferentially within subcutaneous tumor bearing mice providing strong radioenhancement for cancer therapy.[247] More recently, Joh et al. showed that PEG-AuNPs and radiation therapy can enhance DNA damage, tumor cell destruction, and

improve survival in mice with orthotopic glioblastoma multiforme tumors.[249] Intriguingly, they also showed that ionizing radiation could compromise the integrity of the blood brain barrier significantly increasing the accumulation of AuNPs within brain tumor bearing mice. All of these strategies mentioned are examples of passive tumor targeting of AuNPs that are reliant on the EPR effect. To our knowledge, a study conducted by Chattopadhyay and coworkers is the only one that assessed the *in vivo* radioenhancement effects of AuNPs, using a tumor specific HER-2 targeted nanoplatform.[235] However, the benefits of having targeted-AuNPs versus untargeted were not conclusive as there were no *in vivo* comparisons made, and AuNPs were administered via intratumoral injections.

Very few *in vivo* studies have been carried out using MV photon energy beams that are commonly used in radiotherapy. However, some emerging studies are suggestive of the clinical potential of AuNPs in improving outcomes of radiotherapy. Using 6 MV electrons with 13 nm AuNPs, tumor growth was significantly retarded and survival was prolonged compared to radiation alone in mice with melanoma flank tumors.[243] Increased tumor sensitization with AuNPs has also been demonstrated using proton therapy.[250] Proton beam irradiations of 45 MeV (10-41 Gy) were delivered to subcutaneous colon carcinoma tumors in mice after receiving a single dose of 100 – 300 mg/kg of AuNPs, which led to a 58 – 100% one year survival versus 11 – 13% in proton only irradiations.

Table 1.2 Summary of *in vivo* radiosensitzation experiments using AuNPs

*DE- Dose Enhancement

Author	Size (nm)	AuNP Dose (g kg^{-1})	Tumor conc. (mg g^{-1})	Surface coating	Cell model	Source energy	Dose (Gy)	Predicted DE
Hainfeld et al.[202]	1.9	0-2.7	7	Thiol	SCCVII	68 kV 157 kV	30	1.84 1.315
Hebert et al.[201]	5	0-0.675	0.1	DTDTPA-Gd	MCF7-L1	150 kV	10	1.01
Chang et al.[243]	13	0-0.036	74	Citrate	B16F10	MV e^-	25	1.01
Hainfeld et al.[188] 2004	1.9	0-2.7	7	Thiol	EMT-6	250 kV	26-30	1.56
Joh et al.[203] 2013	12.4	0-1.25	1.25	PEG	HT1080	175 kV	6 Gy	1.16
Joh et al.[249] PLOS	12	0-1.25	0.15	PEG	U251	175 kV	20 Gy	1.3
Kim et al.[250] 2012	14	0-0.3	0.1 – 0.2	Citrate	CT26	Proton 40 MV	10-41 Gy	
Zhang et al.[248] 2012	4.8 12.1 27.3 46.6	0-4		PEG	U14	Gamma Rays	5 Gy	1.41 1.65 1.58 1.42
Chattopadhyay et al.[237]	30		4.8	Herceptin	MDA-MB-361	100 kV	11 Gy	
Atkinson et al.[251]		n/a	n/a	n/a		n/a	6 Gy	
Zhang et al.[247] 2014	1.5	0.01	0.01456	GSH BSH	U14	662kV	5 Gy	

1.11 X-ray Computed Tomography Imaging & Contrast Agents

Developed in the 1970s, computerized transverse axial tomography is a technique that acquires many X-ray projection images from different directions. Using dedicated computer algorithms, 3D volume reconstructions are generated enabling the visualization of internal anatomical features within the human body. Today, with the introduction of modified detector technologies and the advent of spiral scanning, whole organs or the body can be imaged in a matter of seconds with sub-millimeter resolution.

While many tissue structures may have varying X-ray attenuation characteristics, it is often difficult to delineate abnormal tissue pathology accurately without the administration of a contrast agent. Water-soluble iodinated compounds have long been used as X-ray contrast agents. Iodinated compounds in clinical use have low molecular weights, ranging from 127 Da for iodide to about 1600 Da for tri-iodobenze dimers (e.g. iodixanol, 1550 Da). Because of their small size, iodinated contrast agents exhibit rapid renal clearance and vascular permeation, necessitating short imaging times. As a result, intra-arterial catheterization is often needed, which carries the risk of arterial puncture, dislodgement of plaques, stroke, myocardial infarction, anaphylactic shock and renal failure. Patients with impaired renal function carry a particular high risk for adverse effects.[209, 252]

To overcome some of the disadvantages associated with low-molecular weight contrast agents, chemists have used many different strategies to increase the molecular weight of X-ray contrast media, e.g. iodinated polysaccharides,[253]polymeric tri-iodobenzenes,[254] and cascade polymers carrying tri-iodobenzenes.[255] Similar agents have

also been prepared with dysprosium and gadolinium (Gd).[256, 257] However, complex chemistry and problems with tolerability have kept these agents from reaching clinical trials.[255]

An alternative to using macromolecules is to incorporate many highly attenuating atoms into nanoparticles. Nanoparticles offer an opportunity for longer circulation times, visualization of the reticuloendothelial system (RES), blood pool imaging, and lymphography. Molecular imaging is also possible since each nanoparticle is capable of carrying many atoms with high atomic number, providing a mechanism to increase contrast at the target site.[258, 259] Over the past two decades, many nanoparticulate X-ray contrast agents have been developed, including liposomes loaded with iodinated compounds,[260, 261] polymeric iodine-containing PEG-based micelles,[262] iodine containing perfluorocarbons,[263, 264] bismuth sulfide nanoparticles,[265] and AuNPs.[188, 209] Of these, gold nanoparticles have garnered a particularly high degree of interest. In comparison to iodine, gold possesses a mass attenuation coefficient that is ~2.7-fold higher.[266] Accordingly, it was found that 1.9 nm AuNPs exhibit a better contrast-to-noise ratio (CNR) on both projection radiography (40-80 kVp) and computed tomography (CT) (80-140 kVp).[209, 266-268] Specifically, at equimolar concentrations, AuNPs exhibited an 89% improvement over iopromide at low energies near the mammographic range (40 kVp) and a 114% greater CNR at higher energies (140 kVp).[266] Similarly, 30 nm AuNPs attenuated 120 kVp X-rays 5.7 times more than the iodine-based agent, Ultravist.[268] The high attenuating properties of AuNPs has recently led to their successful implementation as targeted molecular imaging agents in mice.[258, 259] Notably, the additional benefits of working with AuNPs are that the size and shape can easily be controlled and the surface

can be modified with various functional groups. In contrast, while other nanoparticle formulations, such as bismuth sulfide and tantalum oxide nanoparticles,[269] may also exhibit higher X-ray absorption than iodine (at 50 kVp), it is difficult to control their size and there is a lack of chemical methods to modify their surface.[265, 268]

1.12 Magnetic Resonance Imaging

Magnetic resonance imaging is a noninvasive imaging modality that utilizes strong magnetic fields to produce clinically relevant images of not only tissue structure, but also function.[270] The primary molecules responsible for signal generation during image acquisition are the protons in water, with intrinsic contrast provided by the spatial differences in proton density and relaxation times. In general there are two relaxation signals that characterize MR signals referred to as longitudinal (T_1) and transverse relaxation (T_2) time constants. The longitudinal time constant T_1, also called spin-lattice relaxation, is the process by which, following a radiofrequency pulse, the magnetization vector realigns along the longitudinal (z) axis as proton spins give their energy back to the surrounding lattice, coming into equilibrium with its surroundings. The transverse time constant T_2, also called spin-spin relaxation, is the time required for the transverse component of the magnetization vector to decay, and is a consequence of interactions between spins as well as external field inhomogeneities. By taking advantage of the different T_1 and T_2 time constants in tissues, MR images of the same anatomical structures with varying degrees of hyperintesities and hypointensities can be obtained.

1.13 Superparamagnetic Iron Oxide (SPIO) Nanoparticles

SPIO nanoparticles are predominately composed of a magnetite (Fe_3O_4) and/or maghemite (γ-Fe_2O_3) iron core and a hydrophilic/hydrophobic surface coating.[271, 272] These particles have the greatest application in providing useful contrast on T_2 or T_2^* weighted MR imaging, producing a hypointense (dark) signal. When an external magnetic field is applied, the magnetic moments are oriented in the direction of the magnetic field thereby enhancing the magnetic flux in their vicinity. The disturbances in the local magnetic field results in a rapid de-phasing of surrounding protons following an RF pulse, altering both their longitudinal and transverse relaxation characteristics, and generating a detectable change in the MR signal. Due to their strong enhancement in proton relaxation, SPIO nanoparticles have been extensively investigated as MR contrast agents. While many of the clinical studies using SPIO are in early phase clinical trials or discontinued, a few have been marketed.[273]

Over the past decades, studies using SPIO nanoparticles have shown potential applications in MR hepatic imaging (as they are readily taken up by Kupffer cells), cell tracking, cardiovascular imaging, and biomolecular detection.[272] In cancer imaging, SPIO can be used for the detection of lymph node metastases, which aids in cancer staging and therapeutic planning.[274, 275] While these applications are promising, a desirable goal is to utilize SPIO nanoparticles for cellular and molecular imaging applications, to provide earlier detection of malignancies prior to metastasis. However, a major hurdle for the detection of non-RES lesions is the sensitivity limitations of some MR contrast agents. As a result, many strategies have been utilized to improve SPIO nanoparticle sensitivity including the optimization of MR hardware and pulse sequences, nanoparticle shape and

size, SPIO cell specific targeting, and the development of SPIO nanocarriers. For example, the development of an activatable SPIO nanoparticle probe has been shown to increase contrast by improving site-specific accumulation.[276] Other approaches have significantly increased particle relaxivity by incorporating many SPIO nanoparticles within the hydrophobic core of polymeric micelles.[277, 278] This approach has been adapted in this thesis to create micelles that are capable of generating strong MR contrast. SPIO was combined with AuNPs, to create a micelle that has both diagnostic and radio-therapeutic potential.

1.14 Polymeric Micelles

Polymeric micelles offer a powerful multifunctional platform for drug delivery and diagnostic imaging applications.[279, 280] These nanoconstructs are composed of amphiphilic block co-polymers with distinct hydrophobic and hydrophilic domains that can self-assemble into supramolecular core-shell structures (usually 10 to 100 nm) in aqueous solution. The hydrophobic micelle core provides an ideal carrier compartment for hydrophobic drugs and nanoparticles,[277] and the shell consists of a protective corona that stabilizes the nanoparticles. Among the many different classes of amphiphilic block copolymers used, polyethylene oxide (PEO)-b-polycaprolactone (PCL) or poly(lactic acid) (PLA) have received the most interest as they are FDA approved materials with potential benefits that span drug delivery and diagnostic applications.[281] The dense PEG corona of the PEG-b-PCL vesicles imparts stealthiness and is able to deter membrane opsonization, and significantly extend *in vivo* circulation times.[282]

For example, the incorporation of insoluble anticancer agents into micelles has been shown to improve drug circulation, enhance cytotoxicity at the target site and enable delivery of higher doses to the tumor than with agents alone.[283, 284] Other groups have incorporated imaging agents including SPIO, for magnetic resonance imaging, radioactive metals for positron emission tomographic imaging, and organic iodine for X-ray/CT imaging.[285] Until now, the only clinically approved micelle formulation is Genexol-PM, a PEG-PLA micelle entrapped formulation of paclitaxel, used in the treatment of breast cancer. Furthermore, polymeric micelles have the flexibility of incorporating multiple types of compounds within the core for multimodal and theranostic applications as well as surface bioconjugation for active targeting.[277, 281]

In this thesis small (< 6 nm) AuNPs were encapsulated within the hydrophobic core of polymeric micelles such that they would mimic AuNPs with larger core diameters and significantly prolong their circulation in the blood. However, upon the hydrolysis of the amphiphilic polymer, we hypothesized that that presence of small AuNPs could help to improve the clearance from various organ systems and reduce long term retention. SPIO was also encapsulated within the micelle to allow for MR imaging.

1.15 Preface to Dissertation

While AuNPs have been used for diverse applications in both imaging and therapy, their poor long-term elimination and low sensitivity in X-ray imaging is a major limitation. This dissertation thesis is laid out to follow a sequence of findings that led to the development of a nanoplatform for imaging and radiotherapy with improved pharmacokinetics. The chapters are broken down as follows:

Chapter 2: Development of gold-loaded polymeric micelles with prolonged circulation for combined X-ray imaging and radiation therapy.

Chapter 3: Preparation of superparamagnetic iron oxide and gold loaded micelles for improved imaging sensitivity.

Chapter 4: Develop a targeted superparamagnetic iron based micelles for cell specific targeting.

Chapter 5: Examination of the *in vivo* long-term toxicity, clearance, and organ retention of gold-loaded polymeric micelles using two different sizes of AuNPs.

Chapter 6 is a summary of the primary discussion points that have been highlighted over the course of this dissertation and future directions for this work.

1.16 References

1. Begg, A.C., Stewart, F.A. & Vens, C. Strategies to improve radiotherapy with targeted drugs. *Nat Rev Cancer* **11**, 239-253 (2011).
2. Seibert, J.A. & Boone, J.M. X-ray imaging physics for nuclear medicine technologists. Part 2: X-ray interactions and image formation. *J Nucl Med Technol* **33**, 3-18 (2005).
3. Bernier, J., Hall, E.J. & Giaccia, A. Radiation oncology: a century of achievements. *Nat Rev Cancer* **4**, 737-747 (2004).
4. Oh, C.E., Antes, K., Darby, M., Song, S. & Starkschall, G. Comparison of 2D conventional, 3D conformal, and intensity-modulated treatment planning techniques for patients with prostate cancer with regard to target-dose homogeneity and dose to critical, uninvolved structures. *Med Dosim* **24**, 255-263 (1999).
5. Bucci, M.K., Bevan, A. & Roach, M., 3rd Advances in radiation therapy: conventional to 3D, to IMRT, to 4D, and beyond. *CA Cancer J Clin* **55**, 117-134 (2005).
6. Stone, H.B., Coleman, C.N., Anscher, M.S. & McBride, W.H. Effects of radiation on normal tissue: consequences and mechanisms. *Lancet Oncol* **4**, 529-536 (2003).
7. Chang, B.K. & Timmerman, R.D. Stereotactic body radiation therapy: a comprehensive review. *Am J Clin Oncol* **30**, 637-644 (2007).
8. Leksell, L. Stereotactic radiosurgery. *J Neurol Neurosurg Psychiatry* **46**, 797-803 (1983).

9. Werner-Wasik, M. et al. Immediate side effects of stereotactic radiotherapy and radiosurgery. *Int J Radiat Oncol Biol Phys* **43**, 299-304 (1999).

10. Flickinger, J.C., Kondziolka, D. & Lunsford, L.D. Radiosurgery of Benign Lesions. *Semin Radiat Oncol* **5**, 220-224 (1995).

11. Jensen, A.W. et al. Gamma knife radiosurgery of radiation-induced intracranial tumors: local control, outcomes, and complications. *Int J Radiat Oncol Biol Phys* **62**, 32-37 (2005).

12. Korytko, T. et al. 12 Gy gamma knife radiosurgical volume is a predictor for radiation necrosis in non-AVM intracranial tumors. *Int J Radiat Oncol Biol Phys* **64**, 419-424 (2006).

13. Marks, L.B. & Spencer, D.P. The influence of volume on the tolerance of the brain to radiosurgery. *J Neurosurg* **75**, 177-180 (1991).

14. Roman, D.D. & Sperduto, P.W. Neuropsychological effects of cranial radiation: current knowledge and future directions. *Int J Radiat Oncol Biol Phys* **31**, 983-998 (1995).

15. Minniti, G., Traish, D., Ashley, S., Gonsalves, A. & Brada, M. Risk of second brain tumor after conservative surgery and radiotherapy for pituitary adenoma: update after an additional 10 years. *J Clin Endocrinol Metab* **90**, 800-804 (2005).

16. Brada, M. et al. The long-term efficacy of conservative surgery and radiotherapy in the control of pituitary adenomas. *Clin Endocrinol (Oxf)* **38**, 571-578 (1993).

17. Kaido, T. et al. Radiosurgery-induced brain tumor. Case report. *J Neurosurg* **95**, 710-713 (2001).

18. McIver, J.I. & Pollock, B.E. Radiation-induced tumor after stereotactic radiosurgery and whole brain radiotherapy: case report and literature review. *J Neurooncol* **66**, 301-305 (2004).

19. Shamisa, A. et al. Glioblastoma multiforme occurring in a patient treated with gamma knife surgery. Case report and review of the literature. *J Neurosurg* **94**, 816-821 (2001).

20. Yu, J.S., Yong, W.H., Wilson, D. & Black, K.L. Glioblastoma induction after radiosurgery for meningioma. *Lancet* **356**, 1576-1577 (2000).

21. Wulf, J., Hadinger, U., Oppitz, U., Olshausen, B. & Flentje, M. Stereotactic radiotherapy of extracranial targets: CT-simulation and accuracy of treatment in the stereotactic body frame. *Radiother Oncol* **57**, 225-236 (2000).

22. Nagata, Y. et al. Clinical outcomes of 3D conformal hypofractionated single high-dose radiotherapy for one or two lung tumors using a stereotactic body frame. *Int J Radiat Oncol Biol Phys* **52**, 1041-1046 (2002).

23. Hof, H. et al. Stereotactic single-dose radiotherapy of stage I non-small-cell lung cancer (NSCLC). *Int J Radiat Oncol Biol Phys* **56**, 335-341 (2003).

24. Murphy, M.J. An automatic six-degree-of-freedom image registration algorithm for image-guided frameless stereotaxic radiosurgery. *Med Phys* **24**, 857-866 (1997).

25. Taylor, M.L., Kron, T. & Franich, R.D. A contemporary review of stereotactic radiotherapy: inherent dosimetric complexities and the potential for detriment. *Acta Oncol* **50**, 483-508 (2011).

26. Purdy, J.A. 3D treatment planning and intensity-modulated radiation therapy. *Oncology (Williston Park)* **13**, 155-168 (1999).

27. Verhey, L.J. Comparison of three-dimensional conformal radiation therapy and intensity-modulated radiation therapy systems. *Semin Radiat Oncol* **9**, 78-98 (1999).

28. Ling, C.C. & Fuks, Z. Conformal radiation treatment: a critical appraisal. *Eur J Cancer* **31A**, 799-803 (1995).

29. Bakiu, E., Telhaj, E., Kozma, E., Ruci, F. & Malkaj, P. Comparison of 3D CRT and IMRT Tratment Plans. *Acta Inform Med* **21**, 211-212 (2013).

30. Intensity-modulated radiotherapy: current status and issues of interest. *Int J Radiat Oncol Biol Phys* **51**, 880-914 (2001).

31. Nutting, C.M. Intensity Modulated Radiotherapy (IMRT) in head and neck cancers - an overview. *Gulf J Oncolog*, 17-26 (2012).

32. Durante, M. & Loeffler, J.S. Charged particles in radiation oncology. *Nat Rev Clin Oncol* **7**, 37-43 (2009).

33. Baskar, R., Lee, K.A., Yeo, R. & Yeoh, K.W. Cancer and radiation therapy: current advances and future directions. *Int J Med Sci* **9**, 193-199 (2014).

34. Laramore, G.E. Role of particle radiotherapy in the management of head and neck cancer. *Curr Opin Oncol* **21**, 224-231 (2009).

35. Riley, P.A. Free radicals in biology: oxidative stress and the effects of ionizing radiation. *Int J Radiat Biol* **65**, 27-33 (1994).

36. Balasubramanian, B., Pogozelski, W.K. & Tullius, T.D. DNA strand breaking by the hydroxyl radical is governed by the accessible surface areas of the hydrogen atoms of the DNA backbone. *Proc Natl Acad Sci U S A* **95**, 9738-9743 (1998).

37. Steel, G.G., McMillan, T.J. & Peacock, J.H. The 5Rs of radiobiology. *Int J Radiat Biol* **56**, 1045-1048 (1989).

38. Radford, I.R. & Broadhurst, S. Enhanced induction by X-irradiation of DNA double-strand breakage in mitotic as compared with S-phase V79 cells. *Int J Radiat Biol Relat Stud Phys Chem Med* **49**, 909-914 (1986).

39. Bedford, J.S. Sublethal damage, potentially lethal damage, and chromosomal aberrations in mammalian cells exposed to ionizing radiations. *Int J Radiat Oncol Biol Phys* **21**, 1457-1469 (1991).

40. Bredesen, D.E. Apoptosis: overview and signal transduction pathways. *J Neurotrauma* **17**, 801-810 (2000).

41. Giusti, A.M., Raimondi, M., Ravagnan, G., Sapora, O. & Parasassi, T. Human cell membrane oxidative damage induced by single and fractionated doses of ionizing radiation: a fluorescence spectroscopy study. *Int J Radiat Biol* **74**, 595-605 (1998).

42. Kerr, J.F., Wyllie, A.H. & Currie, A.R. Apoptosis: a basic biological phenomenon with wide-ranging implications in tissue kinetics. *Br J Cancer* **26**, 239-257 (1972).

43. Strasser, A. The role of BH3-only proteins in the immune system. *Nat Rev Immunol* **5**, 189-200 (2005).

44. Youle, R.J. & Strasser, A. The BCL-2 protein family: opposing activities that mediate cell death. *Nat Rev Mol Cell Biol* **9**, 47-59 (2008).

45. Fogg, V.C., Lanning, N.J. & Mackeigan, J.P. Mitochondria in cancer: at the crossroads of life and death. *Chin J Cancer* **30**, 526-539 (2011).

46. Miura, M., Friedlander, R.M. & Yuan, J. Tumor necrosis factor-induced apoptosis is mediated by a CrmA-sensitive cell death pathway. *Proc Natl Acad Sci U S A* **92**, 8318-8322 (1995).

47. Budihardjo, I., Oliver, H., Lutter, M., Luo, X. & Wang, X. Biochemical pathways of caspase activation during apoptosis. *Annu Rev Cell Dev Biol* **15**, 269-290 (1999).

48. Joza, N. et al. Essential role of the mitochondrial apoptosis-inducing factor in programmed cell death. *Nature* **410**, 549-554 (2001).

49. Verheij, M. & Bartelink, H. Radiation-induced apoptosis. *Cell Tissue Res* **301**, 133-142 (2000).

50. Dewey, W.C., Ling, C.C. & Meyn, R.E. Radiation-induced apoptosis: relevance to radiotherapy. *Int J Radiat Oncol Biol Phys* **33**, 781-796 (1995).

51. Hotchkiss, R.S., Strasser, A., McDunn, J.E. & Swanson, P.E. Cell death. *N Engl J Med* **361**, 1570-1583 (2009).

52. Kuo, S.S., Saad, A.H., Koong, A.C., Hahn, G.M. & Giaccia, A.J. Potassium-channel activation in response to low doses of gamma-irradiation involves reactive oxygen intermediates in nonexcitatory cells. *Proc Natl Acad Sci U S A* **90**, 908-912 (1993).

53. Todd, D.G. & Mikkelsen, R.B. Ionizing radiation induces a transient increase in cytosolic free [Ca2+] in human epithelial tumor cells. *Cancer Res* **54**, 5224-5230 (1994).

54. Green, D.R. & Reed, J.C. Mitochondria and apoptosis. *Science* **281**, 1309-1312 (1998).

55. Kastan, M.B., Onyekwere, O., Sidransky, D., Vogelstein, B. & Craig, R.W. Participation of p53 protein in the cellular response to DNA damage. *Cancer Res* **51**, 6304-6311 (1991).

56. Bristow, R.G., Benchimol, S. & Hill, R.P. The p53 gene as a modifier of intrinsic radiosensitivity: implications for radiotherapy. *Radiother Oncol* **40**, 197-223 (1996).

57. Wyllie, A.H., Kerr, J.F. & Currie, A.R. Cell death: the significance of apoptosis. *Int Rev Cytol* **68**, 251-306 (1980).

58. Vakifahmetoglu, H., Olsson, M. & Zhivotovsky, B. Death through a tragedy: mitotic catastrophe. *Cell Death Differ* **15**, 1153-1162 (2008).

59. Schmitt, C.A. Cellular senescence and cancer treatment. *Biochim Biophys Acta* **1775**, 5-20 (2007).

60. Dimri, G.P. et al. A biomarker that identifies senescent human cells in culture and in aging skin in vivo. *Proc Natl Acad Sci U S A* **92**, 9363-9367 (1995).

61. Klionsky, D.J. Autophagy: from phenomenology to molecular understanding in less than a decade. *Nat Rev Mol Cell Biol* **8**, 931-937 (2007).

62. Luke, C.J. et al. An intracellular serpin regulates necrosis by inhibiting the induction and sequelae of lysosomal injury. *Cell* **130**, 1108-1119 (2007).

63. Malhi, H., Gores, G.J. & Lemasters, J.J. Apoptosis and necrosis in the liver: a tale of two deaths? *Hepatology* **43**, S31-44 (2006).

64. Leist, M., Single, B., Castoldi, A.F., Kuhnle, S. & Nicotera, P. Intracellular adenosine triphosphate (ATP) concentration: a switch in the decision between apoptosis and necrosis. *J Exp Med* **185**, 1481-1486 (1997).

65. Cobb, J.P., Hotchkiss, R.S., Karl, I.E. & Buchman, T.G. Mechanisms of cell injury and death. *Br J Anaesth* **77**, 3-10 (1996).

66. Kroemer, G. et al. Classification of cell death: recommendations of the Nomenclature Committee on Cell Death 2009. *Cell Death Differ* **16**, 3-11 (2009).

67. Kroemer, G. & Jaattela, M. Lysosomes and autophagy in cell death control. *Nat Rev Cancer* **5**, 886-897 (2005).

68. Levine, B. & Deretic, V. Unveiling the roles of autophagy in innate and adaptive immunity. *Nat Rev Immunol* **7**, 767-777 (2007).

69. Palumbo, S. et al. Different involvement of autophagy in human malignant glioma cell lines undergoing irradiation and temozolomide combined treatments. *J Cell Biochem* **113**, 2308-2318 (2012).

70. Kim, K.W. et al. Autophagy upregulation by inhibitors of caspase-3 and mTOR enhances radiotherapy in a mouse model of lung cancer. *Autophagy* **4**, 659-668 (2008).

71. Moretti, L., Attia, A., Kim, K.W. & Lu, B. Crosstalk between Bak/Bax and mTOR signaling regulates radiation-induced autophagy. *Autophagy* **3**, 142-144 (2007).

72. Palumbo, S. & Comincini, S. Autophagy and ionizing radiation in tumors: the "survive or not survive" dilemma. *J Cell Physiol* **228**, 1-8 (2013).

73. Pajonk, F., Vlashi, E. & McBride, W.H. Radiation resistance of cancer stem cells: the 4 R's of radiobiology revisited. *Stem Cells* **28**, 639-648 (2010).

74. Pilch, D.R. et al. Characteristics of gamma-H2AX foci at DNA double-strand breaks sites. *Biochem Cell Biol* **81**, 123-129 (2003).

75. Jenuwein, T. & Allis, C.D. Translating the histone code. *Science* **293**, 1074-1080 (2001).

76. Felsenfeld, G. & Groudine, M. Controlling the double helix. *Nature* **421**, 448-453 (2003).

77. Rogakou, E.P., Pilch, D.R., Orr, A.H., Ivanova, V.S. & Bonner, W.M. DNA double-stranded breaks induce histone H2AX phosphorylation on serine 139. *J Biol Chem* **273**, 5858-5868 (1998).

78. Olive, P.L. Detection of DNA damage in individual cells by analysis of histone H2AX phosphorylation. *Methods Cell Biol* **75**, 355-373 (2004).

79. Limoli, C.L. & Ward, J.F. A new method for introducing double-strand breaks into cellular DNA. *Radiat Res* **134**, 160-169 (1993).

80. Sedelnikova, O.A., Rogakou, E.P., Panyutin, I.G. & Bonner, W.M. Quantitative detection of (125)IdU-induced DNA double-strand breaks with gamma-H2AX antibody. *Radiat Res* **158**, 486-492 (2002).

81. Rich, J.N. Cancer stem cells in radiation resistance. *Cancer Res* **67**, 8980-8984 (2007).

82. Woodward, W.A. et al. WNT/beta-catenin mediates radiation resistance of mouse mammary progenitor cells. *Proc Natl Acad Sci U S A* **104**, 618-623 (2007).

83. Phillips, T.M., McBride, W.H. & Pajonk, F. The response of CD24(-/low)/CD44+ breast cancer-initiating cells to radiation. *J Natl Cancer Inst* **98**, 1777-1785 (2006).

84. Diehn, M. et al. Association of reactive oxygen species levels and radioresistance in cancer stem cells. *Nature* **458**, 780-783 (2009).

85. Bao, S. et al. Glioma stem cells promote radioresistance by preferential activation of the DNA damage response. *Nature* **444**, 756-760 (2006).

86. Lomonaco, S.L. et al. The induction of autophagy by gamma-radiation contributes to the radioresistance of glioma stem cells. *Int J Cancer* **125**, 717-722 (2009).

87. Pawlik, T.M. & Keyomarsi, K. Role of cell cycle in mediating sensitivity to radiotherapy. *Int J Radiat Oncol Biol Phys* **59**, 928-942 (2004).

88. Formenti, S.C. et al. Concurrent paclitaxel and radiation therapy for breast cancer. *Semin Radiat Oncol* **9**, 34-42 (1999).

89. Hennequin, C., Giocanti, N. & Favaudon, V. Interaction of ionizing radiation with paclitaxel (Taxol) and docetaxel (Taxotere) in HeLa and SQ20B cells. *Cancer Res* **56**, 1842-1850 (1996).

90. Kano, Y. et al. Schedule-dependent synergism and antagonism between paclitaxel and methotrexate in human carcinoma cell lines. *Oncol Res* **10**, 347-354 (1998).

91. Withers, H.R. Cell cycle redistribution as a factor in multifraction irradiation. *Radiology* **114**, 199-202 (1975).

92. Sinclair, W.K. & Morton, R.A. X-ray sensitivity during the cell generation cycle of cultured Chinese hamster cells. *Radiat Res* **29**, 450-474 (1966).

93. Bentzen, S.M. Repopulation in radiation oncology: perspectives of clinical research. *Int J Radiat Biol* **79**, 581-585 (2003).

94. Lauber, K. et al. Apoptosis induction and tumor cell repopulation: the yin and yang of radiotherapy. *Radiat Oncol* **6**, 176.

95. Kim, J.J. & Tannock, I.F. Repopulation of cancer cells during therapy: an important cause of treatment failure. *Nat Rev Cancer* **5**, 516-525 (2005).

96. Withers, H.R. Biologic basis for altered fractionation schemes. *Cancer* **55**, 2086-2095 (1985).

97. Withers, H.R. et al. Local control of carcinoma of the tonsil by radiation therapy: an analysis of patterns of fractionation in nine institutions. *Int J Radiat Oncol Biol Phys* **33**, 549-562 (1995).

98. Barton, M.B., Keane, T.J., Gadalla, T. & Maki, E. The effect of treatment time and treatment interruption on tumour control following radical radiotherapy of laryngeal cancer. *Radiother Oncol* **23**, 137-143 (1992).

99. Fyles, A., Keane, T.J., Barton, M. & Simm, J. The effect of treatment duration in the local control of cervix cancer. *Radiother Oncol* **25**, 273-279 (1992).

100. Peters, L.J., Ang, K.K. & Thames, H.D., Jr. Accelerated fractionation in the radiation treatment of head and neck cancer. A critical comparison of different strategies. *Acta Oncol* **27**, 185-194 (1988).

101. Norin, T. et al. Conventional and superfractionated radiation therapy in Burkitt's lymphoma. *Acta Radiol Ther Phys Biol* **10**, 545-557 (1971).

102. Bourhis, J. et al. Phase III randomized trial of very accelerated radiation therapy compared with conventional radiation therapy in squamous cell head and neck cancer: a GORTEC trial. *J Clin Oncol* **24**, 2873-2878 (2006).

103. Bourhis, J. et al. Hyperfractionated or accelerated radiotherapy in head and neck cancer: a meta-analysis. *Lancet* **368**, 843-854 (2006).

104. Fu, K.K. et al. A Radiation Therapy Oncology Group (RTOG) phase III randomized study to compare hyperfractionation and two variants of accelerated fractionation to standard fractionation radiotherapy for head and neck squamous cell carcinomas: first report of RTOG 9003. *Int J Radiat Oncol Biol Phys* **48**, 7-16 (2000).

105. Overgaard, J. et al. Five compared with six fractions per week of conventional radiotherapy of squamous-cell carcinoma of head and neck: DAHANCA 6 and 7 randomised controlled trial. *Lancet* **362**, 933-940 (2003).

106. Hockel, M. et al. Association between tumor hypoxia and malignant progression in advanced cancer of the uterine cervix. *Cancer Res* **56**, 4509-4515 (1996).

107. Brizel, D.M. et al. Tumor oxygenation predicts for the likelihood of distant metastases in human soft tissue sarcoma. *Cancer Res* **56**, 941-943 (1996).

108. Brizel, D.M., Sibley, G.S., Prosnitz, L.R., Scher, R.L. & Dewhirst, M.W. Tumor hypoxia adversely affects the prognosis of carcinoma of the head and neck. *Int J Radiat Oncol Biol Phys* **38**, 285-289 (1997).

109. Nordsmark, M. et al. Prognostic value of tumor oxygenation in 397 head and neck tumors after primary radiation therapy. An international multi-center study. *Radiother Oncol* **77**, 18-24 (2005).

110. Fyles, A. et al. Tumor hypoxia has independent predictor impact only in patients with node-negative cervix cancer. *J Clin Oncol* **20**, 680-687 (2002).

111. Kallman, R.F. & Dorie, M.J. Tumor oxygenation and reoxygenation during radiation therapy: their importance in predicting tumor response. *Int J Radiat Oncol Biol Phys* **12**, 681-685 (1986).

112. Bertout, J.A., Patel, S.A. & Simon, M.C. The impact of O2 availability on human cancer. *Nat Rev Cancer* **8**, 967-975 (2008).

113. Saunders, M. & Dische, S. Clinical results of hypoxic cell radiosensitisation from hyperbaric oxygen to accelerated radiotherapy, carbogen and nicotinamide. *Br J Cancer Suppl* **27**, S271-278 (1996).

114. Watson, E.R. et al. Hyperbaric oxygen and radiotherapy: a Medical Research Council trial in carcinoma of the cervix. *Br J Radiol* **51**, 879-887 (1978).

115. Henke, M. et al. Erythropoietin to treat head and neck cancer patients with anaemia undergoing radiotherapy: randomised, double-blind, placebo-controlled trial. *Lancet* **362**, 1255-1260 (2003).

116. Belenkov, A.I. et al. Erythropoietin induces cancer cell resistance to ionizing radiation and to cisplatin. *Mol Cancer Ther* **3**, 1525-1532 (2004).

117. Poskitt, T.R. Radiation therapy and the role of red blood cell transfusion. *Cancer Invest* **5**, 231-236 (1987).

118. Overgaard, J. Hypoxic radiosensitization: adored and ignored. *J Clin Oncol* **25**, 4066-4074 (2007).

119. Rischin, D. et al. Tirapazamine, Cisplatin, and Radiation versus Fluorouracil, Cisplatin, and Radiation in patients with locally advanced head and neck cancer: a

randomized phase II trial of the Trans-Tasman Radiation Oncology Group (TROG 98.02). *J Clin Oncol* **23**, 79-87 (2005).

120. Brown, J.M. & Wilson, W.R. Exploiting tumour hypoxia in cancer treatment. *Nat Rev Cancer* **4**, 437-447 (2004).

121. von Pawel, J. et al. Tirapazamine plus cisplatin versus cisplatin in advanced non-small-cell lung cancer: A report of the international CATAPULT I study group. Cisplatin and Tirapazamine in Subjects with Advanced Previously Untreated Non-Small-Cell Lung Tumors. *J Clin Oncol* **18**, 1351-1359 (2000).

122. Rischin, D. et al. Tirapazamine, cisplatin, and radiation versus cisplatin and radiation for advanced squamous cell carcinoma of the head and neck (TROG 02.02, HeadSTART): a phase III trial of the Trans-Tasman Radiation Oncology Group. *J Clin Oncol* **28**, 2989-2995 (2010).

123. Puck, T.T. & Marcus, P.I. Action of x-rays on mammalian cells. *J Exp Med* **103**, 653-666 (1956).

124. Franken, N.A., Rodermond, H.M., Stap, J., Haveman, J. & van Bree, C. Clonogenic assay of cells in vitro. *Nat Protoc* **1**, 2315-2319 (2006).

125. Chen, Y. et al. Radiation pneumonitis and early circulatory cytokine markers. *Semin Radiat Oncol* **12**, 26-33 (2002).

126. Rubin, P., Johnston, C.J., Williams, J.P., McDonald, S. & Finkelstein, J.N. A perpetual cascade of cytokines postirradiation leads to pulmonary fibrosis. *Int J Radiat Oncol Biol Phys* **33**, 99-109 (1995).

127. Fu, X.L. et al. Predicting the risk of symptomatic radiation-induced lung injury using both the physical and biologic parameters V(30) and transforming growth factor beta. *Int J Radiat Oncol Biol Phys* **50**, 899-908 (2001).

128. Hauer-Jensen, M., Kong, F.M., Fink, L.M. & Anscher, M.S. Circulating thrombomodulin during radiation therapy of lung cancer. *Radiat Oncol Investig* **7**, 238-242 (1999).

129. Paris, F. et al. Endothelial apoptosis as the primary lesion initiating intestinal radiation damage in mice. *Science* **293**, 293-297 (2001).

130. Eifel, P.J., Donaldson, S.S. & Thomas, P.R. Response of growing bone to irradiation: a proposed late effects scoring system. *Int J Radiat Oncol Biol Phys* **31**, 1301-1307 (1995).

131. Johansson, S., Svensson, H. & Denekamp, J. Timescale of evolution of late radiation injury after postoperative radiotherapy of breast cancer patients. *Int J Radiat Oncol Biol Phys* **48**, 745-750 (2000).

132. Wachsberger, P., Burd, R. & Dicker, A.P. Tumor response to ionizing radiation combined with antiangiogenesis or vascular targeting agents: exploring mechanisms of interaction. *Clin Cancer Res* **9**, 1957-1971 (2003).

133. Nittby, H. et al. Increased blood-brain barrier permeability in mammalian brain 7 days after exposure to the radiation from a GSM-900 mobile phone. *Pathophysiology* **16**, 103-112 (2009).

134. Moding, E.J. et al. Dual-energy micro-computed tomography imaging of radiation-induced vascular changes in primary mouse sarcomas. *Int J Radiat Oncol Biol Phys* **85**, 1353-1359.

135. Barcellos-Hoff, M.H. How do tissues respond to damage at the cellular level? The role of cytokines in irradiated tissues. *Radiat Res* **150**, S109-120 (1998).

136. Meyn, R.E., Stephens, L.C., Hunter, N.R., Ang, K.K. & Milas, L. Reemergence of apoptotic cells between fractionated doses in irradiated murine tumors. *Int J Radiat Oncol Biol Phys* **30**, 619-624 (1994).

137. Ling, C.C., Guo, M., Chen, C.H. & Deloherey, T. Radiation-induced apoptosis: effects of cell age and dose fractionation. *Cancer Res* **55**, 5207-5212 (1995).

138. Rupnow, B.A., Murtha, A.D., Alarcon, R.M., Giaccia, A.J. & Knox, S.J. Direct evidence that apoptosis enhances tumor responses to fractionated radiotherapy. *Cancer Res* **58**, 1779-1784 (1998).

139. Thames, H.D., Jr., Peters, L.J., Withers, H.R. & Fletcher, G.H. Accelerated fractionation vs hyperfractionation: rationales for several treatments per day. *Int J Radiat Oncol Biol Phys* **9**, 127-138 (1983).

140. Thames, H.D., Jr., Withers, H.R., Peters, L.J. & Fletcher, G.H. Changes in early and late radiation responses with altered dose fractionation: implications for dose-survival relationships. *Int J Radiat Oncol Biol Phys* **8**, 219-226 (1982).

141. Saunders, M. et al. Continuous hyperfractionated accelerated radiotherapy (CHART) versus conventional radiotherapy in non-small-cell lung cancer: a randomised multicentre trial. CHART Steering Committee. *Lancet* **350**, 161-165 (1997).

142. Saunders, M. et al. Continuous, hyperfractionated, accelerated radiotherapy (CHART) versus conventional radiotherapy in non-small cell lung cancer: mature

data from the randomised multicentre trial. CHART Steering committee. *Radiother Oncol* **52**, 137-148 (1999).

143. Fletcher, G.H. Regaud lecture perspectives on the history of radiotherapy. *Radiother Oncol* **12**, iii-v, 253-271 (1988).

144. Friberg, S. & Ruden, B.I. Hypofractionation in radiotherapy. An investigation of injured Swedish women, treated for cancer of the breast. *Acta Oncol* **48**, 822-831 (2009).

145. Galecki, J., Hicer-Grzenkowicz, J., Grudzien-Kowalska, M., Michalska, T. & Zalucki, W. Radiation-induced brachial plexopathy and hypofractionated regimens in adjuvant irradiation of patients with breast cancer--a review. *Acta Oncol* **45**, 280-284 (2006).

146. Johansson, S. Radiation induced brachial plexopathies. *Acta Oncol* **45**, 253-257 (2006).

147. Lee, W.R. Prostate cancer and the hypofractionation hypothesis. *J Clin Oncol* **31**, 3849-3851 (2013).

148. Whelan, T.J. et al. Long-term results of hypofractionated radiation therapy for breast cancer. *N Engl J Med* **362**, 513-520 (2010).

149. Fowler, J.F. The first James Kirk memorial lecture. What next in fractionated radiotherapy? *Br J Cancer Suppl* **6**, 285-300 (1984).

150. Cox, R., Masson, W.K., Weichselbaum, R.R., Nove, J. & Little, J.B. The repair of potentially lethal damage in x-irradiated cultures of normal and ataxia telangiectasia human fibroblasts. *Int J Radiat Biol Relat Stud Phys Chem Med* **39**, 357-365 (1981).

151. Weichselbaum, R.R., Nove, J. & Little, J.B. X-ray sensitivity of fifty-three human diploid fibroblast cell strains from patients with characterized genetic disorders. *Cancer Res* **40**, 920-925 (1980).

152. Obedian, E., Fischer, D.B. & Haffty, B.G. Second malignancies after treatment of early-stage breast cancer: lumpectomy and radiation therapy versus mastectomy. *J Clin Oncol* **18**, 2406-2412 (2000).

153. Walter, A.W. et al. Secondary brain tumors in children treated for acute lymphoblastic leukemia at St Jude Children's Research Hospital. *J Clin Oncol* **16**, 3761-3767 (1998).

154. Salloum, E. et al. Second solid tumors in patients with Hodgkin's disease cured after radiation or chemotherapy plus adjuvant low-dose radiation. *J Clin Oncol* **14**, 2435-2443 (1996).

155. Inskip, P.D., Stovall, M. & Flannery, J.T. Lung cancer risk and radiation dose among women treated for breast cancer. *J Natl Cancer Inst* **86**, 983-988 (1994).

156. Dawson, L.A. & Sharpe, M.B. Image-guided radiotherapy: rationale, benefits, and limitations. *Lancet Oncol* **7**, 848-858 (2006).

157. Wardman, P. Chemical radiosensitizers for use in radiotherapy. *Clin Oncol (R Coll Radiol)* **19**, 397-417 (2007).

158. Bennett, M., Feldmeier, J., Smee, R. & Milross, C. Hyperbaric oxygenation for tumour sensitisation to radiotherapy. *Cochrane Database Syst Rev*, CD005007 (2005).

159. Stea, B., Suh, J.H., Boyd, A.P., Cagnoni, P.J. & Shaw, E. Whole-brain radiotherapy with or without efaproxiral for the treatment of brain metastases:

Determinants of response and its prognostic value for subsequent survival. *Int J Radiat Oncol Biol Phys* **64**, 1023-1030 (2006).

160. Wardman, P., Rothkamm, K., Folkes, L.K., Woodcock, M. & Johnston, P.J. Radiosensitization by nitric oxide at low radiation doses. *Radiat Res* **167**, 475-484 (2007).

161. Stewart, F.A., Denekamp, J. & Randhawa, V.S. Skin sensitization by misonidazole: a demonstration of uniform mild hypoxia. *Br J Cancer* **45**, 869-877 (1982).

162. Chassagne, D., Charreau, I., Sancho-Garnier, H., Eschwege, F. & Malaise, E.P. First analysis of tumor regression for the European randomized trial of etanidazole combined with radiotherapy in head and neck carcinomas. *Int J Radiat Oncol Biol Phys* **22**, 581-584 (1992).

163. Murayama, C. et al. Radiosensitization by a new potent nucleoside analog: 1-(1',3',4'-trihydroxy-2'-butoxy)methyl-2-nitroimidazole(RP-343). *Int J Radiat Oncol Biol Phys* **26**, 433-443 (1993).

164. Murayama, C. et al. Radiosensitization by a new nucleoside analogue: 1-[2-hydroxy-1-(hydroxymethyl)ethoxy]methyl-2-nitroimidazole (RP-170). *Int J Radiat Oncol Biol Phys* **17**, 575-581 (1989).

165. Kvols, L.K. Radiation sensitizers: a selective review of molecules targeting DNA and non-DNA targets. *J Nucl Med* **46 Suppl 1**, 187S-190S (2005).

166. Servidei, T. et al. The novel trinuclear platinum complex BBR3464 induces a cellular response different from cisplatin. *Eur J Cancer* **37**, 930-938 (2001).

167. Richmond, R.C. Toxic variability and radiation sensitization by dichlorodiammineplatinum(II) complexes in Salmonella typhimurium cells. *Radiat Res* **99**, 596-608 (1984).

168. Amorino, G.P., Freeman, M.L., Carbone, D.P., Lebwohl, D.E. & Choy, H. Radiopotentiation by the oral platinum agent, JM216: role of repair inhibition. *Int J Radiat Oncol Biol Phys* **44**, 399-405 (1999).

169. Ostruszka, L.J. & Shewach, D.S. The role of cell cycle progression in radiosensitization by 2',2'-difluoro-2'-deoxycytidine. *Cancer Res* **60**, 6080-6088 (2000).

170. Chen, A.Y., Choy, H. & Rothenberg, M.L. DNA topoisomerase I-targeting drugs as radiation sensitizers. *Oncology (Williston Park)* **13**, 39-46 (1999).

171. Lespinasse, F., Biscay, P., Malaise, E.P. & Guichard, M. SR-2508 plus buthionine sulfoximine or SR-2508 alone: effects on the radiation response and the glutathione content of a human tumor xenograft. *Radiat Res* **110**, 149-154 (1987).

172. Ono, K. et al. Radiosensitizing effect of misonidazole in combination with an inhibitor of glutathione synthesis in murine tumors. *Int J Radiat Oncol Biol Phys* **12**, 1661-1666 (1986).

173. Minchinton, A.I. et al. Glutathione depletion in tissues after administration of buthionine sulphoximine. *Int J Radiat Oncol Biol Phys* **10**, 1261-1264 (1984).

174. Rojas, A. et al. Enhancement of misonidazole radiosensitization by buthionine sulphoximine. *Radiother Oncol* **2**, 325-332 (1984).

175. Javvadi, P., Segan, A.T., Tuttle, S.W. & Koumenis, C. The chemopreventive agent curcumin is a potent radiosensitizer of human cervical tumor cells via increased reactive oxygen species production and overactivation of the mitogen-activated protein kinase pathway. *Mol Pharmacol* **73**, 1491-1501 (2008).

176. Inano, H. et al. Potent preventive action of curcumin on radiation-induced initiation of mammary tumorigenesis in rats. *Carcinogenesis* **21**, 1835-1841 (2000).

177. Shehzad, A., Park, J.W., Lee, J. & Lee, Y.S. Curcumin induces radiosensitivity of in vitro and in vivo cancer models by modulating pre-mRNA processing factor 4 (Prp4). *Chem Biol Interact* **206**, 394-402 (2013).

178. Tanabe, K., Makimura, Y., Tachi, Y., Imagawa-Sato, A. & Nishimoto, S. Hypoxia-selective activation of 5-fluorodeoxyuridine prodrug possessing indolequinone structure: radiolytic reduction and cytotoxicity characteristics. *Bioorg Med Chem Lett* **15**, 2321-2324 (2005).

179. Sykes, B.M. et al. N-Substituted 2-(2,6-dinitrophenylamino)propanamides: novel prodrugs that release a primary amine via nitroreduction and intramolecular cyclization. *J Med Chem* **42**, 346-355 (1999).

180. Ahn, G.O., Ware, D.C., Denny, W.A. & Wilson, W.R. Optimization of the auxiliary ligand shell of Cobalt(III)(8-hydroxyquinoline) complexes as model hypoxia-selective radiation-activated prodrugs. *Radiat Res* **162**, 315-325 (2004).

181. Kobayashi, K., Usami, N., Porcel, E., Lacombe, S. & Le Sech, C. Enhancement of radiation effect by heavy elements. *Mutat Res* **704**, 123-131 (2010).

182. Usami, N. et al. Fast He2+ ion irradiation of DNA loaded with platinum-containing molecules. *Int J Radiat Biol* **81**, 515-522 (2005).

183. Richards, G.M. & Mehta, M.P. Motexafin gadolinium in the treatment of brain metastases. *Expert Opin Pharmacother* **8**, 351-359 (2007).

184. Ji, S.R. et al. Carbon nanotubes in cancer diagnosis and therapy. *Biochim Biophys Acta* **1806**, 29-35 (2010).

185. Porcel, E. et al. Platinum nanoparticles: a promising material for future cancer therapy? *Nanotechnology* **21**, 85103 (2010).

186. Le Duc, G. et al. Toward an image-guided microbeam radiation therapy using gadolinium-based nanoparticles. *ACS Nano* **5**, 9566-9574 (2011).

187. Fan, W. et al. Rattle-structured multifunctional nanotheranostics for synergetic chemo-/radiotherapy and simultaneous magnetic/luminescent dual-mode imaging. *J Am Chem Soc* **135**, 6494-6503 (2013).

188. Hainfeld, J.F., Slatkin, D.N. & Smilowitz, H.M. The use of gold nanoparticles to enhance radiotherapy in mice. *Phys Med Biol* **49**, N309-315 (2004).

189. Pautler, M. & Brenner, S. Nanomedicine: promises and challenges for the future of public health. *Int J Nanomedicine* **5**, 803-809 (2010).

190. Barenholz, Y. Doxil(R)--the first FDA-approved nano-drug: lessons learned. *J Control Release* **160**, 117-134 (2012).

191. Kanekiyo, M. et al. Self-assembling influenza nanoparticle vaccines elicit broadly neutralizing H1N1 antibodies. *Nature* **499**, 102-106 (2013).

192. des Rieux, A., Fievez, V., Garinot, M., Schneider, Y.J. & Preat, V. Nanoparticles as potential oral delivery systems of proteins and vaccines: a mechanistic approach. *J Control Release* **116**, 1-27 (2006).

193. Kircher, M.F. et al. A brain tumor molecular imaging strategy using a new triple-modality MRI-photoacoustic-Raman nanoparticle. *Nat Med* **18**, 829-834 (2012).

194. Jiang, S., Gnanasammandhan, M.K. & Zhang, Y. Optical imaging-guided cancer therapy with fluorescent nanoparticles. *J R Soc Interface* **7**, 3-18 (2010).

195. Reddy, G.R. et al. Vascular targeted nanoparticles for imaging and treatment of brain tumors. *Clin Cancer Res* **12**, 6677-6686 (2006).

196. Cheng, Z., Al Zaki, A., Hui, J.Z., Muzykantov, V.R. & Tsourkas, A. Multifunctional nanoparticles: cost versus benefit of adding targeting and imaging capabilities. *Science* **338**, 903-910 (2012).

197. Ulijn, R.V. & Smith, A.M. Designing peptide based nanomaterials. *Chem Soc Rev* **37**, 664-675 (2008).

198. Giljohann, D.A. et al. Gold nanoparticles for biology and medicine. *Angew Chem Int Ed Engl* **49**, 3280-3294 (2010).

199. Jeremic, B., Aguerri, A.R. & Filipovic, N. Radiosensitization by gold nanoparticles. *Clin Transl Oncol* **15**, 593-601 (2013).

200. Dorsey, J.F. et al. Gold nanoparticles in radiation research: potential applications for imaging and radiosensitization. *Transl Can Res* **2** (2013).

201. Hebert, E.M., Debouttiere, P.J., Lepage, M., Sanche, L. & Hunting, D.J. Preferential tumour accumulation of gold nanoparticles, visualised by Magnetic

Resonance Imaging: radiosensitisation studies in vivo and in vitro. *Int J Radiat Biol* **86**, 692-700 (2010).

202. Hainfeld, J.F. et al. Gold nanoparticles enhance the radiation therapy of a murine squamous cell carcinoma. *Phys Med Biol* **55**, 3045-3059 (2010).

203. Joh, D.Y. et al. Theranostic gold nanoparticles modified for durable systemic circulation effectively and safely enhance the radiation therapy of human sarcoma cells and tumors. *Transl Oncol* **6**, 722-731 (2013).

204. Sadauskas, E. et al. Protracted elimination of gold nanoparticles from mouse liver. *Nanomedicine* **5**, 162-169 (2009).

205. Balasubramanian, S.K. et al. Biodistribution of gold nanoparticles and gene expression changes in the liver and spleen after intravenous administration in rats. *Biomaterials* **31**, 2034-2042 (2010).

206. Goel, R., Shah, N., Visaria, R., Paciotti, G.F. & Bischof, J.C. Biodistribution of TNF-alpha-coated gold nanoparticles in an in vivo model system. *Nanomedicine (Lond)* **4**, 401-410 (2009).

207. Sadauskas, E. et al. Kupffer cells are central in the removal of nanoparticles from the organism. *Part Fibre Toxicol* **4**, 10 (2007).

208. Semmler-Behnke, M. et al. Biodistribution of 1.4- and 18-nm gold particles in rats. *Small* **4**, 2108-2111 (2008).

209. Hainfeld, J.F., Slatkin, D.N., Focella, T.M. & Smilowitz, H.M. Gold nanoparticles: a new X-ray contrast agent. *Br J Radiol* **79**, 248-253 (2006).

210. Mesbahi, A. A review on gold nanoparticles radiosensitization effect in radiation therapy of cancer. *Rep Pract Oncol Radiother* **15**, 176-180 (2010).

211. Butterworth, K.T., McMahon, S.J., Currell, F.J. & Prise, K.M. Physical basis and biological mechanisms of gold nanoparticle radiosensitization. *Nanoscale* **4**, 4830-4838 (2012).

212. Adams, F.H., Norman, A., Mello, R.S. & Bass, D. Effect of radiation and contrast media on chromosomes. Preliminary report. *Radiology* **124**, 823-826 (1977).

213. Chithrani, D.B. et al. Gold nanoparticles as radiation sensitizers in cancer therapy. *Radiat Res* **173**, 719-728 (2010).

214. Nath, R., Bongiorni, P. & Rockwell, S. Iododeoxyuridine radiosensitization by low- and high-energy photons for brachytherapy dose rates. *Radiat Res* **124**, 249-258 (1990).

215. Polf, J.C. et al. Enhanced relative biological effectiveness of proton radiotherapy in tumor cells with internalized gold nanoparticles. *Appl Phys Lett* **98**, 193702 (2011).

216. Roa, W. et al. Gold nanoparticle sensitize radiotherapy of prostate cancer cells by regulation of the cell cycle. *Nanotechnology* **20**, 375101 (2009).

217. Kang, B., Mackey, M.A. & El-Sayed, M.A. Nuclear targeting of gold nanoparticles in cancer cells induces DNA damage, causing cytokinesis arrest and apoptosis. *J Am Chem Soc* **132**, 1517-1519 (2010).

218. Berbeco, R.I., Ngwa, W. & Makrigiorgos, G.M. Localized dose enhancement to tumor blood vessel endothelial cells via megavoltage X-rays and targeted gold nanoparticles: new potential for external beam radiotherapy. *Int J Radiat Oncol Biol Phys* **81**, 270-276 (2011).

219. Robar, J.L., Riccio, S.A. & Martin, M.A. Tumour dose enhancement using modified megavoltage photon beams and contrast media. *Phys Med Biol* **47**, 2433-2449 (2002).

220. Ngwa, W., Makrigiorgos, G.M. & Berbeco, R.I. Applying gold nanoparticles as tumor-vascular disrupting agents during brachytherapy: estimation of endothelial dose enhancement. *Phys Med Biol* **55**, 6533-6548 (2010).

221. Cho, S.H., Jones, B.L. & Krishnan, S. The dosimetric feasibility of gold nanoparticle-aided radiation therapy (GNRT) via brachytherapy using low-energy gamma-/x-ray sources. *Phys Med Biol* **54**, 4889-4905 (2009).

222. Bahreyni Toossi, M.T. et al. A Monte Carlo study on tissue dose enhancement in brachytherapy: a comparison between gadolinium and gold nanoparticles. *Australas Phys Eng Sci Med* **35**, 177-185 (2012).

223. Cho, S.H. Estimation of tumour dose enhancement due to gold nanoparticles during typical radiation treatments: a preliminary Monte Carlo study. *Phys Med Biol* **50**, N163-173 (2005).

224. Leung, M.K. et al. Irradiation of gold nanoparticles by x-rays: Monte Carlo simulation of dose enhancements and the spatial properties of the secondary electrons production. *Med Phys* **38**, 624-631 (2011).

225. Tsiamas, P. et al. Low-Z linac targets for low-MV gold nanoparticle radiation therapy. *Med Phys* **41**, 021701 (2014).

226. Jain, S. et al. Cell-specific radiosensitization by gold nanoparticles at megavoltage radiation energies. *Int J Radiat Oncol Biol Phys* **79**, 531-539 (2011).

227. McMahon, S.J. et al. Nanodosimetric effects of gold nanoparticles in megavoltage radiation therapy. *Radiother Oncol* **100**, 412-416 (2011).

228. Maeda, H., Wu, J., Sawa, T., Matsumura, Y. & Hori, K. Tumor vascular permeability and the EPR effect in macromolecular therapeutics: a review. *J Control Release* **65**, 271-284 (2000).

229. Konerding, M.A., Fait, E. & Gaumann, A. 3D microvascular architecture of pre-cancerous lesions and invasive carcinomas of the colon. *Br J Cancer* **84**, 1354-1362 (2001).

230. Regulla, D.F., Hieber, L.B. & Seidenbusch, M. Physical and biological interface dose effects in tissue due to X-ray-induced release of secondary radiation from metallic gold surfaces. *Radiat Res* **150**, 92-100 (1998).

231. Brun, E., Sanche, L. & Sicard-Roselli, C. Parameters governing gold nanoparticle X-ray radiosensitization of DNA in solution. *Colloids Surf B Biointerfaces* **72**, 128-134 (2009).

232. Rahman, W.N. et al. Enhancement of radiation effects by gold nanoparticles for superficial radiation therapy. *Nanomedicine* **5**, 136-142 (2009).

233. Zheng, Y., Hunting, D.J., Ayotte, P. & Sanche, L. Radiosensitization of DNA by gold nanoparticles irradiated with high-energy electrons. *Radiat Res* **169**, 19-27 (2008).

234. Ngwa, W. et al. In vitro radiosensitization by gold nanoparticles during continuous low-dose-rate gamma irradiation with I-125 brachytherapy seeds. *Nanomedicine* **9**, 25-27 (2013).

235. Chattopadhyay, N. et al. Molecularly targeted gold nanoparticles enhance the radiation response of breast cancer cells and tumor xenografts to X-radiation. *Breast Cancer Res Treat* **137**, 81-91 (2013).

236. Hossain, M. & Su, M. Nanoparticle location and material dependent dose enhancement in X-ray radiation therapy. *J Phys Chem C Nanomater Interfaces* **116**, 23047-23052 (2012).

237. Chattopadhyay, N. et al. Design and characterization of HER-2-targeted gold nanoparticles for enhanced X-radiation treatment of locally advanced breast cancer. *Mol Pharm* **7**, 2194-2206 (2010).

238. Kong, T. et al. Enhancement of radiation cytotoxicity in breast-cancer cells by localized attachment of gold nanoparticles. *Small* **4**, 1537-1543 (2008).

239. Geng, F. et al. Thio-glucose bound gold nanoparticles enhance radio-cytotoxic targeting of ovarian cancer. *Nanotechnology* **22**, 285101 (2011).

240. Liu, C.J. et al. Enhancement of cell radiation sensitivity by pegylated gold nanoparticles. *Phys Med Biol* **55**, 931-945 (2010).

241. Butterworth, K.T. et al. Evaluation of cytotoxicity and radiation enhancement using 1.9 nm gold particles: potential application for cancer therapy. *Nanotechnology* **21**, 295101 (2010).

242. Zhang, X. et al. Enhanced radiation sensitivity in prostate cancer by gold-nanoparticles. *Clin Invest Med* **31**, E160-167 (2008).

243. Chang, M.Y. et al. Increased apoptotic potential and dose-enhancing effect of gold nanoparticles in combination with single-dose clinical electron beams on tumor-bearing mice. *Cancer Sci* **99**, 1479-1484 (2008).

244. Chien, C.C. et al. Synchrontron Radiation Instrumentation: Ninth International Conference on Synchrontron Radiation Instrumentation. **879** (2006).

245. Zhang, X.D. et al. Irradiation stability and cytotoxicity of gold nanoparticles for radiotherapy. *Int J Nanomedicine* **4**, 165-173 (2009).

246. Liu, C.J. et al. Enhanced x-ray irradiation-induced cancer cell damage by gold nanoparticles treated by a new synthesis method of polyethylene glycol modification. *Nanotechnology* **19**, 295104 (2008).

247. Zhang, X.D. et al. Enhanced tumor accumulation of sub-2 nm gold nanoclusters for cancer radiation therapy. *Adv Healthc Mater* **3**, 133-141 (2014).

248. Zhang, X.D. et al. Size-dependent radiosensitization of PEG-coated gold nanoparticles for cancer radiation therapy. *Biomaterials* **33**, 6408-6419 (2012).

249. Joh, D.Y. et al. Selective targeting of brain tumors with gold nanoparticle-induced radiosensitization. *PLoS One* **8**, e62425 (2013).

250. Kim, J.K. et al. Enhanced proton treatment in mouse tumors through proton irradiated nanoradiator effects on metallic nanoparticles. *Phys Med Biol* **57**, 8309-8323 (2012).

251. Atkinson, R.L. et al. Thermal enhancement with optically activated gold nanoshells sensitizes breast cancer stem cells to radiation therapy. *Sci Transl Med* **2**, 55ra79 (2010).

252. Rutten, A. & Prokop, M. Contrast agents in X-ray computed tomography and its applications in oncology. *Anticancer Agents Med Chem* **7**, 307-316 (2007).

253. Sako, M. et al. Basic research of iodinated starch as a potential contrast material for blood pool opacification of tissue and for indirect lymphography. *Osaka: Excerpta Medica*, 24-28 (1990).

254. Nottelet, B., Coudane, J. & Vert, M. Synthesis of an X-ray opaque biodegradable copolyester by chemical modification of poly (epsilon-caprolactone). *Biomaterials* **27**, 4948-4954 (2006).

255. Speck, U. Contrast agents: X-ray contrast agents and molecular imaging--a contradiction? *Handb Exp Pharmacol*, 167-175 (2008).

256. Adam, G. et al. Gd-DTPA-cascade-polymer: potential blood pool contrast agent for MR imaging. *J Magn Reson Imaging* **4**, 462-466 (1994).

257. Vera, D.R. & Mattrey, R.F. A molecular CT blood pool contrast agent. *Acad Radiol* **9**, 784-792 (2002).

258. Chanda, N. et al. Bombesin functionalized gold nanoparticles show in vitro and in vivo cancer receptor specificity. *Proc Natl Acad Sci U S A* **107**, 8760-8765.

259. Eck, W., Nicholson, A.I., Zentgraf, H., Semmler, W. & Bartling, S. Anti-CD4-targeted gold nanoparticles induce specific contrast enhancement of peripheral lymph nodes in X-ray computed tomography of live mice. *Nano Lett* **10**, 2318-2322 (2010).

260. Elrod, D.B., Partha, R., Danila, D., Casscells, S.W. & Conyers, J.L. An iodinated liposomal computed tomographic contrast agent prepared from a diiodophosphatidylcholine lipid. *Nanomedicine* **5**, 42-45 (2009).

261. Benita, S., Poly, P.A., Puisieux, F. & Delattre, J. Radiopaque liposomes: effect of formulation conditions on encapsulation efficiency. *J Pharm Sci* **73**, 1751-1755 (1984).

262. Torchilin, V.P., Frank-Kamenetsky, M.D. & Wolf, G.L. CT visualization of blood pool in rats by using long-circulating, iodine-containing micelles. *Acad Radiol* **6**, 61-65 (1999).

263. Long, D.M., Jr., Lasser, E.C., Sharts, C.M., Multer, F.K. & Nielsen, M. Experiments with radiopaque perfluorocarbon emulsions for selective opacification of organs and total body angiography. *Invest Radiol* **15**, 242-247 (1980).

264. Patronas, N.J., Hekmatpanah, J. & Doi, K. Brain-tumor imaging using radiopaque perfluorocarbon. A preliminary report. *J Neurosurg* **58**, 650-653 (1983).

265. Rabin, O., Manuel Perez, J., Grimm, J., Wojtkiewicz, G. & Weissleder, R. An X-ray computed tomography imaging agent based on long-circulating bismuth sulphide nanoparticles. *Nat Mater* **5**, 118-122 (2006).

266. Jackson, P.A., Rahman, W.N., Wong, C.J., Ackerly, T. & Geso, M. Potential dependent superiority of gold nanoparticles in comparison to iodinated contrast agents. *Eur J Radiol* **75**, 104-109 (2010).

267. Cai, Q.Y. et al. Colloidal gold nanoparticles as a blood-pool contrast agent for X-ray computed tomography in mice. *Invest Radiol* **42**, 797-806 (2007).

268. Kim, D., Park, S., Lee, J.H., Jeong, Y.Y. & Jon, S. Antibiofouling polymer-coated gold nanoparticles as a contrast agent for in vivo X-ray computed tomography imaging. *J Am Chem Soc* **129**, 7661-7665 (2007).

269. Oh, M.H. et al. Large-scale synthesis of bioinert tantalum oxide nanoparticles for X-ray computed tomography imaging and bimodal image-guided sentinel lymph node mapping. *J Am Chem Soc* **133**, 5508-5515 (2011).

270. Weinstein, J.S. et al. Superparamagnetic iron oxide nanoparticles: diagnostic magnetic resonance imaging and potential therapeutic applications in neurooncology and central nervous system inflammatory pathologies, a review. *J Cereb Blood Flow Metab* **30**, 15-35 (2010).

271. Hyeon, T., Lee, S.S., Park, J., Chung, Y. & Na, H.B. Synthesis of highly crystalline and monodisperse maghemite nanocrystallites without a size-selection process. *J Am Chem Soc* **123**, 12798-12801 (2001).

272. Thorek, D.L., Chen, A.K., Czupryna, J. & Tsourkas, A. Superparamagnetic iron oxide nanoparticle probes for molecular imaging. *Ann Biomed Eng* **34**, 23-38 (2006).

273. Wang, Y.X., Hussain, S.M. & Krestin, G.P. Superparamagnetic iron oxide contrast agents: physicochemical characteristics and applications in MR imaging. *Eur Radiol* **11**, 2319-2331 (2001).

274. Will, O. et al. Diagnostic precision of nanoparticle-enhanced MRI for lymph-node metastases: a meta-analysis. *Lancet Oncol* **7**, 52-60 (2006).

275. Saksena, M.A., Saokar, A. & Harisinghani, M.G. Lymphotropic nanoparticle enhanced MR imaging (LNMRI) technique for lymph node imaging. *Eur J Radiol* **58**, 367-374 (2006).

276. Crayton, S.H. & Tsourkas, A. pH-titratable superparamagnetic iron oxide for improved nanoparticle accumulation in acidic tumor microenvironments. *ACS Nano* **5**, 9592-9601 (2011).

277. Nasongkla, N. et al. Multifunctional polymeric micelles as cancer-targeted, MRI-ultrasensitive drug delivery systems. *Nano Lett* **6**, 2427-2430 (2006).

278. Talelli, M. et al. Superparamagnetic iron oxide nanoparticles encapsulated in biodegradable thermosensitive polymeric micelles: toward a targeted nanomedicine suitable for image-guided drug delivery. *Langmuir* **25**, 2060-2067 (2009).

279. Torchilin, V.P. PEG-based micelles as carriers of contrast agents for different imaging modalities. *Adv Drug Deliv Rev* **54**, 235-252 (2002).

280. Otsuka, H., Nagasaki, Y. & Kataoka, K. PEGylated nanoparticles for biological and pharmaceutical applications. *Adv Drug Deliv Rev* **55**, 403-419 (2003).

281. Oerlemans, C. et al. Polymeric micelles in anticancer therapy: targeting, imaging and triggered release. *Pharm Res* **27**, 2569-2589 (2010).

282. Klibanov, A.L., Maruyama, K., Torchilin, V.P. & Huang, L. Amphipathic polyethyleneglycols effectively prolong the circulation time of liposomes. *FEBS Lett* **268**, 235-237 (1990).

283. Diao, Y.Y. et al. Doxorubicin-loaded PEG-PCL copolymer micelles enhance cytotoxicity and intracellular accumulation of doxorubicin in adriamycin-resistant tumor cells. *Int J Nanomedicine* **6**, 1955-1962.

284. Jones, M. & Leroux, J. Polymeric micelles - a new generation of colloidal drug carriers. *Eur J Pharm Biopharm* **48**, 101-111 (1999).

285. Trubetskoy, V.S. Polymeric micelles as carriers of diagnostic agents. *Adv Drug Deliv Rev* **37**, 81-88 (1999).

Chapter 2: Development of Gold-Loaded Polymeric Micelles for Computed Tomography–Guided Radiation Therapy Treatment and Radiosensitization

2.1 Abstract

Gold nanoparticles (AuNPs) have generated interest as both imaging and therapeutic agents. AuNPs are attractive for imaging applications since they are nontoxic and provide nearly three times greater X-ray attenuation per unit weight than iodine. As therapeutic agents, AuNPs can sensitize tumor cells to ionizing radiation. To create a nanoplatform that could simultaneously exhibit long circulation times, achieve appreciable tumor accumulation, generate computed tomography (CT) image contrast, and serve as a radiosensitizer, gold-loaded polymeric micelles (GPMs) were prepared. Specifically, 1.9 nm AuNPs were encapsulated within the hydrophobic core of micelles formed with the amphiphilic diblock copolymer poly(ethylene glycol)-*b*-poly(ε-caprolactone). GPMs were produced with low polydispersity and mean hydrodynamic diameters ranging from 25 to 150 nm. Following intravenous injection, GPMs provided blood pool contrast for up to 24 hours and improved the delineation of tumor margins *via* CT. Thus, GPM-enhanced CT imaging was used to guide radiation therapy delivered *via*

a Small Animal Radiation Research Platform. In combination with the radiosensitizing capabilities of gold, tumor-bearing mice exhibited a 1.7-fold improvement in the median survival time, compared with mice receiving radiation alone. It is envisioned that translation of these capabilities to human cancer patients could guide and enhance the efficacy of radiation therapy.

2.2 Introduction

Over the past two decades, many nanoparticle formulations have been evaluated as computed tomography (CT) contrast agents, including liposomes loaded with iodinated compounds,[1-3] polymeric iodine-containing poly(ethylene glycol) (PEG)-based micelles,[4] iodine-containing perfluorocarbons,[5, 6] bismuth sulfide nanoparticles,[7] and gold nanoparticles (AuNPs).[8-10] Of these, gold nanoparticles have garnered a particularly high degree of interest. This is largely due to the high mass attenuation coefficient of gold, which is ~ 2.7-fold higher than iodine.[11] Accordingly, it has been found that 30nm AuNPs can attenuate 120 kVp x-rays 5.7 times more than the iodine-based agent, Ultravist.[10] Additional benefits of working with AuNPs include the ability to finely tune their size and shape and modify their surface with various functional groups. While other nanoparticle formulations, such as bismuth sulfide nanoparticles, may also exhibit a higher x-ray absorption than iodine, it is difficult to control their size and there is a lack of chemical methods to modify their surface.[10, 12] Surface chemistry is important when attempting to prolong systemic circulation, a prerequisite for tumor imaging and tumor accumulation *via* the enhanced permeability and retention (EPR) effect.[13] An extended circulation also offers an opportunity to image the reticuloendothelial system (RES), the blood pool, and in some cases the lymph system.

In addition to their use as CT contrast agents, AuNPs have also shown promise as radiosensitizers. Radiosensitization is due to the high absorbance of gold and the resulting deposition of energy in surrounding tissues from photoelectrons (*i.e.*

photoelectric effect), Auger electrons, and the generation of free radicals.[14, 15] Within the kilovoltage energy range, the radiosensitization effect is generally attributable to the photoelectric effect while Auger electrons are hypothesized to be responsible for energy radiosensitization within the megavoltage range of radiation energies.[16-19] It has been shown that AuNPs in combination with radiation treatment can lead to an increase in the number of DNA double-stranded breaks compared with radiation alone.[14, 20-25] In one recent study it was shown that 1.9 nm AuNPs could even lead to an increase in the survival of tumor-bearing mice, compared with radiation therapy (RT) alone.[9] However, because of the rapid clearance of the small nanoparticles used in this study, the tumors had to be irradiated immediately after AuNP administration. In general, rapid clearance limits tumor-specific accumulation *via* EPR, and thus can limit the ability of small AuNPs to guide, via CT, the precise delivery of radiation therapy.

When designing a treatment plan, radiation oncologists must take into account several critical factors including the mapping of true tumor margins, which can sometimes be challenging to define using current imaging techniques. Therefore, a more accurate definition of tumor boundaries would facilitate more precise delivery of radiation therapy and as a result decrease normal tissue exposure to undesirable radiation.[26-28] With this goal in mind, it is envisioned that long-circulating AuNPs that appreciably accumulate in tumors *via* EPR can be used to guide RT planning and treatment, through improved contrast-enhanced delineation of tumor boundaries *via* CT, thus minimizing energy deposition in surrounding healthy tissues. In addition, AuNP-mediated radiosensitization can also directly increase the radiation dose received by the

tumor, thus providing a second complementary mechanism by which the overall therapeutic index can be increased.

In this study, we describe the development of a multifunctional micelle that simultaneously exhibits long circulation times, achieves appreciable tumor accumulation, generates CT image contrast, and serves as a sensitizer for radiation therapy in cellular and animal models at sublethal radiation doses. Specifically, using a microemulsion synthesis method, we have been able to prepare gold-loaded polymeric micelles (GPMs), with tunable hydrodynamic diameters ranging from 25 to 150 nm. The GPMs are formed using the amphiphilic diblock copolymer poly(ethylene glycol)-*b*-poly(ε-caprolactone) (PEG-*b*-PCL) and have tightly packed clusters of 1.9 nm AuNPs incorporated within the hydrophobic core (Figure 2.1). We first evaluated the ability of GPMs to enhance double-stranded DNA breaks *in vitro* in response to radiation. Next, we assessed whether GPMs are capable of generating contrast for CT blood pool and tumor imaging. Finally we investigated whether the radiosensitization in cells translated to an improvement in survivability in murine tumor xenograft models.

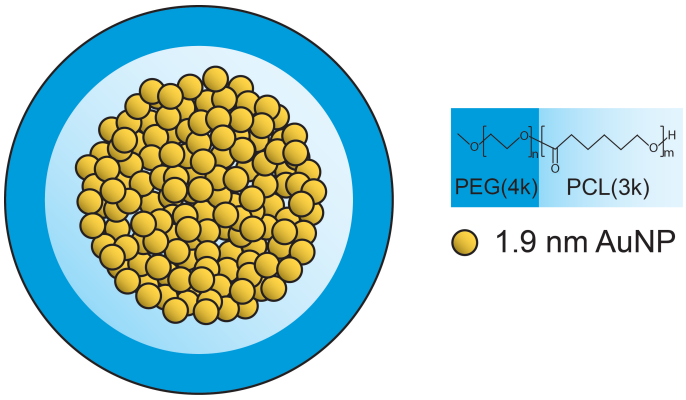

Figure 2.1. Schematic of gold-loaded polymeric micelles (GPMs). Gold nanoparticles are self-assembled into the hydrophobic core of micelles, stabilized with the amphiphilic diblock copolymer PEG-b-PCL.

Each GPM is composed of approximately hundreds to thousands of individual gold nanoparticles, depending on their size.

2.3 Materials and Methods

Synthesis of 1.9 nm gold AuNPs

Dodecanethiol capped AuNPs were prepared according to the procedure described by Brust *et. al*,[46] using a two phase reduction of tetrachloroaurate ($HAuCl_4$) by sodium borohydride ($NaBH_4$) in the presence of an alkanethiol. Briefly, 30 mL of an aqueous solution of 30 mM $HAuCl_4$ was mixed with 50 mM of tetraoctylammonium bromide (TOAB) in 80 mL of toluene. The solution was stirred until the $HAuCl_4$ solution transferred into the organic phase. Then, 0.84 mM of 1-dodecanethiol was added to the solution while stirring followed by the dropwise addition of a 0.4 M aqueous solution of $NaBH_4$. The resultant mixture was then stirred for at least 3 hours and precipitated twice at -20°C in ethanol overnight to remove excess thiols. The precipitate was collected *via* centrifugation and the supernatant was decanted. The remaining pellet was dissolved in toluene.

Synthesis of GPMs

Gold loaded polymeric micelles were synthesized using oil-in-water emulsions and stabilized using the amphiphilic diblock copolymer polyethylene glycol (4k) – polycaprolactone (3k) (PEG-*b*-PCL). AuNPs were dissolved in toluene at 30 mg Au/mL and PEG-*b*-PCL was also dissolved in toluene at a concentration of 50 mg/mL. A combined solution (200 µL) of the diblock (4 mg) and the AuNPs (3.5 mg) was added directly to a glass vial containing 4 mL of millipore water and the mixture was emulsified

for approximately 3 minutes in an ultrasonic bath. The emulsions were then allowed to stand overnight in a desiccator prior to their characterization and purification. The resulting dark brown solution was centrifuged at 400 RCF for 10 minutes to remove the largest micelles. The solution was then centrifuged twice at 3100 RCF for 30 minutes, after which the supernatant was removed, and the pellet was re-suspended in pH 7.4 phosphate buffered saline (PBS). Different size fractions were collected using different centrifugal rates. Free polymer and smaller sized particles were removed by diafiltration using a MidGee hoop cross flow cartridge with 750 kDa molecular weight cutoff (GE Healthcare, Piscataway, NJ, USA) and was then filtered through a 0.2 μm cellulose acetate membrane filter (Nalgene, Thermo Scientific) to remove any oversized particles. Finally the nanoparticles were concentrated using 50 kDa MWCO centrifugal filter units (Millipore, Billercia, MA, USA).

Physicochemical analysis of GPMs

GPM stock solutions were diluted in Millipore water and deposited on 200-mesh carbon coated copper grids (Polysciences, Warrington, PA) for TEM imaging using a JEOL 1010 transmission electron microscope operating at 80 kV. Stock samples of GPM were diluted in PBS for measuring the hydrodynamic diameter of the nanoparticles by dynamic light scattering (DLS). These measurements were acquired using a Zetasizer Nano-ZS (Malvern Instruments, Worcestershire, UK) using the non-invasive back-scatter (NIBS) mode. Zeta potential measurements were carried out by diluting GPM stock samples in PBS and the mean particle zeta potential was measured using a Zetasizer Nano-ZS.

Cell culture and γ-h2ax immunofluorescence

HT-1080 human fibrosarcoma cells (ATCC) were cultured and maintained in Dulbecco's modified Eagle's medium (DMEM), supplemented with 10% fetal bovine serum (FBS), 1% penicillin/streptomycin at 37°C and 5% CO_2. Cells in chamber slides were exposed to culture medium with 1 mM of AuNPs for 24 hours then irradiated using a Small Animal Radiation Research Platform (SARRP) (150 kVp, 15 mA). After 12 hours post-irradiation, cells were fixed with 10% neutral buffered formalin (Sigma-Aldrich) for 10 minutes. Cells were then rinsed with PBS, and the nuclei were stained with Hoechst 33342 (25 μM) for 15 minutes. The slides were permeabilized with 0.5% Triton X-100 in PBS and then exposed to blocking buffer (PBS, 0.5% Triton X-100, 5% normal chicken serum, 1% BSA) for 30 minutes at room temperature and subsequently incubated overnight at 4^oC with mouse monoclonal anti-phospho-histone γ-H2AX primary antibody (JBW301, Upstate) at 1:1500 dilution in PBS (with 0.5% Triton X-100 and 1% BSA). Cells were washed with PBS and then incubated with chicken anti-mouse Alexa 594 secondary antibody (Molecular Probes) at 1:1000 dilution in PBS (with 0.5% Triton X-100 and 1% BSA) for 1 hour at room temperature. After rinsing with PBS, the slides were mounted with Prolong Gold Antifade Reagent (Invitrogen) and coverslips. Fluorescence imaging was performed using a Deltavision Deconvolution microscope (Applied Precision) equipped with a 60x (1.42 NA) oil-immersion lens and thermoelectrically cooled 12-bit monochrome CCD camera. Images were recorded as z-stacks (0.3 μm steps). Following reconstructive deconvolution, the maximum values of the pixels were used to assemble two-dimensional projections. Foci were counted

automatically using ImageJ after applying a top-hat filter and constant value threshold based on unirradiated controls.

Clonogenic Assay

Cells were incubated for 24 hours in culture medium with or without 100 μg/mL of GPMs in 100 mm dishes and then irradiated with the SARRP (150 kVp, 15 mA) at the specified radiation doses (0 Gy, 2 Gy, 4 Gy and 6 Gy). After radiation, the cells were washed three times with PBS, trypsinized, and plated at predetermined densities. The plates were kept in a humidified incubator and maintained in a $37^{o}C$ and 5% CO_2 environment for 10 to 14 days. The cells were then stained with methylene blue and the resulting colonies counted. A colony by definition had n > 50 cells. The surviving fraction was calculated as (colonies counted) / (cells seeded x (plating efficiency/100)). Each point on the survival curve represents the mean surviving fraction from at least three replicates. The survival curves were fitted to a linear-quadratic equation: surviving fraction = $\exp[-(\alpha D+\beta D^2)]$. The sensitizer enhancement ratio (SER) was calculated as the ratio of the mean inactivation doses, defined as the dose at which there is 37% survival with and without GPMs.

Quantification of blood clearance via ICP-OES

Approximately 6 week old female nu/nu nude mice (n = 3) were used for the GPMs blood clearance experiments. The GPMs were injected retro-orbitally at a dose of approximately 100 ppm in 200 μL of injected solution. Prior to injection, an aliquot of the GPM solution was saved for inductively coupled plasma – optical emission spectroscopy (ICP-OES) for the determination of the gold concentration of injected

sample. Blood samples (10 μL each) were collected from each animal using the tail-nick method at 1 min, 10 min, 15 min, 30 min, 1 h, 2 h, 4 h, 8 h, 24 h, and 48 h post-injection.

Contrast Enhanced in vivo CT imaging and biodistribution analysis

Approximately 6 week old female nu/nu nude mice (Charles River Laboratory, Charles River, MS, USA) were maintained in accordance with the Institutional Animal Care and Use Committee of the University of Pennsylvania. Mice were anesthetized using isoflurane, and HT-1080 cells were injected subcutaneously into the back left flank (2×10^6 cells in 0.1 mL of PBS). Tumors were grown until the mean diameter was approximately 7 – 8 mm, and pre-contrast cone beam CT imaging was performed using a Small Animal Radiation Research Platform, SARRP (Gulmay Medical, Inc.). CT imaging was conducted at 50 kVp (0.5 mA), and 1440 projections were used to reconstruct the cone-beam images using the algorithm provided by the manufacturer. Immediately following the pre-contrast image acquisition, either GPMs or 1.9 nm AuroVist^{TM} gold nanoparticles (Nanoprobes, Yaphank,NY) were intravenously injected into the HT-1080 tumor-bearing mice (n = 3 for each group). Using isoflurane to anesthetize the mice, both contrast agents were administered by retro-orbital injection (650 mg Au/kg in 0.2 mL). Post-contrast images were collected 30 min, 24 h, and 48 h post-injection with the same imaging parameters used for pre-contrast images. After 48 hours, the animals were sacrificed and the tumors, livers, spleens, kidneys, hearts, and lungs were harvested. Tissue samples were thoroughly washed with PBS and blotted dry to minimize the contribution of any nanoparticles remaining in the bloodstream. The tissue were weighed and digested in HNO_3 overnight at 70°C. Following the overnight

digestion, HCl was added to dissolve the gold. Samples were diluted with Millipore water and analyzed for gold content using ICP-OES.

Toxicity studies

Approximately 6 week old female nu/nu nude mice were randomized into four groups of 3 animals per group receiving 650 mg Au/kg**,** or sham-injected with PBS. Animals were weighed and observed regularly for clinical signs for up to 1 week post-injection. Animals were euthanized by CO_2 at 1 day and 1 week after intravenous gold injections and 0.3 mL blood was removed from the right ventricle immediately after the cessation of breathing. Blood chemistry analytes included blood urea nitrogen (BUN), phosphate, albumin, globin, gamma glutamyl transpeptidase (GGT), alanine aminotransferase (ALT), aspartate aminotransferase (AST), alkaline phosphatase, total bilirubin, cholesterol, and creatinine

In vivo radiation therapy

Approximately 6 week old female nu/nu nude mice were anesthetized using isoflurane, and HT-1080 cells were injected subcutaneously into the back left flank (2 x 10^6 cells in 0.1 mL of PBS). Tumors were grown until the mean diameter was approximately 7 – 8 mm. Next, tumor-bearing mice were split into four groups of 7 each – the first group received 6 Gy RT only; the second group received an intravenous injection of GPMs (650 mg Au/kg in 0.2 mL) 24 hours prior to a single dose of 6 Gy RT; the third group received GPMs only (*i.e*. no RT), and the fourth group received no GPMs and no RT. When applicable, GPMs were administered by retro-orbital injection. In all groups receiving RT, CT imaging was used to localize the isocenter of the tumor.

Radiation therapy was administered using a SARRP (175 kVp, 15 mA) and delivered through a 17 mm diameter collimator. Mice were monitored for tumor growth, and were sacrificed when the tumor volume reached 1300 mm^3. Tumor volumes were calculated assuming an ellipsoidal tumor shape (1 / 2 x length x $width^2$).[47] Survival time to this endpoint was calculated from date of treatment.

2.4 Results and Discussion

Characterization of 1.9 nm AuNPs

Hydrophobic AuNPs were prepared with dodecanethiol as a capping agent. Transmission electron microscopy (TEM) was used to characterize the mean core size of the individual hydrophobic AuNPs. TEM images showed a uniform distribution of AuNPs with a core size of 1.93 ± 0.16 nm (Figure 2.2). Purity was confirmed *via* UV-vis spectroscopy (Figure 2.3).

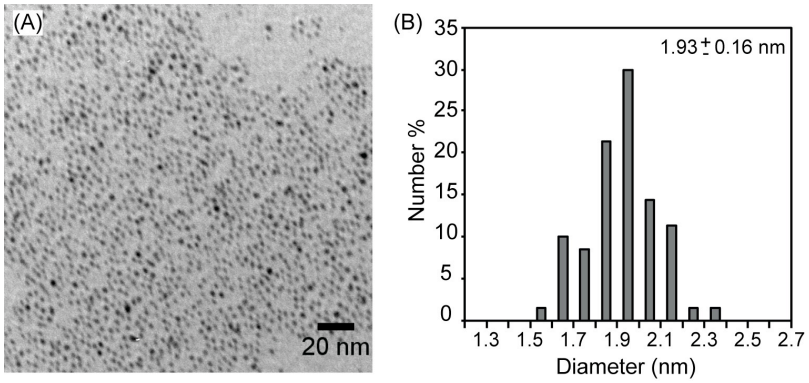

Figure 2.2. (A) Transmission electron micrograph of 1.9 nm AuNPs. Scale bar is 20 nm. **(B)** Core size distribution of 1.9 nm AuNPs. The mean size and standard deviation is shown.

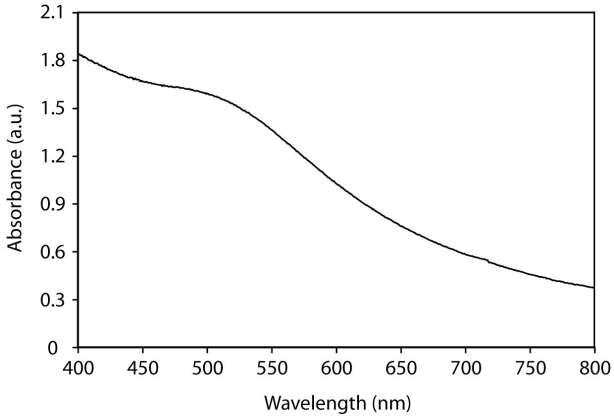

Figure 2.3. UV-vis absorption spectrum of 1.9 nm AuNPs with a broad surface plasmon resonance ranging from 490 nm – 510 nm.

Synthesis and Characterization of GPMs

GPMs were prepared by encapsulating 1.9 nm AuNPs within the diblock copolymer PEG-*b*-PCL, using a microemulsion method. These GPMs were soluble in aqueous solutions owing to the hydrophilic PEG corona of the diblock copolymer. Following synthesis and purification of the GPMs, six different sizes (25 – 150 nm, Figure 2.4) were collected using differential centrifugation, as confirmed by dynamic light scattering (DLS). The DLS measurements demonstrate particle measurements with a low polydispersity index for all GPM fractions (< 0.1). TEM was used to determine the morphology of the GPMs and the packing of AuNPs within the hydrophobic core. TEM micrographs revealed a narrow distribution of spherical GPMs with tightly packed clusters of AuNPs contained within the hydrophobic core of the micelles (Figure 2.4). The TEM micrographs also revealed a low polydispersity, correlating well with the DLS measurements. The zeta potential of the various GPMs formulations was near neutral. A summary of the GPM physical-chemical properties is provided in Table 2.1.

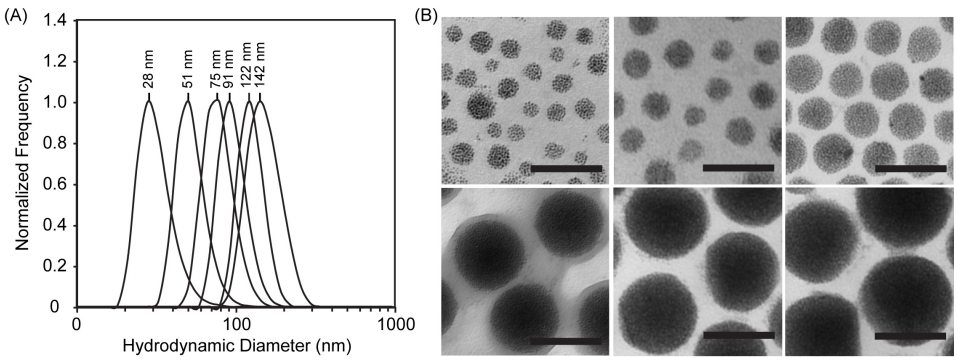

Figure 2.4. Size and morphology of GPMs. **(A)** Dynamic light scattering profiles of six GPM formulations with mean sizes ranging from 25 - 150 nm, in phosphate buffered saline, pH 7.4. **(B)** Transmission electron microscopy (TEM) images of the same six GPM formulations, respectively. The electron micrographs reveal a narrow monodispersed distribution of spherical GPMs, with tightly packed gold clusters contained within the hydrophobic core (all scale bars = 100 nm).

Table 2.1. Summary of GPM physical-chemical properties

Hydrodynamic Diameter (nm)	Core Size (nm)	Polydispersity Index	Zeta potential (mV)
30.9 ± 2.4	26.8 ± 10.4	0.088	-1.34 ± 0.17
57 ± 5.7	39.5 ± 10.3	0.063	-1.01 ± .05
78.6 ± 3.8	54.8 ± 7.1	0.05	-0.95 ± 0.3
97.8 ± 3.4	70.4 ± 16.8	.049	-1.17 ± 0.04
130.2 ± 2.7	106.3 ± 11.5	0.042	-1.5± 0.23
153.8 ± 6.3	115.2 ± 20.3	.055	-1.62 ± 0.85

Evaluation of GPMs as a radiosensitizer

GPMs with a hydrodynamic diameter of approximately 75 nm were selected for a more detailed evaluation as radiosensitizing agents. This size was selected because it was produced in significantly higher yields than the other sizes and was thus more amenable for *in vivo* testing. To evaluate the radiosensitization effects of the 75 nm GPMs *in vitro*, HT-1080 human fibrosarcoma cells were irradiated (4 Gy) or mock irradiated in the presence or absence of GPMs and analyzed for double-stranded breaks (γ-h2ax staining)

(Figure 2.5a-b). Immunofluorescent images revealed very low levels of γ-h2ax foci (observed as bright fluorescent spots) in unirradiated cells, regardless of the presence of GPMs. In contrast, high levels of γ-h2ax foci were observed within the nuclei of cells that received radiation treatment, with a noticeably higher number of double-stranded breaks in cells that were treated in the presence GPMs. Quantitatively, there were very few γ-h2ax foci per unit area in unirradiated controls, as expected, and there was no statistically significant difference between cells incubated in the presence or absence of GPMs. However, when cells were irradiated, the number of γ-h2ax foci increased and a statistically significant difference was observed between cells irradiated in the presence and absence of GPMs. Compared to cells receiving radiation only, the cells that were irradiated in the presence of GPMs exhibited roughly a 2.2 times higher density of DNA double-stranded breaks. Furthermore, clonogenic survival assays revealed a decrease in survival of HT-1080 cells irradiated in the presence of GPMs compared to those receiving irradiation alone (Fig. 2.5c). A statistically significant difference in survival ($p < 0.05$) was observed for radiation doses of 4 and 6 Gy. Using the linear-quadratic model to assess the enhancement of radiation effects, it was estimated that GPMs produced a sensitizer enhancement ratio (SER) of approximately 1.2, which is consistent with previous studies that utilized AuNPs as a radiosensitizer.[22, 29]

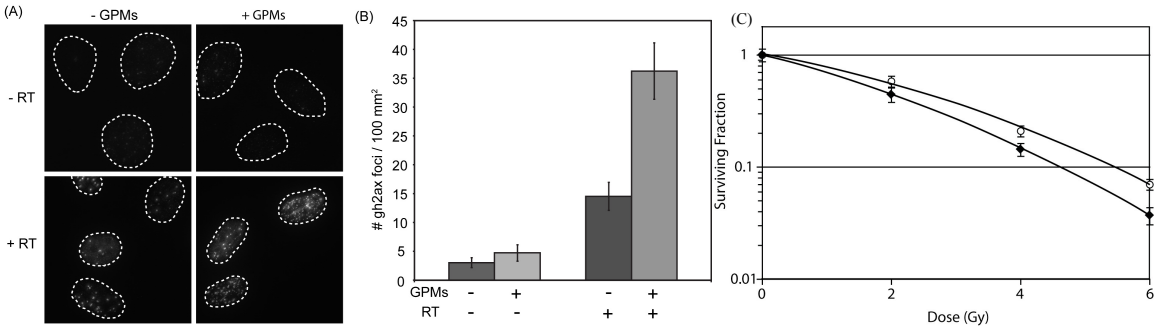

Figure 2.5. *In vitro* evaluation of radiation induced DNA double-stranded breaks in the presence and absence of GPMs. **(A)** Immunofluorescent imaging of γ-h2ax foci in HT-1080 cells incubated with or without GPMs in the absence (top) or presence (bottom) of irradiation (4 Gy). **(B)** Quantitative analysis of γ-h2ax foci density (# foci/um^2) for n > 100 cells in each treatment group. Error bars represent 95% confidence intervals. **(C)** Clonogenic assay of HT-1080 cells treated with and without GPMs and given radiation doses of 0, 2, 4 and 6 Gy. Error bars represent the mean survival ± standard error of at least three replicates.

Stability of GPMs in serum

Prior to evaluating GPMs as an imaging and radiosensitizing agent in living subjects, the stability of 75 nm GPMs was evaluated in fetal bovine serum (Figure 2.6). Upon incubating the GPMs with 100% serum for 24 h at 37°C, there was no difference in the size of the GPMs as determined by DLS and no visible precipitates were observable in the solution. Moreover, no evidence of leaching of AuNPs from the micelle or alteration in the micelle structure was observed on TEM images following incubation in serum (Figure 2.7), suggesting that GPMs are sufficiently stable for *in vivo* studies. It should be noted that all of the micelle samples (i.e. all size fractions) also appear to be stable in PBS at pH 7.4 for months with no observable changes in hydrodynamic diameter or structure, as determined by DLS and TEM, respectively.

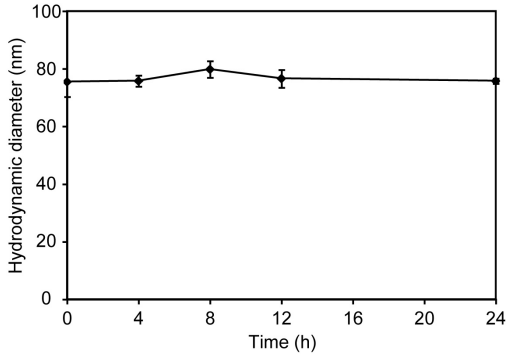

Figure 2.6. Mean hydrodynamic diameter of GPMs in fetal bovine serum as determined by dynamic light

scattering. GPMs were incubated at 37°C and the hydrodynamic diameter was measured over the course of 24 hours.

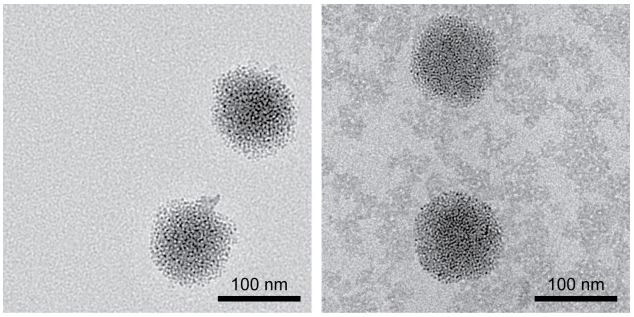

Figure 2.7 Transmission Electron Microscopy image of GPMs in fetal bovine serum prior to (left) and 24 hours after (right) incubation at 37°C.

GPM pharmacokinetics

Long circulating particles, that are able to avoid rapid clearance from the bloodstream *via* glomerular filtration and the reticuloenodthelial system (RES), are necessary for EPR-driven tumor accumulation. Therefore, if GPMs are to be used to help delineate tumor margins and guide radiation therapy, it is necessary for them to exhibit a long circulation half-life. It was determined that the circulation half-life of 75 nm GPMs is ~ 1 hour during the early distribution phase and 8.7 hours during the elimination phase (Figure 2.8). This long circulation time is likely governed by the dense hydrophilic PEG coating present on the micelle.

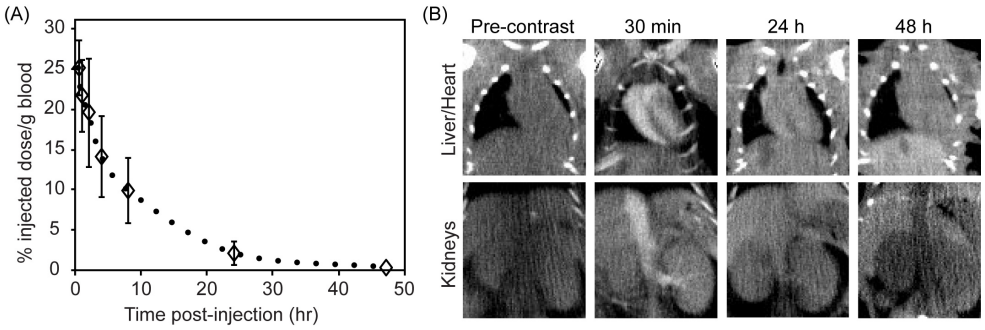

Figure 2.8. Blood clearance profile and CT imaging of GPMs in blood pool. **(A)** ICP-OES analysis of gold content in blood at various times following the intravenous administration of GPMs to mice (n = 3). **(B)** Serial CT coronal views of a mouse following retro-orbital injection of 200 μL of GPMs solution (650 mg Au/kg). Coronal view of heart and liver (top) and inferior vena cava and kidneys (bottom) are shown.

The ability of GPMs to generate contrast *in vivo* was validated in mice. Images acquired 30 minutes post-injection demonstrated enhancement of the great vessels and minor branches such as the renal vessels and interlobular vessels (Figure 2.8). Furthermore, the cardiac chambers were readily visualized demonstrating the potential use of GPMs as a blood-pool contrast agent. After 24 hours there was residual enhancement of the heart and great vessels indicative of the long circulation time of the GPMs. The administered dose of GPMs (650 mg Au/kg) was well within the range of clinically approved intravenous contrast agents. For example, Iodixanol (VISIPAQUE) is typically administered at doses ranging from 300 to 1200 mg I/kg body weight. Additionally, the dose utilized in this study was lower than what was used in prior studies that employed gold as a radiosensitizer (i.e. > 1350 mg Au/kg).[9, 29]

The biodistribution of GPMs was evaluated at 48 hours and at 1 week post-injection by performing an ICP-OES analysis of gold content within the heart, kidneys, lungs, spleen, liver, feces, and urine (Table 2.2). All organs examined showed a marked reduction in gold accumulation between these two time points, including the liver and spleen. Specifically, ICP-OES findings revealed a 28% reduction of gold in the liver and a 47.5% reduction of gold in the spleen. Evaluation of gold content within feces and urine suggests that the primary route of clearance was biliary excretion.

Table 2.2. Biodistribution of GPM in mice at 48 hours and 1 week post-injections displayed as a percentage of injected dose (%ID) and percentage of injected dose per gram of tissue (%ID/g)

Organs	%ID (48 hr)	%ID/g (48 hr)	%ID (1 week)	%ID/g (1 week)
Heart	0.1 ± 0.02	1.1 ± 0.2	0.05 ± 0.004	0.4 ± 0.01
Kidney	0.7 ± 0.1	1.9 ± 0.2	0.4 ± 0.01	1.1 ± 0.1
Lungs	0.4 ± 0.1	2.6 ± 0.7	0.04 ± 0.005	0.3 ± 0.01
Spleen	11.6 ± 0.3	104.3 ± 14.6	6.3 ± 0.6	61.9 ± 5.2
Liver	17.6 ± 1.8	13.9 ± 0.4	12.6 ± 1.0	10.0 ± 0.5
Feces	2.0 ± 0.06	0.6 ± 0.02	0.64 ± 0.04	0.19 ± 0.01
Urine	not determined	0.006 ± 0.001	not determined	0.002 ± 0.000

Toxicity analysis

The intravenous injection of GPMs at 650 mg Au/kg into healthy mice led to no signs of illness, weight loss (Figure 2.9), or change in activity. Notably, the amount of gold administered was well below the LD_{50}, which was previously reported to be 3.2 g Au/kg.[9] A toxicological analysis of mice 1 day and 1 week following the administration of GPMs (650 mg Au/kg) revealed normal blood chemistry, compared to saline injected controls (Table 2.3).

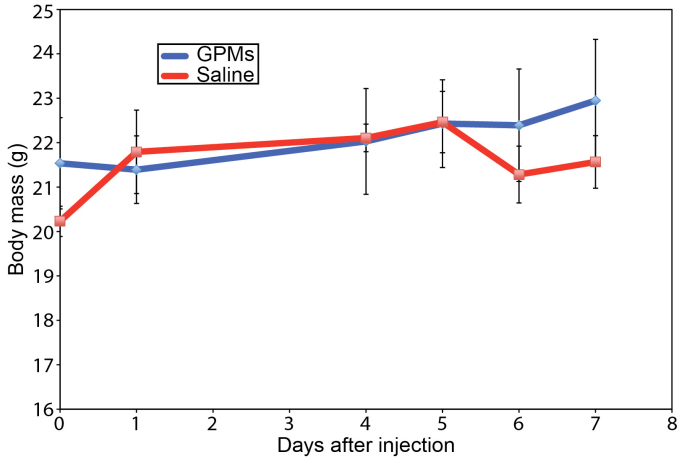

Figure 2.9. Whole animal weights of tumor-free mice treated with 650 mg Au/kg GPMs (0.2 mL) compared with mice sham injected with phosphate buffered saline (0.2 mL). Data reflect average weights and n = 3 for all groups.

Table 2.3. Serum clinical chemistry of mice injected with 650 mg Au/kg GPMs (0.2 mL) and sampled at 24 hours and 1 week compared with mice sham injected with phosphate buffered saline (0.2 mL). All values were within normal limits and n = 3 for all groups. Data is recorded ± standard error.

	BUN	**Albumin**	**ALT**	**AST**	**Alk. Phos.**	**GGT**
Day 1 GPMs	24.3 ± 3.9	2.4 ± 0.1	157.7 ± 111.7	377 ± 146.5	114 ± 7.1	5.3 ± 0.3
Control	25 ± 2.1	2.4 ± 0.1	180 ± 89.3	337 ± 122.1	129.7 ± 11.8	9 ± 1.5
Day 7 GPMs	30.3 ± 3.5	2.4 ± 0.3	93 ± 29.5	245.3 ± 102.9	62.3 ± 2.9	12.7 ± 3.9
Control	20 ± 2.6	2.3 ± 0.2	139 ± 4.4	267.3 ± 78.1	68.7 ± 10.7	23.1 ± 13.3
	Total Bil.	**Cholesterol**	**Calcium**	**Creatinine**	**Glucose**	**Phosphorus**
Day 1 GPMs	0.5 ± 0.2	99.3 ± 9.8	8.9 ± 0.4	0.2 ± 0.0	168.7 ± 24.5	8.5 ± 0.3
Control	1.1 ± 0.0	91.3 ± 2.7	8.6 ± 0.4	0.2 ± 0.0	195.7 ± 34.1	10 ± 0.4
Day 7 GPMs	0.9 ± 0.6	77.3 ± 5	8.8 ± 0.1	0.2 ± 0.1	279.7 ± 10.3	7.7 ± 0.5
Control	1.5 ± 0.9	180 ± 45	9.1 ± 0.6	0.1 ± 0.0	195.7 ± 34.1	8.6 ± 1.6

*BUN, creatinine, total bili (total bilirubin), and cholesterol are in units of mg/dL. ALT, AST, alk. phos. (alkaline phosphatase), and GGT are in units of U/L. Albumin is in units of g/dL. Blood samples were obtained from mice injected with 400 mg Au/kg of GSM or sham injected with saline. Data is recorded ± standard error.

GPMs as a CT contrast agent

The ability of GPMs to accumulate within tumors at sufficient levels to provide CT contrast was confirmed in mice bearing HT-1080 flank tumors. Axial tumor slices of 3 different tumor-bearing mice were analyzed pre-contrast as well as 30 min, 24 h and 48 h post-contrast (Figure 2.10). The variation of signal enhancement from slice to slice was accounted for by normalizing the signal to the corresponding para-spinal muscles for each slice. In the pre-contrast image, the tumor on the flank of the mouse located between the thigh and para-spinal muscles is not clearly delineated. At the 30 minute time point, there is no qualitative or statistical difference in contrast enhancement within the tumor compared to the pre-contrast image. However, at 24 hours and 48 hours post-contrast, the tumor is revealed as a hyper-intense heterogeneously enhancing region with well-defined margins. These enhancements in tumor contrast were statistically different from both the

pre-contrast and 30 minute time points. This result is likely due to the extravasation of GPMs out of leaky vasculature and accumulation within the tumor owing to the EPR effect. This distinction between tumor and normal tissue can help in the design of radiation treatment of cancer by enabling visualization of regional tumor margins and spread, to help localize and maximize radiation doses to malignancies while minimizing exposure to normal tissue. Notably, within the tumor margins, the contrast enhancement was somewhat heterogeneous, likely due to variations in the ability of GPMs to penetrate far beyond the vascular wall.

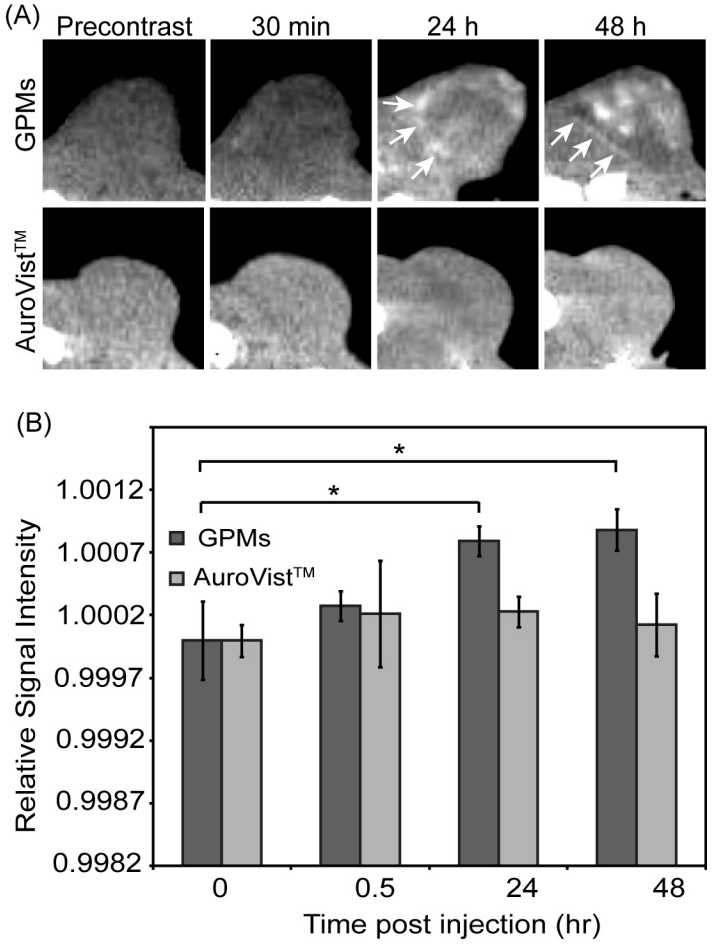

Figure 2.10. *In vivo* CT images and intensity analysis of nu/nu nude mice with HT-1080 flank tumors. **(A)** Representative CT images in the axial plane prior to injection (pre-contrast) and 30 min, 24 h and 48 h post-injection of GPMs (n = 3) or AuroVist™ (n = 3). Tumor boundaries are indicated by white arrows. **(B)**

Quantitative analysis of CT images. Signal intensity of each tumor was normalized to adjacent paraspinal muscle. For contrast measurement, the relative signal intensity, RSI, was calculated as the quotient of the post-contrast to pre-contrast normalized tumor intensity. Statistically significant values of $p < 0.05$ are indicated with an asterisk.

To demonstrate the importance of a long circulating platform for effective extravasation and accumulation in tumors, 1.9 nm control AuNPs were also administered to tumor-bearing mice and imaged 30 min, 24 h and 48 h post-contrast. At each time point, no visible tumor contrast enhancement was observed, compared with pre-contrast images. This is likely because > 90 % of the particles are cleared within the first 30 minutes.[8]

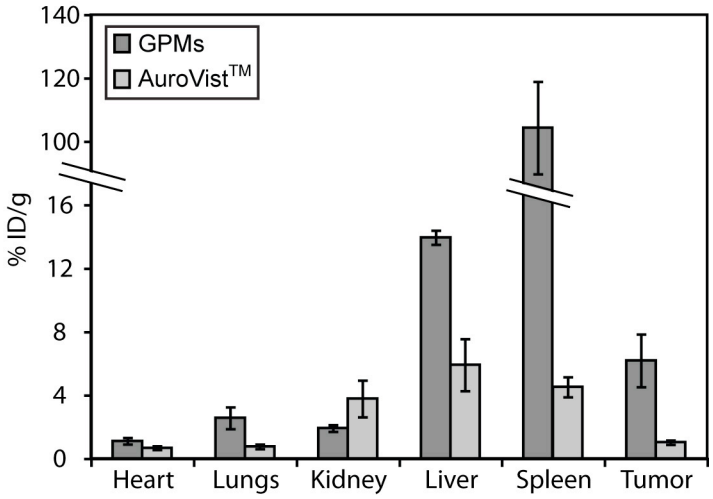

Figure 2.11. ICP-OES analysis of gold distribution at 48 hours following the administration of GPMs or AuroVist™. The percent injected dose per gram of tissue was calculated by measuring the concentration of gold in excised organs *via* ICP-OES. There is a statistically significant increase in the accumulation of gold in tumors of mice receiving GPMs ($p < 0.05$) compared to mice injected with AuroVist™.

To quantitatively determine the amount of GPMs and 1.9 nm AuNPs delivered to the tumor, as well as other organs, the liver, spleen, lung, heart, kidneys, and tumor were harvested 48 hours post-injection and the gold content was analyzed by ICP-OES (Figure

2.11). Mice injected with GPMs had the highest levels of gold in the liver and spleen, and only modest levels of gold in the heart, lungs, and kidneys. In contrast, mice injected with 1.9 nm AuNPs had higher levels of gold within the kidney, lower uptake in the liver and spleen, and very modest uptake in the heart and lungs. This difference in organ distribution is expected since the mechanism of elimination differs for both formulations. In general neutrally charged particles with hydrodynamic sizes smaller than ~ 6 nm are cleared from the systemic circulation *via* glomerular filtration and excreted in the urine,[30] whereas particles greater than ~ 6 nm are primarily cleared by the RES system.[31] This disparity in elimination was also supported by *in vivo* CT imaging. Following GPM administration, the spleen and liver gradually brighten over the course of 48 hours (Figure 2.12); in contrast, mice injected with AuroVist^{TM} exhibit very bright contrast within the kidneys and bladder at early time points of CT imaging and gradually return to baseline at 24 hours post-injection. With respect to tumor delivery, mice injected with GPMs displayed a statistically significant 6-fold increase in gold accumulation compared to mice injected with AuroVist^{TM}. From the ICP-OES data, the average concentration of gold within the tumor was calculated to be 0.57 ± 0.1 mg/mL and 0.14 ± 0.01 mg/mL for mice injected with GPMs and AuroVist^{TM}, respectively. In general, the sensitivity for Au detection using CT imaging is estimated to be around 0.5 mg/mL.[21] However, as a result of the heterogeneous distribution of Au within the tumor, some regions likely have gold concentrations well above this lower detection limit. Furthermore, these tumor concentrations were well above the 0.1 mg Au/mL, where a radiosensitization effect was observed *in vitro*. Importantly, this circulation-mediated increase in nanoparticle delivery was sufficient to provide CT contrast prior to tumor radiation therapy. This demonstrates

the importance of having a long circulating platform since the improvement in delivery has the ability to yield significant contrast enhancement for CT-guided radiation therapy.

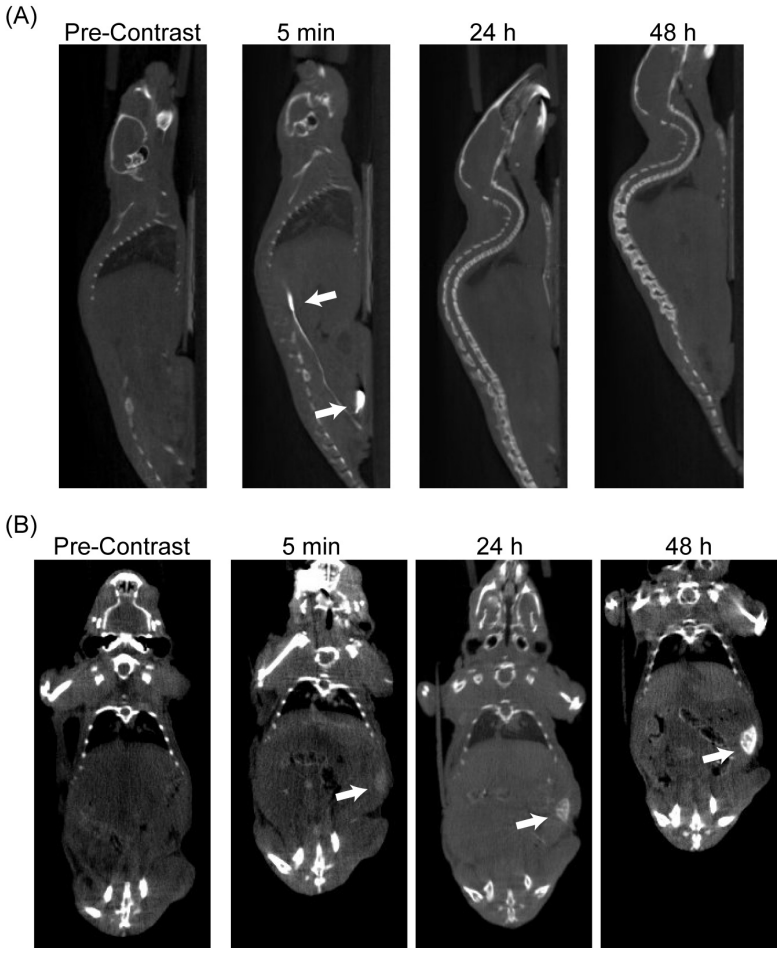

Figure 2.12. Computed tomography images of mice injected with AuroVist^{TM} or GPMs. **(A)** The kidneys, ureter and bladder (arrows) are enhanced during early imaging time points following the injection of AuroVist^{TM}, but no contrast is evident at 24 h or 48 h, consistent with renal clearance. **(B)** The spleen (arrows) is observed as early as 5 minutes post-injection of GPMs and contrast continues to increase over the next 48 h, indicative of RES uptake.

Radiosensitization of tumors with GPMs

To specifically examine the therapeutic effects of using GPMs as radiosensitzers *in vivo*, nu/nu mice bearing 7 - 8 mm subcutaneous HT-1080 flank tumors were divided

into four groups (n = 7 per group). The first two groups were the unirradiated controls with one of the two groups receiving GPMs. The next two groups received either radiation therapy (6 Gy) alone or were injected with GPMs 24 hours prior to radiation treatment. Notably, contrast enhancement was visible within the tumors of mice receiving GPMs, which enabled CT-guided stereotactic radiation. Mice were monitored for tumor growth and were sacrificed when the tumors reached the predetermined threshold volume (1300 mm^3). The survival time was measured from the time of radiation (or mock irradiation). Mice that received GPMs prior to radiation therapy exhibited a statistically significant ($p < 0.05$) improvement in median survival (68 days), compared to mice treated with radiation alone (38 days) (Figure 2.13). It should be noted that all mouse groups appeared to tolerate GPMs very well over the course of study with no observable changes in behavior or symptoms of poisoning such as loss of appetite, diarrhea, or vomiting. For the group receiving radiation only, two mice were sacrificed prior to the threshold volume cutoff due to an ulcerated tumor in one and severe emaciation in another. The general observable trend in tumor growth post radiation therapy was a reduction in tumor growth, followed by a reduction in tumor volume and then eventual tumor re-growth (Figure 2.14). Only one mouse out of seven in the radiation-only group, with a slow growing palpable tumor, survived 90 days post treatment. In contrast, 3 of the 7 mice that received GPMs prior to radiation survived 90 days post therapy. Two out of the three mice had complete remission with no palpable tumor while the third mouse had a palpable static tumor. With respect to the unirradiated groups, GPMs alone had no effect on tumor growth compared to untreated controls. These results suggest that the

EPR-dependent accumulation of GPMs within tumors can guide and enhance the efficacy of radiation therapy.

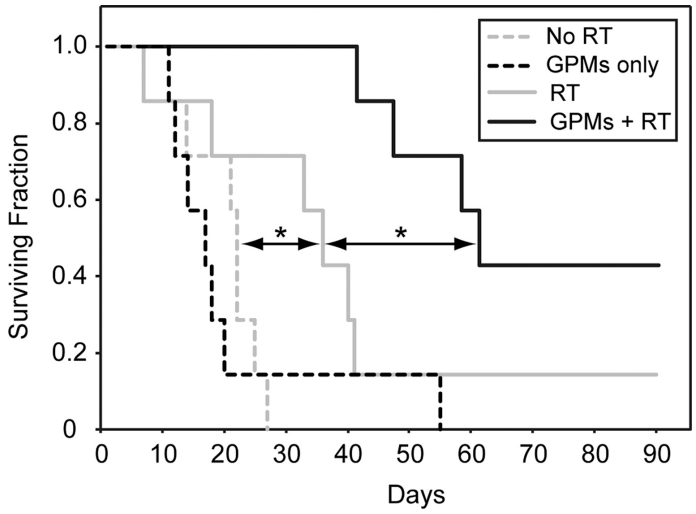

Figure 2.13. Kaplan-Meier survival analysis. A survival analysis was performed for tumor bearing mice (n = 7 per group) receiving no treatment (dotted grey line), GPMs only (dotted black line), irradiation only (solid grey line), or irradiation 24 h after retro-orbital injection of GPMs (solid black line). GPMs were administered at a dose of 650 mg Au/kg. The radiation dose administered was 6 Gy at 150 kVp. The asterisk indicates statistical significance ($p < 0.05$).

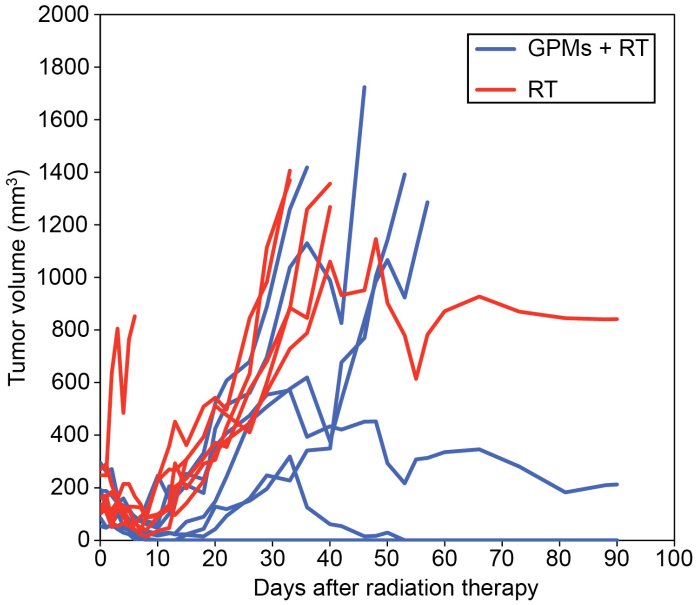

Figure 2.14. Tumor growth curves of mice receiving GPMs with radiation therapy (blue) or radiation therapy alone (red).

2.5 Conclusion

Gold nanoparticles present a promising platform for therapeutic and imaging (theranostic) applications because of their unique physical-chemical properties, their ability to be easily functionalized and their safety profile. Gold has been used in medical practice throughout history and continues today as a treatment for rheumatoid arthritis.[32] Numerous animal studies suggest that AuNPs are also very well tolerated.[33-38] In fact, several AuNP formulations have even entered clinical trials for cancer treatment, including CYT-6091 and AuroShell®. In this study 1.9 nm AuNPs were encapsulated within the biocompatible and biodegradable polymer PEG-*b*-PCL, forming gold-loaded polymeric micelles. An anticipated benefit of this GPM formulation over pegylated, solid AuNPs of similar size is that it is easy to incorporate other anticancer and/or other metallic nanoparticles into the micelle core,[39-41] if additional functionality is desirable. Moreover, we believe that the presence of many small AuNPs (1.9 nm) may allow for more rapid dissolution and excretion, compared with a single large AuNP. It was previously reported that with 40 nm solid AuNPs there is only a 9% fall in the content of gold in the liver from day 1 to 6 months.[42] In addition, many studies report inefficient clearance and a persistent accumulation of AuNPs within the reticuloendothelial system.[43-45] In contrast, we observed more than a 28% fall in gold content within the liver between day 2 and day 7. These results are very promising, although a more complete analysis must still be performed to study additional and later time points before a

definitive conclusion can be drawn.

In summary, we showed that GPMs were capable of enhancing radiation-induced DNA double-stranded breaks in a cell culture model, consistent with prior work with solid AuNPs.[14, 15, 20-25, 29] Furthermore, because of their extended clearance half-life, GPMs exhibited improved EPR-dependent accumulation in murine tumor xenografts, compared to individual 1.9 nm AuroVist^{TM} nanoparticles. The higher levels of GPM accumulation in the tumor provided clear and quantifiable improvement in CT contrast. The combination of CT-guided radiation therapy and gold-mediated radiosensitization led to a statistically significant increase in the mean survival time of tumor-bearing mice compared with mice receiving radiation alone. Accurate delineation of tumor extent and tumor-specific radiosensitization is important for radiotherapy, due to radiation dose limitations of the surrounding normal tissue. Therefore, we envision that GPMs can be used someday in a tractable manner to both guide and enhance the efficacy of radiation therapy.

2.7 References

1. Benita, S.; Poly, P. A.; Puisieux, F.; Delattre, J., Radiopaque Liposomes: Effect of Formulation Conditions on Encapsulation Efficiency. *J. Pharm. Sci.* **1984,** 73, 1751-1755.

2. Elrod, D. B.; Partha, R.; Danila, D.; Casscells, S. W.; Conyers, J. L., An Iodinated Liposomal Computed Tomographic Contrast Agent Prepared From a Diiodophosphatidylcholine Lipid. *Nanomedicine* **2009,** 5, 42-45.

3. A, S., Iodinated liposomes as contrast agents. In: Ferrari M, Bulte JWM, Modo MMJ, editors. Fundamental Biomedical Technologies: Nanoparticles in biomedical imaging. New York: Springer. **2008**, 371-410.

4. Torchilin, V. P.; Frank-Kamenetsky, M. D.; Wolf, G. L., CT Visualization of Blood Pool in Rats by Using Long-Circulating, Iodine-Containing Micelles. *Acad. Radiol.* **1999,** 6, 61-65.

5. Long, D. M., Jr.; Lasser, E. C.; Sharts, C. M.; Multer, F. K.; Nielsen, M., Experiments With Radiopaque Perfluorocarbon Emulsions for Selective Opacification of Organs and Total Body Angiography. *Invest. Radiol.* **1980,** 15, 242-247.

6. Patronas, N. J.; Hekmatpanah, J.; Doi, K., Brain-Tumor Imaging Using Radiopaque Perfluorocarbon - a Preliminary-Report. *J. Neurosurg.* **1983,** 58, 650-653.

7. Rabin, O.; Perez, J. M.; Grimm, J.; Wojtkiewicz, G.; Weissleder, R., An X-ray Computed Tomography Imaging Agent Based on Long-Circulating Bismuth Sulphide Nanoparticles. *Nat. Mater.* **2006,** 5, 118-122.

8. Hainfeld, J. F.; Slatkin, D. N.; Focella, T. M.; Smilowitz, H. M., Gold Nanoparticles: a New X-ray Contrast Agent. *Br. J. Radiol.* **2006,** 79, 248-253.

9. Hainfeld, J. F.; Slatkin, D. N.; Smilowitz, H. M., The Use of Gold Nanoparticles to Enhance Radiotherapy in Mice. *Phys. Med. Biol.* **2004,** 49, 309-315.

10. Kim, D.; Park, S.; Lee, J. H.; Jeong, Y. Y.; Jon, S., Antibiofouling Polymer-Coated Gold Nanoparticles as a Contrast Agent for In Vivo X-ray Computed Tomography Imaging. *J. Am. Chem. Soc.* **2007,** 129, 7661-7665.

11. Jackson, P. A.; Abd Rahman, W. N. W.; Wong, C. J.; Ackerly, T.; Geso, M., Potential Dependent Superiority of Gold Nanoparticles in Comparison to Iodinated Contrast Agents. *Eur. J. Radiol.* **2010,** 75, 104-109.

12. Rabin, O.; Perez, J. M.; Grimm, J.; Wojtkiewicz, G.; Weissleder, R., An X-ray computed tomography imaging agent based on long-circulating bismuth sulphide nanoparticles. *Nature Materials* **2006,** 5, (2), 118-122.

13. Peng, C.; Zheng, L.; Chen, Q.; Shen, M.; Guo, R.; Wang, H.; Cao, X.; Zhang, G.; Shi, X., PEGylated Dendrimer-Entrapped Gold Nanoparticles for In Vivo Blood Pool and Tumor Imaging by Computed Tomography. *Biomaterials* **2012,** 33, 1107-1119.

14. Butterworth, K. T.; Coulter, J. A.; Jain, S.; Forker, J.; McMahon, S. J.; Schettino, G.; Prise, K. M.; Currell, F. J.; Hirst, D. G., Evaluation of Cytotoxicity and Radiation Enhancement Using 1.9 nm Gold Particles: Potential Application for Cancer Therapy. *Nanotechnol.* **2010,** 21.

15. Cheng, N. N.; Starkewolf, Z.; Davidson, R. A.; Sharmah, A.; Lee, C.; Lien, J.; Guo, T., Chemical Enhancement by Nanomaterials Under X-ray Irradiation. *J. Am. Chem. Soc.* **2012,** 134, 1950-1953.

16. Coulter, J. A.; Hyland, W. B.; Nicol, J.; Currell, F. J., Radiosensitising nanoparticles as novel cancer therapeutics--pipe dream or realistic prospect? *Clin. Oncol.* **2013,** 25, 593.

17. Dorsey, J. F.; Sun, L.; Joh, D. Y.; Witztum, A.; Al Zaki, A.; Kao, G. D.; Alonso-Basanta, M.; Avery, S.; Tsourkas, A.; Hahn, S. M., Gold nanoparticles in radiation research: potential applications for imaging and radiosensitization. *Transl Cancer Res* **2013,** 2, (4), 280-291.

18. Douglass, M.; Bezak, E.; Penfold, S., Monte Carlo investigation of the increased radiation deposition due to gold nanoparticles using kilovoltage and megavoltage photons in a 3D randomized cell model. *Med. Phys.* **2013,** 40, 071710.

19. Lechtman, E.; Mashouf, S.; Chattopadhyay, N.; Keller, B. M.; Lai, P.; Cai, Z.; Reilly, R. M.; Pignol, J. P., A Monte Carlo-based Model of Gold Nanoparticle Radiosensitization Accounting for Increased Radiobiological Effectiveness. *Phys. Med. Biol.* **2013,** 58, 3075.

20. Chithrani, D. B.; Jelveh, S.; Jalali, F.; van Prooijen, M.; Allen, C.; Bristow, R. G.; Hill, R. P.; Jaffray, D. A., Gold Nanoparticles as Radiation Sensitizers in Cancer Therapy. *Radiat. Res.* **2010,** 173, 719-728.

21. Hainfeld, J. F.; Dilmanian, F. A.; Zhong, Z.; Slatkin, D. N.; Kalef-Ezra, J. A.; Smilowitz, H. M., Gold Nanoparticles Enhance the Radiation Therapy of a Murine Squamous Cell Carcinoma. *Phys. Med. Biol.* **2010,** 55, 3045-59.

22. Jain, S.; Coulter, J. A.; Hounsell, A. R.; Butterworth, K. T.; McMahon, S. J.; Hyland, W. B.; Muir, M. F.; Dickson, G. R.; Prise, K. M.; Currell, F. J.; O'Sullivan, J.

M.; Hirst, D. G., Cell-Specific Radiosensitization by Gold Nanoparticles at Megavoltage Radiation Energies. *Int. J. Radiat. Oncol., Biol., Phys.* **2011,** 79, 531-539.

23. Liu, C. J.; Wang, C. H.; Chen, S. T.; Chen, H. H.; Leng, W. H.; Chien, C. C.; Wang, C. L.; Kempson, I. M.; Hwu, Y.; Lai, T. C.; Hsiao, M.; Yang, C. S.; Chen, Y. J.; Margaritondo, G., Enhancement of Cell Radiation Sensitivity by Pegylated Gold Nanoparticles. *Phys. Med. Biol.* **2010,** 55, 931-945.

24. Zhang, X. D.; Wu, D.; Shen, X.; Chen, J.; Sun, Y. M.; Liu, P. X.; Liang, X. J., Size-Dependent Radiosensitization of PEG-Coated Gold Nanoparticles for Cancer Radiation Therapy. *Biomaterials* **2012,** 33, 6408-6419.

25. Zheng, Y.; Hunting, D. J.; Ayotte, P.; Sanche, L., Radiosensitization of DNA by Gold Nanoparticles Irradiated with High-Energy Electrons. *Radiat. Res.* **2008,** 169, 19-27

26. Stone, H. B.; Coleman, C. N.; Anscher, M. S.; McBride, W. H., Effects of radiation on normal tissue: consequences and mechanisms. *Lancet Oncol* **2003,** 4, (9), 529-36.

27. Engelmeier, R. L.; King, G. E., Complications of Head and Neck Radiation Therapy and Their Management. *J. Prosthet. Dent.* **1983,** 49, 514-522.

28. Bernier, J.; Hall, E. J.; Giaccia, A., Radiation Oncology: a Century of Achievements. *Nat. Rev. Can.* **2004,** 4, 737-747.

29. Joh, D. Y.; Sun, L.; Stangl, M.; Al Zaki, A.; Murty, S.; Santoiemma, P. P.; Davis, J. J.; Baumann, B. C.; Alonso-Basanta, M.; Bhang, D.; Kao, G. D.; Tsourkas, A.; Dorsey, J. F., Selective Targeting of Brain Tumors with Gold Nanoparticle-Induced Radiosensitization. *PLoS One* **2013,** 8, e62425.

30. Longmire, M.; Choyke, P. L.; Kobayashi, H., Clearance properties of nano-sized particles and molecules as imaging agents: considerations and caveats. *Nanomedicine (Lond)* **2008,** 3, (5), 703-17.

31. Choi, H. S.; Liu, W.; Misra, P.; Tanaka, E.; Zimmer, J. P.; Itty Ipe, B.; Bawendi, M. G.; Frangioni, J. V., Renal Clearance of Quantum Dots. *Nat. Biotechnol.* **2007,** 25, 1165-1170.

32. SP., F., Medical Uses of Gold Compounds: Past, Present, and Future. *Gold Bull.* **1996,** 29, 53 - 60.

33. Connor, E. E.; Mwamuka, J.; Gole, A.; Murphy, C. J.; Wyatt, M. D., Gold Nanoparticles are Taken up by Human Cells but do not Cause Acute Cytotoxicity. *Small* **2005,** 1, 325-327.

34. Lasagna-Reeves, C.; Gonzalez-Romero, D.; Barria, M. A.; Olmedo, I.; Clos, A.; Ramanujam, V. M. S.; Urayama, A.; Vergara, L.; Kogan, M. J.; Soto, C., Bioaccumulation and Toxicity of Gold Nanoparticles after Repeated Administration in Mice. *Biochem. Biophys. Res. Commun.* **2010,** 393, 649-655.

35. Lewinski, N.; Colvin, V.; Drezek, R., Cytotoxicity of nanoparticles. *Small* **2008,** 4, (1), 26-49.

36. Pan, Y.; Neuss, S.; Leifert, A.; Fischler, M.; Wen, F.; Simon, U.; Schmid, G.; Brandau, W.; Jahnen-Dechent, W., Size-Dependent Cytotoxicity of Gold Nanoparticles. *Small* **2007,** 3, 1941-1949.

37. Shukla, R.; Bansal, V.; Chaudhary, M.; Basu, A.; Bhonde, R. R.; Sastry, M., Biocompatibility of Gold Nanoparticles and Their Endocytotic Fate Inside the Cellular Compartment: A Microscopic Overview. *Langmuir* **2005,** 21, 10644-10654.

38. Tkachenko, A. G.; Xie, H.; Coleman, D.; Glomm, W.; Ryan, J.; Anderson, M. F.; Franzen, S.; Feldheim, D. L., Multifunctional Gold Nanoparticle-Peptide Complexes for Nuclear Targeting. *J. Am. Chem. Soc.* **2003,** 125, 4700-4701.

39. Torchilin, V. P., PEG-Based Micelles as Carriers of Contrast Agents for Different Imaging Modalities. *Adv. Drug Deliv. Rev.* **2002,** 54, 235-252.

40. Ai, H.; Flask, C.; Weinberg, B.; Shuai, X.; Pagel, M. D.; Farrell, D.; Duerk, J.; Gao, J. M., Magnetite-Loaded Polymeric Micelles as Ultrasensitive Magnetic-Resonance Probes. *Adv. Mater.* **2005,** 17, 1949-+.

41. Nasongkla, N.; Bey, E.; Ren, J.; Ai, H.; Khemtong, C.; Guthi, J. S.; Chin, S. F.; Sherry, A. D.; Boothman, D. A.; Gao, J., Multifunctional Polymeric Micelles as Cancer-Targeted, MRI-Ultrasensitive Drug Delivery Systems. *Nano Lett.* **2006,** 6, 2427-2430.

42. Sadauskas, E.; Danscher, G.; Stoltenberg, M.; Vogel, U.; Larsen, A.; Wallin, H., Protracted Elimination of Gold Nanoparticles From Mouse Liver. *Nanomedicine* **2009,** 5, 162.

43. Balasubramanian, S. K.; Jittiwat, J.; Manikandan, J.; Ong, C. N.; Yu, L. E.; Ong, W. Y., Biodistribution of gold nanoparticles and gene expression changes in the liver and spleen after intravenous administration in rats. *Biomaterials* 31, (8), 2034-42 (2010).

44. Cho, W. S.; Cho, M.; Jeong, J.; Choi, M.; Cho, H. Y.; Han, B. S.; Kim, S. H.; Kim, H. O.; Lim, Y. T.; Chung, B. H., Acute toxicity and pharmacokinetics of 13 nm-sized PEG-coated gold nanoparticles. *Toxicol Appl Pharmacol* **2009,** 236, (1), 16-24.

45. Niidome, T.; Yamagata, M.; Okamoto, Y.; Akiyama, Y.; Takahashi, H.; Kawano, T.; Katayama, Y.; Niidome, Y., PEG-modified gold nanorods with a stealth character for in vivo applications. *J Control Release* **2006,** 114, (3), 343-7.

46. Brust, M.; Walker, M.; Bethell, D.; Schiffrin, D. J.; Whyman, R., Synthesis of Thiol-Derivatized Gold Nanoparticles in a 2-phase Liquid-Liquid System. *J. Chem. Soc. Chem. Commun.* **1994**, 801-802 .

47. Tomayko, M. M.; Reynolds, C. P., Determination of Subcutaneous Tumor Size in Athymic (nude) Mice. *Cancer Chemother. and Pharmacol.* **1989,** 24, 148-154.

Chapter 3: Development of a Multi-Functional Nanoplatform for Imaging, Radiotherapy, and the Prediction of Therapeutic Response

3.1 Abstract

Gold nanoparticles have garnered interest as both radiosensitzers and computed tomography (CT) contrast agents. However, the extremely high concentrations of gold nanoparticles required to generate CT contrast is far beyond that needed for meaningful radiosensitization, which limits their use as combined therapeutic-diagnostic – theranostic – agents. To establish a theranostic nanoplatform with well-aligned radiotherapeutic and diagnostic properties for better integration into standard radiation therapy practice, we developed a gold- and superparamagnetic iron oxide nanoparticle (SPION)-loaded micelle (GSM). Intravenous injection of GSMs into tumor-bearing mice led to selective, tumoral accumulation, enabling magnetic resonance (MR) imaging of tumor margins. Subsequent irradiation led to a 90-day survival of 71% in GSM-treated mice, compared with 29% for irradiation-only mice. Furthermore, measurements of the GSM-enhanced MR contrast were highly predictive of tumor response. Therefore, GSMs may not only guide and enhance the efficacy of radiation therapy, but may allow patients to be managed more effectively.

3.2 Introduction

External beam radiation therapy is an integral part of current treatment strategies for a variety of cancer types, both for initial therapy and recurrence. Increasingly, more targeted approaches using stereotactic radiosurgery are also being used to maximize the dose to the tumor volume while limiting off-target side effects. Moreover, a wide range of radiosensitizers, including existing chemotherapeutic agents, are being explored to specifically enhance ionizing radiation within tumor tissue without going above the relative dose limitations of surrounding normal tissue.[1,2] Some of the most promising nanotechnology candidates being evaluated as radiosensitizers utilize high-Z materials (i.e. high atomic number), such as gold nanoparticles (AuNPs), to significantly enhance the dose of radiation therapy.[3-7] AuNP-mediated radiosensitization is due to the greater absorption and deposition of energy in surrounding tissues from photoelectrons, Auger electrons, and characteristic X-rays.[8-9] [10-14] It has been shown that the administration of AuNPs can lead to a statistically significant increase in median survival in tumor-bearing mice compared with radiation therapy alone.[15-18]

Accurate dosimetry planning prior to radiation treatment requires radiation oncologists and radiation physicists to consider a number of critical factors including the mapping of tumor margins, which can often be difficult to assess using current imaging techniques. AuNPs have long been exploited as computed tomography (CT)-contrast agents and recently have been used to assist with the delineation of tumors boundaries to guide external beam irradiation, thereby simultaneously serving as both a therapeutic and imaging agent.[8,19] The results from these studies have been encouraging, with tumor-bearing mice exhibiting enhanced tumor contrast and improved median survival when

treated with AuNPs in combination with radiation therapy, compared with radiation therapy alone.[17,18] However, a debilitating limitation of this approach is the considerable mismatch between the lower detection limit of gold on CT systems (mM concentration range) and the tumoral concentration required for gold-mediated radiosensitization (μM range). This disparity therefore would require the administration of supratherapeutic doses – on the order of grams Au/kg body weight[8] – to perform imaging studies prior to initiating radiotherapy treatment.

Magnetic resonance (MR) imaging is an integral component of the workup for many tumors and increasingly utilized for treatment planning. Consequently, nanoplatforms that include MR contrast agents could be organically integrated into standard radiation therapy practice. Superparamagnetic iron oxide nanoparticles (SPIONs) are a popular class of MR contrast agent that generate contrast by rapidly de-phasing the magnetic moments of proximal water molecules.[20] SPIONs are capable of generating T_2-weighted contrast enhancement in MR imaging at nanomolar concentrations and can therefore be detected by MR at concentrations far lower than those at which AuNPs can be detected via CT.[20]

Herein, we report the design and testing of a multifunctional nanoplatoform consisting of **G**old- and **S**PIO-nanoparticle loaded polymeric **M**icelles ("GSMs") with well aligned radiotherapeutic and diagnostic ("RadioTheranostic") properties. The AuNPs and SPIONs were encapsulated within the hydrophobic core of micelles formed with the biodegradable, amphiphilic diblock copolymer poly(ethylene glycol)-*b*-poly(ε-caprolactone) (Figure 3.1a). The physical-chemical properties of GSMs and their contrast- and radio-enhancement characteristics were first evaluated *in vitro*. A focused

pharmacokinetic and toxicity analysis was subsequently performed in healthy mice. GSMs were then translated into a murine tumor xenograft model in order to assess their *in vivo* imaging, therapeutic, and prognostic benefits.

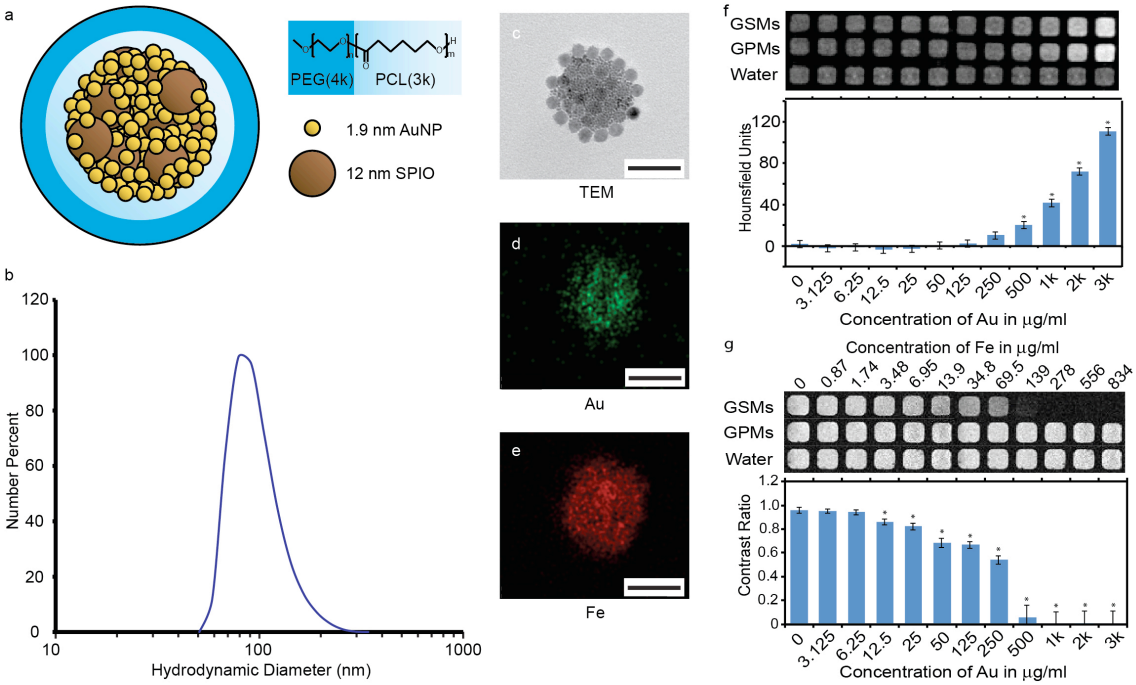

Figure 3.1. (A) Schematic of gold- and SPIO-nanoparticle loaded polymeric micelles (GSMs). Gold and SPIO nanoparticles are self-assembled into the hydrophobic core of micelles, stabilized with the amphiphilic diblock copolymer PEG-*b*-PCL. Each GSM is composed of approximately hundreds to thousands of individual gold nanoparticles and tens to hundreds of SPIO nanoparticles. **(B)** Dynamic light scattering profile of GSMs in phosphate buffered saline, pH 7.4. The average hydrodynamic diameter is 100 nm. **(C)** Transmission electron microscopy (TEM) image of a single GSM. The electron micrograph reveals the incorporation of two size populations of nanoparticles (gold, 1.9 nm; SPIO, 12 nm) tightly packed within the hydrophobic core (all scale bars = 100 nm). **(D-E)** Energy dispersive X-ray spectroscopy analysis on GSM with Au and Fe signals respectively. **(F)** CT phantoms of GSMs and gold-loaded polymeric micelles (GPMs) with a sensitivity detection limit around 500 μg Au/mL. **(G)** MR phantoms of GSMs and GPMs (sensitivity detection limit 12.5 μg Au/mL (3.48 μg Fe/mL).

3.3 Materials and Methods

Materials

Laboratory stock chemicals, as well as iron and gold salts, were purchased from Sigma-Aldrich (St. Louis, MO, USA). Cell culture materials (medium, serum, trypsin, and antibiotics) were purchased from Invitrogen (Carlsbad, CA, USA). Other materials were ordered as specified.

Synthesis of hydrophobic 1.9 nm gold nanoparticles

Dodecanethiol-capped gold nanoparticles, 1.9 nm in diameter, were prepared by the reduction of gold salts in a two-phase reaction, as previously described by Brust et al. [46] Briefly, a 30 mM solution of $HAuCl_4$ (30 mL) was mixed with 80 mL of a 50 mM solution of tetraoctylammonium bromide in toluene, with the addition of 170 mg (84 mmol) of 1-dodecanethiol. While this two-phase solution was stirring vigorously, a 25 mL aqueous solution of 400 mM $NaBH_4$ was added dropwise at a rate of 1 mL per minute. The resulting mixture was then allowed to stir for three hours. Next, the aqueous phase was removed from the organic phase, which contained the AuNPs. The organic solution was then diluted with three volumes of 95% ethanol, and the mixture was precipitated overnight at -20°C. The resulting precipitate was then collected via centrifugation and the supernatant removed. Finally, the gold nanoparticles were resuspended in toluene to a final concentration of ~ 40 mg/mL.

Synthesis of hydrophobic 12 nm SPIO nanoparticles

Oleic acid stabilized SPIO particles were prepared by thermal decomposition as previously described by Park et al.[47] After allowing the reaction to cool to room

temperature, two volumes of acetone were added and the resulting mixture was centrifuged to precipitate the nanoparticles. The particles were then washed in 10 mL hexane and precipitated again using 35 mL of acetone followed by centrifugation. This washing procedure was repeated until the supernatant was clear. The particles were then allowed to air dry and dissolved in toluene at ~ 40 mg/mL.

Synthesis of gold-superparamagnetic iron oxide polymeric micelles (GSMs)

GSMs were prepared using an oil-in-water emulsion-based self-assembly method. First, polyethylene glycol (4k) – polycaprolactone (3k) (PEG-*b*-PCL) was dissolved in toluene to a concentration of 50 mg/mL. A solution (205 μL) containing AuNPs (4 mg), SPIO (1 mg), and PEG-*b*-PCL (4 mg) was then injected into a glass vial containing 4 mL of dH_2O and the sample was sonicated (Branson Ultrasonics, Danbury, CT, USA) until a homogenous mixture was obtained. The toluene was then left uncapped and allowed to evaporate overnight. For large scale preparation, this synthesis was easily scaled up by a factor of 10 using a sonic dismembrator (Fisher Scientific, Waltham, MA, USA).

Purification of size-specific GSMs

GSM samples were first centrifuged at 1,000 RCF for 30 minutes to remove large aggregates. The resulting supernatant then underwent diafiltration using a MidGee hoop cross flow cartridge with 750 kDa molecular weight cutoff (GE Healthcare, Piscataway, NJ, USA) in order to remove small impurities and exchange the solution into PBS. GSMs were then passed through a 0.22 μm SFCA filter (Millipore, Billercia, MA, USA) to remove oversized particles. Finally, this filtered solution was centrifuged at 31,000 RCF for one hour, and the pellet was resuspended in PBS. Micelles were then concentrated as

needed using 50 kDa MWCO centrifugal filter units (Millipore, Billercia, MA, USA) and exchanged into cell culture media as necessary.

The concentrations of gold and iron in a given micelle sample were measured by Genesis ICP-OES (Spectro Analytical Instruments GMBH; Kleve, Germany) at the Department of Earth and Environmental Sciences, University of Pennsylvania, PA, USA. Analytical standards were purchased from RICCA Chemical Company (Arlington, TX, USA), and nitric acid and hydrochloric acid were purchased from Fisher Scientific. All dilutions were done using deionized water (≥ 18 MΩ-cm) obtained from a Millipore water purification system.

Metal nanoparticle and GSM physicochemical characterization

AuNP and SPIO size distributions were verified by TEM. Stock samples were diluted in dH_2O and deposited on 200-mesh carbon coated copper grids (Polysciences, Warrington, PA, USA) for TEM imaging with a JEOL 1010 transmission electron microscope. Mean particle diameters and standard deviations were assessed by measuring the diameters of 50 individual particles in ImageJ. GSM size distributions and zeta potentials were measured in pH 7.4 phosphate buffered saline (PBS) by dynamic light scattering using a Zetasizer Nano-ZS (Malvern Instruments, Worcestershire, UK). GSMs were also imaged by TEM, using the same method used for individual metal nanoparticles. GSM relaxivities (r_1 and r_2) were measured using a Bruker mq60 tabletop MR relaxometer (1.41 T, 60 MHz). The gold and iron content of the GSMs was assessed using both a Genesis ICP-OES and energy dispersive X-ray spectroscopy (EDS) mapping using a JEOL 2010F transmission electron microscope.

Determination of contrast sensitivity limit

The radiologic sensitivity was determined for both CT and MRI imaging modalities using 100 nm GSMs. A 384-well plate (well volume of 100 uL) was prepared using GSMs (100 nm diameter) in dH2O with concentrations ranging from 0 to 3,000 μg Au/mL. The same setup was duplicated in parallel on the same plate using 100 nm Au-only micelles (GPMs) as a nanoparticle control. A row of pure dH_2O was included between the rows of GSMs and GPMs as a no-particle control. The CT image was taken at 55 kVp, 5 mAs using the Small Animal Radiation Research Platform (SARRP) at the Perelman School of Medicine of the University of Pennsylvania. The MR image was taken with a 9.0 T magnet at the Small Animal Imaging Facility of the University of Pennsylvania using a gradient echo multislice (GEMS) sequence, TR = 200 ms, and TE = 5 ms. Images were analyzed using ImageJ software. For the CT phantom, Hounsfield units were computed for each well based upon a linear transformation setting $HU_{air} = -1000$ and $HU_{dH2O} = 0$. In order to reduce image noise, the final CT phantom image was constructed by averaging together all of the image slices containing a full view of all pertinent wells from five separate CT scans of the phantom. For the MRI image, the contrast ratio (CR) was computed as the ratio of the average well intensity for micelle and water containing wells, respectively. Statistical analysis ($\alpha = 0.05$) was then performed to determine the lowest concentrations at which the GSMs gave a contrast signal significantly different from baseline (i.e. CR = 1 or HU = 0) in each modality. A similar analysis was performed for the Au-only micelles.

Cell culture and tumor model

HT-1080 mammalian fibrosarcoma cells were cultured and maintained at 37°C and 5% CO_2 in minimum essential media (MEM), supplemented with 10% fetal bovine serum (FBS) and 1% penicillin / streptomycin. Six-week old female nu/nu nude mice (Charles River Laboratory, Charles River, MA, USA) were maintained according to the regulations of the Institutional Animal Care and Use Committee of the University of Pennsylvania. Mice were anesthetized using isoflurane and, for xenograft tumor models, HT-1080 cells (2 x 10^6 cells in 0.2 mL PBS) were injected into the left flank by subcutaneous injection.

In vitro assessment of radiosensitization

The radiosensitization effects of GSM were assessed using a γ-h2ax assay to quantify the number of DNA double-stranded breaks (DSBs) per unit cell area. The assay was performed using HT-1080 cells, plated at 100,000 cells per well in 4-well chamber slides (Nunc Lab-Tek II CC2 Chamber Slide System, Thermo Scientific, Waltham, MA). Three different treatment conditions were evaluated: 100 nm GSMs at a concentration of 100 μg Au/mL, 100 nm AuNP-only micelles (GPMs) at 100 μg Au/mL, and no micelles. After a 24-hour incubation period, the samples were irradiated with 4 Gy of radiation (150 kVp, 10 mA) using the SARRP at the Perelman School of Medicine of the University of Pennsylvania. Three cohorts of treatment slides were used, one each for the time points T = 0 hours (no radiation), T = 6 hours post-radiation, and T = 12 hours post-radiation. At each time point, cells were fixed in 10% neutral buffered formalin (Sigma-Aldrich) for 10 minutes. After being rinsed with PBS, the nuclei were stained with Hoechst 33342 (25 μM) for 15 minutes. Slides were then permeabilized with 0.5% Triton X-100 in PBS and exposed to a blocking buffer composed of PBS, 0.5% Triton X-100,

5% normal chicken serum, and 1% BSA, for 30 minutes at room temperature. Cells were then incubated overnight in a humidified chamber at 4°C with mouse monoclonal anti-phosphohistone γ-h2ax primary antibody (JBW301, Upstate) at 1:1500 dilution in PBS (with 0.5% Triton X-100 and 1% BSA). After approximately 24 hours, slides were washed with PBS, and a chicken anti-mouse Alexa 594 secondary antibody (Molecular Probes) was applied at 1:1000 dilution in PBS (with 0.5% Triton X-100 and 1% BSA) for 1 hour. Finally, slides were incubated for 12 hours with ProLong Gold antifade reagent (Invitrogen) and coverslips applied. Fifteen images were captured of the each slide using a Deltavision deconvolution microscope (Applied Precision) equipped with a 60x (1.42 NA) oil-immersion lens and thermoelectrically cooled 12-bit monochrome CCD camera. Images were recorded as z-stacks with 0.3 μm steps. Each image was then processed and analyzed in order to quantify the number of foci (DSBs) per unit cell area using a custom ImageJ macro developed by co-author M. Vido.

In vitro characterization of dose-dependent radiosensitization effects

The dose dependence of 100 nm GSMs on radiosensitization was evaluated using a clonogenic assay. Briefly, HT-1080 cells were grown to confluence, as described above, and plated at increasing cell concentrations ranging from 200 cells to 4,000 cells in 60 mm x 15 mm Petri dishes. Prior to irradiation at 150 kVp, 10 mA, the media was aspirated away and 3 mL of 100 nm GSMs in media were applied to each plate. Each plate was then exposed to 0 Gy, 2 Gy, 4 Gy, or 6 Gy of radiation, with plates originally seeded with higher cell concentrations receiving the higher doses of radiation. Following radiation, the GSM media was aspirated away and replaced with fresh media. The assay was completed once for each of the following GSM concentrations: 0 μg Au/mL, 25 μg

Au/mL, 50 μg Au/mL, 100 μg Au/mL, and 200 μg Au/mL. After waiting 14 days, colonies were stained with methylene blue. The surviving fraction was then calculated as S = (number of colonies counted) / (cells seeded * %plating efficiency). Survival curves were fit to the linear quadratic model, where $S = \exp[-(\alpha D + \beta D^2)]$, for the dose, D, and the constants, α and β. A sensitizer enhancement ratio was computed for each GSM treatment condition by first computing the mean inactivation dose (MID),[48] where $\text{MID} = \frac{1}{2}\sqrt{\frac{\pi}{\beta}} * e^{z^2} * (1 - \text{erf}(z))$, for $z = \frac{\alpha}{2\sqrt{\beta}}$. The SER for a given GSM concentration was then equal to the ratio SER = (MID for radiation alone) / (MID for radiation + GSMs). GSMs were sterilized before use in this assay by prior irradiation for 500 minutes at 11 Gy/min.

Blood distribution, clearance, and tumor delivery

Three nude mice with HT-1080 tumor xenografts were injected intravenously under anesthesia with 100 nm GSMs in PBS at dose of 400 mg Au/kg body weight. Post-injection, 10 μL blood samples were collected via the tail-nick method from each animal at the following times: 0.5, 1, 2, 4, 6, 8, and 24 hours. After the final aliquot of blood was collected, the animals were sacrificed and the brain, thyroid, heart, lungs, liver, spleen, small bowel, large bowel, kidneys, inguinal lymph nodes, tumor, skin, bone, and muscle were removed from each animal. Organ samples were washed with dH_2O to minimize contamination from any nanoparticles still circulating in the blood. The blood samples and organs were then analyzed for gold content by ICP-OES. Organ samples were weighed into Teflon PFA vials (Savillex, Minnetonka, MN, USA) and digested overnight at 37°C with 70% nitric acid to digest the organic material. HCl was added the next day

to dissolve the AuNPs. Blood samples were dissolved directly in aqua regia. Blood GSM content was calculated as the percent of the injected dose per gram of blood analyzed (%ID/g). Organ GSM content was similarly calculated as the percent of the injected dose present per gram of organ/tumor tissue.

Toxicity studies

Approximately 6 week old female nu/nu nude mice were randomized into four groups of 3 animals per group receiving 650 mg Au/kg or sham-injected with PBS. Animals were weighed and observed regularly for clinical signs of toxicity. Animals were euthanized by CO_2 1 day and 8 days after intravenous injections and 0.3 mL blood was removed from the right ventricle immediately after the cessation of breathing. Blood chemistry analytes included blood urea nitrogen (BUN), albumin, alanine aminotransferase (ALT), aspartate aminotransferase (AST), alkaline phosphatase, total bilirubin, cholesterol, creatinine, and gamma-glutamyl transpeptidase (GGT).

In vivo testing of GSMs as a radiosensitizer and MR contrast imaging agent

Four cohorts of mice were prepared with HT-1080 fibrosarcoma tumors in their left, hind flank as described above. One cohort (n = 8) was preserved as an untreated control. The next cohort (RT-only, n = 8) was irradiated with 6 Gy of radiation at 17 kVp and 10 mA using the SARRP. Another cohort (GSM-only, n = 7) was injected intravenously with 100 nm GSMs in PBS at a dose of 400 mg Au/kg body weight. Prior to contrast administration, the final cohort (GSM+RT, n = 7) was first imaged by CT (55 kVp, 5 mAs) and MRI (GEMS sequence, 200 ms TR, 5 ms TE). Next, the GSM+RT mice were injected as described above with 100 nm GSMs. Twenty four hours later, post-

injection images were acquired using MRI and CT, followed by a single 6 Gy irradiation at 150 kVp and 10 mA. Tumor volumes were monitored thrice weekly using a dial caliper, and the tumor volume was computed as $V = (\pi/6)*A*B*C$, for A, B, and C, the three tumor diameters. Mice were deemed ready to enter the treatment protocol when their average tumor diameter was between 7 and 8 mm. Mice were sacrificed if their average tumor volume rose above 1,300 mm^3, if their tumors became severely ulcerated, or if the mice appeared emaciated (as per IACUC regulations). Progression was defined as occurring on the first of three consecutive days of increasing volume, following the initial period of tumor shrinkage after irradiation. Remission was defined as occurring on the first of three consecutive days of zero palpable tumor volume, following the initial period of tumor shrinkage post-irradiation.

Pre- and post-contrast MR images were analyzed using ImageJ software. The average intensity inside a region of interest (ROI) drawn around the tumor and inside a region of nearby muscle was computed for each image. The relative signal intensity (rSI) was computed as the ratio of average intensity inside the tumor ROI to average intensity inside the muscle ROI for a given image. Finally, the contrast enhancement of a given mouse was then computed as the ratio of post-contrast and pre-contrast CT scores.

Using tumor volume data, the average initial rate of tumor shrinkage post-radiation was computed for the GSM+RT mouse cohort. The initial rate of tumor shrinkage was computed using the largest tumor volume reached before the tumor began shrinking and the tumor volume reached approximately 15 days later (or on the first day of tumor remission, if it occurred before 15 days). These average tumor shrinkage rates

were then correlated to the contrast enhancement for the mice from which they were derived.

Numerical and statistical analysis

All numerical and statistical analysis was performed in Microsoft Excel. Where appropriate, a Student's t-test was used to determine if differences were statistically significant. For the survival studies, the Prism 5 (GraphPad software) was used to perform log-rank survival analysis on data presented in Kaplan-Meier curves. All error bars are reported as standard error of the mean.

3.4 Results and Discussion

Physical characterization of GSMs

Dodecanethiol-terminated AuNPs and oleic acid-stabilized SPIONs were synthesized with mean diameters of approximately 1.9 nm and 12 nm respectively, as measured by transmission electron microscopy (TEM) (Figure 3.2). Using an oil-in-water emulsion method, GSMs were then prepared with a mean hydrodynamic diameter of 100 nm and low polydispersity (PDI < 0.10) (Figure 3.1b). Although the different sizes of the AuNPs and SPIONs allow TEM to provide a cursory determination that both particle types have been incorporated into the micelles (Figure 3.1c**)**, the presence of both Au and Fe was further verified through energy dispersive X-ray spectroscopic analysis of the micelles (Figure 3.1d-e). Furthermore, the spatial arrangement of particles in the micelles was examined using tomographic electron microscopy. These data illustrate that SPIONs can be found throughout the entire GSM volume, interspersed with the smaller AuNPs, and are not restricted to either the center or the periphery of the hydrophobic core.

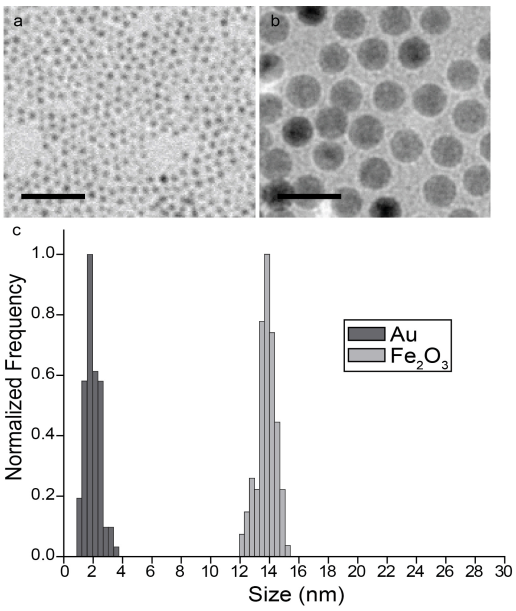

Figure 3.2. Electron micrographs of **(A)** AuNPs and **(B)** SPIO nanoparticles were acquired using a JEOL 1010 transmission electron microscope (scale bars = 30 nm). **(C)** The size distribution of AuNPs and SPIO nanoparticles was determined by measuring the diameter of 50 individual particles. The average diameters of these particles are 2.20 ± 0.44 nm and 13.6 ± 2.72 nm (± standard deviation), for AuNPs and SPIONs respectively.

The average mass ratio of gold-to-iron in these samples was 5.53 ± 0.50:1, as determined by inductively coupled plasma optical emission spectroscopy (ICP-OES). GSMs were easily mass-producible and yielded a longitudinal relaxivity r_1 = 0.536 ± 0.121 $mM^{-1}s^{-1}$ and a transverse relaxivity r_2 = 232.9 ± 11.7 $mM^{-1}s^{-1}$ at 1.41 T (60 MHz) (Figure 3.3). The zeta potential of GSMs was -1.55 ± 0.19 mV.

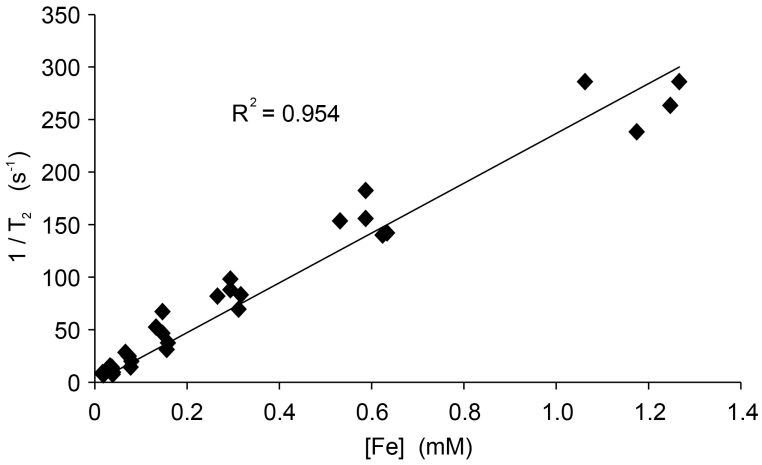

Figure 3.3. GSM transverse relaxivity (r_2) was measured using a Bruker mq60 tabletop MR relaxometer (1.41 T, 60 MHz) for five different batches of GSMs. The average r_2 relaxivity for these batches was found to be 236.9 mM^{-1} s^{-1}.

Assessment of GSM imaging characteristics

To assess the lower detection limits of GSMs via CT (Figure 3.1f) and MR (Figure 3.1g), phantom images were acquired using decreasing concentrations of GSMs dispersed in deionized water. GSMs were compared to micelles containing AuNPs only, i.e. gold-loaded polymeric micelles (GPMs),[18] to determine the effects of substituting SPIONs for AuNPs on CT contrast.

The concentration at which both GSMs and GPMs showed a statistically significant difference in Hounsfield units from baseline (HU of deionized water = 0) was 500 μg Au/mL (at 55 kVp, 0.5 mA), which was consistent with previous studies.[21] There was no significant difference in the Hounsfield units between the GSM or GPM wells, indicating that, at this Au:Fe ratio, the addition of Fe had no substantial effect on CT contrast. Figure 3.1g shows that the lower detection limit for detecting GSMs by T_2 weighted MR was 12.5 μg Au/mL (3.48 μg Fe/mL). No MR contrast from baseline was detected using GPMs for all concentrations, which was expected given that GPMs do not

contain any paramagnetic material. Therefore, 40-fold less GSMs are required for detection via MR imaging than either GSMs or GPMs for detection via CT imaging.

Evaluation of GSM radiosensitizing properties

To evaluate the radiosensitization effects of GSMs *in vitro*, HT-1080 human fibrosarcoma cells were irradiated (4 Gy) or mock irradiated in the presence of GSMs (100 μg Au/mL), GPMs (100 μg Au/mL), or no micelles, and analyzed for double-stranded breaks (γ-h2ax staining) (Figure 3.4a). The number of DNA double-stranded breaks correlates with the overall absorbed radiation dose.[22,23] It was found that the number of γ-h2ax foci / 100 μm^2 (observed as bright fluorescent spots) was enhanced by 1.4 and 2.2 times at 6 hours and 12 hours post-radiation respectively (Figure 3.4b), when either GPMs or GSMs were applied, compared with radiation alone. Both GSMs and GPMs provide statistically similar amounts of radiosensitization *in vitro*. Immunofluorescent images revealed very low levels of γ-h2ax foci in unirradiated cells, regardless of the presence of GPMs or GSMs.

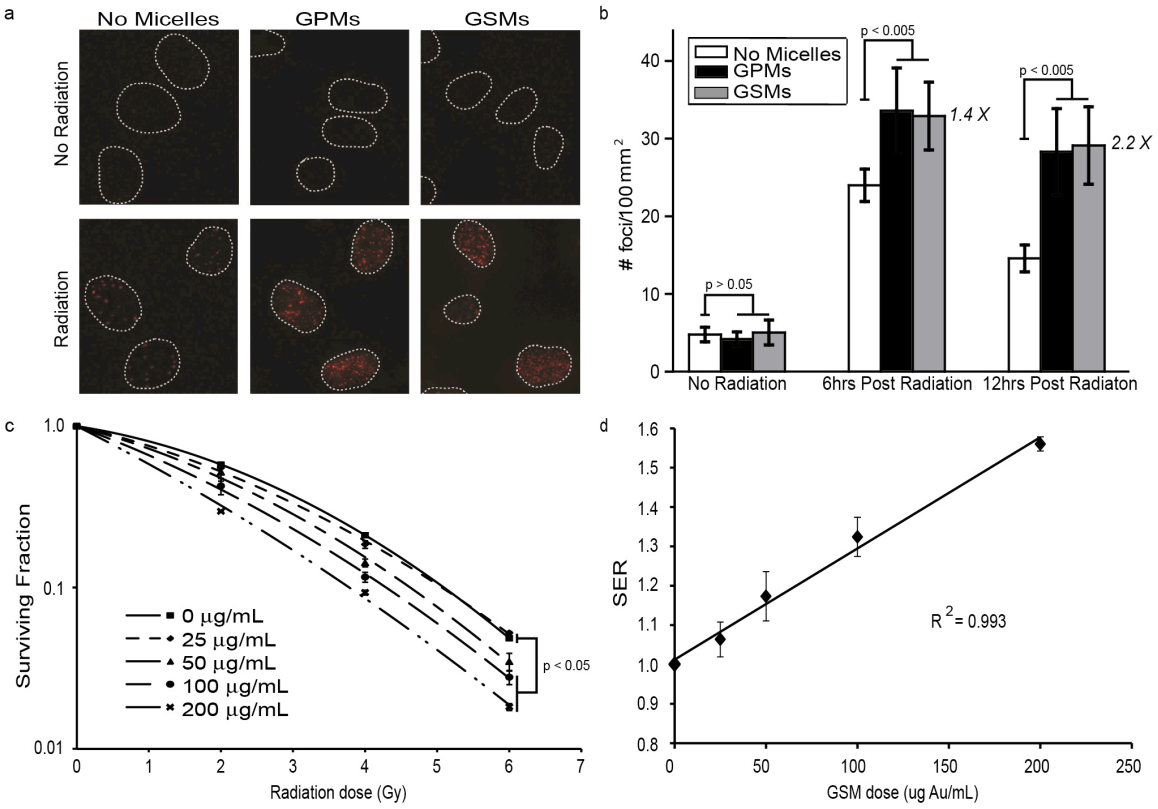

Figure 3.4. *In vitro* evaluation of radiation induced DNA double-stranded breaks and cell survival in the presence and absence of GSMs/GPMs. **(A)** Immunofluorescent imaging of γ-h2ax foci in HT-1080 cells incubated with GSMs (100 µg Au/mL), GPMs (100 µg Au/mL) or without micelles in the absence (top) or presence (bottom) of irradiation (4 Gy, 150 kVp). **(B)** Quantitative analysis of γ-h2ax foci density (# foci/um^2) for n > 100 cells in each treatment group. Error bars represent 95% confidence intervals. The number of γ-h2ax foci / 100 µm^2 (observed as bright fluorescent spots) was enhanced by 1.4 and 2.2 times at 6 hours and 12 hours post-radiation respectively. **(C)** Clonogenic assay of HT-1080 cells treated with and without GSMs (25, 50, 100, and 200 µg Au/mL) and given radiation doses of 0, 2, 4 and 6 Gy (150 kVp). Error bars represent the mean survival ± standard error of at least three replicates. **(D)** Plot of sensitizer enhancement ratio (SER) vs concentration of GSMs. The SER increases linearly as the GSMs concentration is also increased (R^2 = 0.993).

Clonogenic assays were performed on HT-1080 cells that were treated with increasing GSM concentrations and radiation at 4 Gy, revealing a dose dependent

response to both radiation dose and GSM concentration *in vitro* (Figure 3.4c). The sensitizer enhancement ratio (SER), a measure of how effectively a radiosensitizer reduces tumor cell proliferation, increased linearly (Figure 3.4d, $R^2 = 0.993$, slope $p < 0.001$) as the concentration of GSMs was increased. The SER for a GSM dose of 100 μg Au/mL was 1.32, which is comparable to the SER for other AuNP formulations found in the literature.[17,24]

GSM Pharmacokinetics and phamacodynamics

To evaluate the pharmacokinetic and pharmacodynamic properties of GSMs, the blood clearance profile (Figure 3.5a), organ biodistribution (Figure 3.5b), and blood chemistries (Table 3.1) were acquired following intravenous injection of GSMs into HT-1080 tumor-bearing, nu/nu mice. The clearance of GSMs from circulation followed a bi-exponential profile with a 1.45 h half-life for the distribution phase and a 17.5 h half-life for the elimination phase (Figure 3.5a).

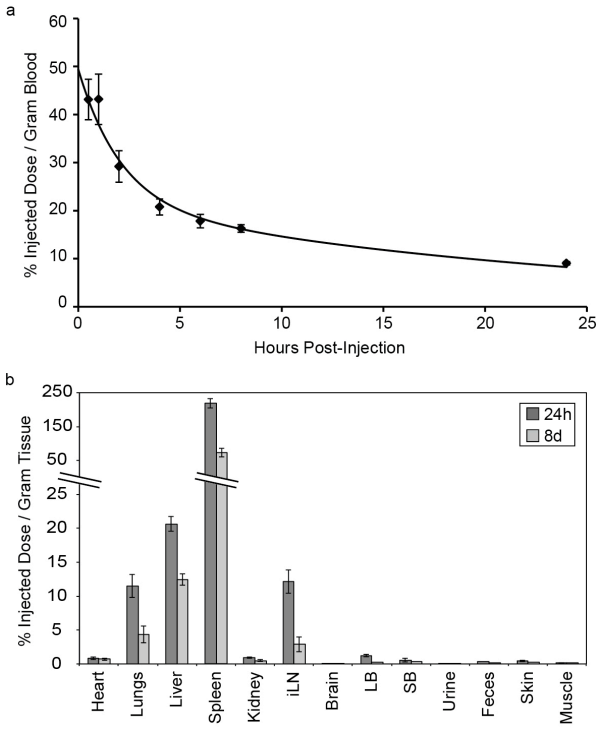

Figure 3.5. Blood clearance profile of GSMs. **(A)** ICP-OES analysis of gold content in blood at various times following the intravenous administration of GSMs to mice (n = 3). **(B)** ICP-OES analysis of gold distribution at 24 hours and 8 days following the administration of GSMs. The percent injected dose per gram of tissue was calculated by measuring the concentration of gold in excised organs *via* ICP-OES. There is a statistically significant decrease in the content of gold in tumors of mice receiving GSMs ($p < 0.05$).

Table 3.1. Blood Chemistry* Serum clinical chemistry of mice injected with 450 mg Au/kg GSMs (0.2 mL) and sampled at 24 hours and 1 week compared with mice sham injected with phosphate buffered saline (0.2 mL). All values were within normal limits and n = 3 for all groups. Data is recorded ± standard error.

	BUN	**Albumin**	**ALT**	**AST**	**Alk. Phos.**
Day 1 GSMs	25.7 ± 3.2	3.1 ± 0.3	501 ± 149	927 ± 183	157 ± 48
Control	24.3 ± 1.3	2.7 ± 0.3	430 ± 290	506 ± 194	111 ± 13
Day 8 GSMs	21.5 ± 3.6	2.4 ± 0.1	121 ± 18	336 ± 78	109 ± 26
Control	16.0 ± 3.7	2.3 ± 0.7	318 ± 190	421 ± 227	78 ± 18
	GGT	**Total Bil.**	**Cholesterol**	**Creatinine**	
Day 1 GSMs	45.4 ± 16.9	4.5 ± 0.9	200 ± 4	0.10 ± 0.2	
Control	15.2 ± 7.3	1.7 ± 0.7	91 ± 2	0.18 ± 0.2	
Day 8 GSMs	15.0 ± 4.7	1.1 ± 0.2	112 ± 26	0.13 ± 0.2	
Control	27.0 ± 9.4	1.5 ± 0.6	173 ± 45	0.18 ± 0.2	

*BUN, creatinine, total bili (total bilirubin), and cholesterol are in units of mg/dL. ALT, AST, alk. phos. (alkaline phosphatase), and GGT are in units of U/L. Albumin is in units of g/dL. Blood samples were obtained from mice injected with 400 mg Au/kg of GSM or sham injected with saline. Data is recorded ± standard error.

The organ biodistribution of GSMs, as percent injected dose per gram of tissue (%ID/g), was acquired 24 hours and 8 days post-injection of GSMs. The high proportion of GSMs found in the spleen and liver suggest that GSMs are cleared primarily through the reticuloendothelial system, as has been previously observed for other PEG-*b*-PCL micelle formulations.[18] It is interesting to note that there is high GSM uptake within the inguinal lymph nodes, an observation consistent with GSM extravasation and/or trafficking of cells from other lymphoid organs.

Gold is primarily excreted within feces, with very little found in the urine. Similar amounts of gold are found in the feces on both day 1 and day 8 post-injection, suggestive of continual excretion. Accordingly, the concentration of Au found in the spleen and the

liver decreases significantly over the course of a week. This result is very encouraging, as most tissue biodistribution studies that have been performed following the injection of AuNPs composed of a single, large gold core (> 10 nm) have indicated very poor excretion profiles.[25-28] For example, it has been found that there is only a 9% fall in the content of gold in the liver from day 1 to 6 months, following the intravenous injection of 40nm AuNPs.[28] It is hypothesized that the encapsulation of very small (1.9 nm) AuNPs into a larger GSM construct may facilitate more rapid dissolution and excretion than larger, single-particle systems.

The intravenous injection of GSMs (400 mg Au/kg) into healthy mice led to no signs of illness, change in activity, or weight loss (Figure 3.6). Notably, the amount of gold administered was well below the LD_{50}, which was previously reported to be 3.2 g Au/kg.[29] A toxicological analysis of mice 1 day and 8 days following the administration of GSMs (400 mg Au/kg) revealed blood chemistries that were not statistically different from those of saline injected controls (Table 3.1).

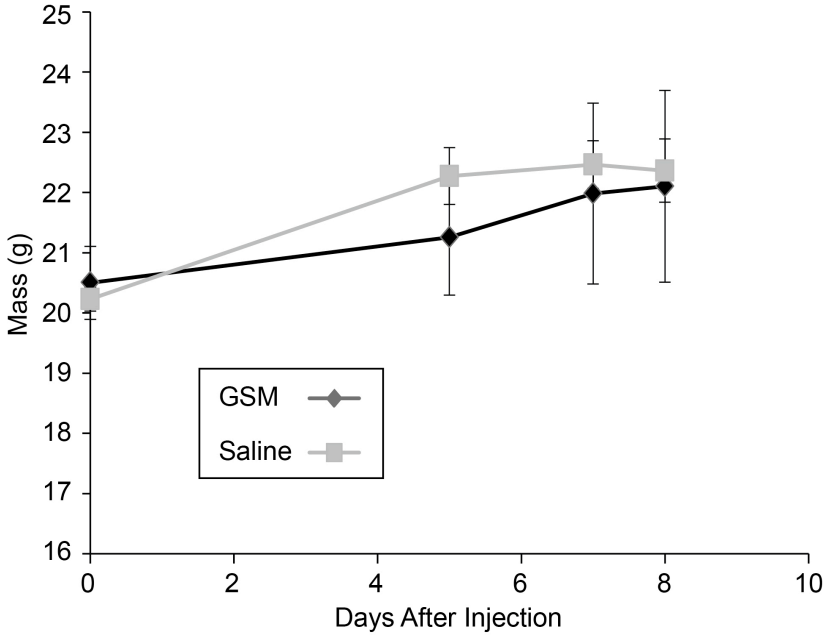

Figure 3.6. Whole animal weights of tumor-free mice treated with 400 mg Au/kg GPMs compared with mice sham injected with phosphate buffered saline. Data reflect average weights (n = 3) for each group. The average weights of the two cohorts do not differ significantly over the studied time period ($p > 0.05$).

In vivo imaging and therapy

HT-1080 cells were injected subcutaneously into the back left flank (2×10^6 cells in 0.1 mL of PBS) of 6 week old female nu/nu mice. Tumors were grown until the mean tumor diameter was approximately 7 – 8 mm. Next, tumor-bearing mice were split into four cohorts – (i) no treatment (n = 8); (ii) GSMs only (400 mg Au/kg, n = 7); (iii) radiation therapy (RT) only (6 Gy, n = 8); (iv) GSMs plus RT 24 h post-injection (n = 7). Animals in the GSM+RT cohort were imaged using MRI and CT both prior to and 24 h following GSM injection. After imaging, mice underwent tumor localized radiation therapy and were followed for 90 days with their tumor sizes measured periodically.

Representative pre- and post-contrast images of a single mouse using both CT and MRI are shown in Figure 3.7a-b. Note that at this GSM dosage no enhancement is visible

with CT imaging, but the tumor is hypointense on MRI, consistent with SPIONs accumulation, effectively revealing the proximal edge of the tumor. To quantitatively determine the amount of GSMs delivered to the tumor, an analogous study was performed (n = 3), whereby the tumors were harvested 24 hours post-injection and the gold content was analyzed by ICP-OES. It was determined that the tumors possessed 6.64% ID of Au/g tumor (6.64% ID of Fe/g, assuming intact GSMs). Upon adjusting for tumor volume, the average concentration of gold within the tumor was calculated to be 0.55 ± 0.17 mg Au/mL (99 ± 3 μg Fe/mL). This is at the lower detection limit for gold by CT (i.e. ~ 0.5 – 1.0 mg/mL), but well above the lower detection limit for SPION via MRI (i.e. ~ 0.87 – 1.74 μg Fe/mL). These tumor concentrations are also well above the 0.1 mg Au/mL needed for a radiosensitization effect, based on the *in vitro* analysis. A silver enhancement stain performed on tumor histology sections of mice injected with GSMs confirmed the presence of AuNPs throughout the tumor. No enhancement was observed in mice that were administered saline (Figure 3.7c).

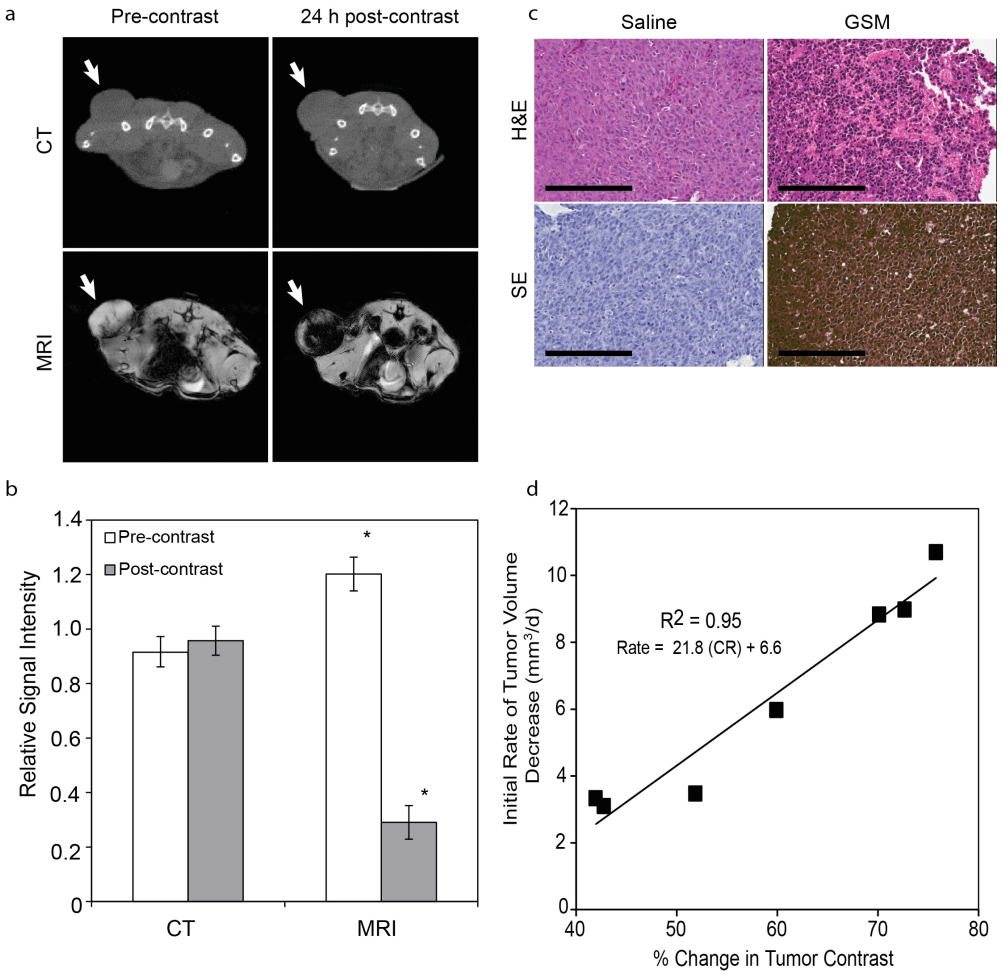

Figure 3.7. *In vivo* imaging and intensity analysis of a single nu/nu nude mouse with a HT1080 flank tumor. **(A)** Representative *CT* (top) and MR (bottom) images in the axial plane prior to injection (pre-contrast) and 24 h post-injection (postcontrast) of GSMs (400 mg Au/kg) (n = 7). Tumors are indicated by white arrows. No enhancement is visible via CT imaging. **(B)** Quantitative analysis of CT and MR images. Signal intensity of each tumor was normalized to adjacent paraspinal muscle. For contrast measurement, the relative signal intensity, RSI, was calculated as the quotient of the post-contrast to pre-contrast normalized tumor intensity. Statistically significant values of $p < 0.05$ are indicated with an asterisk. **(C)** Representative histologic sections of HT-1080 tumors excised from mice 24 hours after i.v. injection with saline (left) or GSMs (right) stained with H&E (top) and a silver enhancement (bottom). **(D)** Plot of initial rate of tumor volume decrease vs the % change in tumor contrast for all mice (n = 7) receiving GSMs (400 mg Au/kg) plus radiation therapy (6 Gy, 150 kVp) in the survival study (see Figure 5). There is a strong linear correlation between the contrast enhancement and tumor response ($R^2 = 0.95$).

Following imaging, mice were monitored for tumor growth and were sacrificed when the tumors reached the predetermined threshold volume (1,300 mm^3). The survival time was measured from the time of radiation (or mock irradiation). Mice that received GSMs prior to radiation therapy exhibited a statistically significant ($p < 0.05$) improvement in median survival (75.6 ± 9.2 d), compared to mice treated with radiation alone (50.4 ± 10.6 d) (Figure 3.8a). It should be noted that all mouse groups appeared to tolerate GSMs very well over the course of study with no observable changes in behavior or symptoms of hepatic or gastrointestinal toxicity, such as loss of appetite, diarrhea, or vomiting. The mean survival times for the control and GSM-only mice were not statistically different at 20.0 ± 2.5 d and 25.7 ± 2.6 d, respectively. The general observable trend in tumor growth post radiation therapy was a reduction in tumor growth, followed by a reduction in tumor volume and then either eventual tumor re-growth or remission (Figure 3.8b). A significantly larger ($p < 0.05$) proportion of mice from the GSM+RT group derived a complete response with no discernable tumor (71%) compared to the mice in the RT-only group (14%). Note that of the two surviving mice in the RT-only group, one mouse derived a complete response and the other mouse had a residual, palpable but stable mass at the end of the study period.

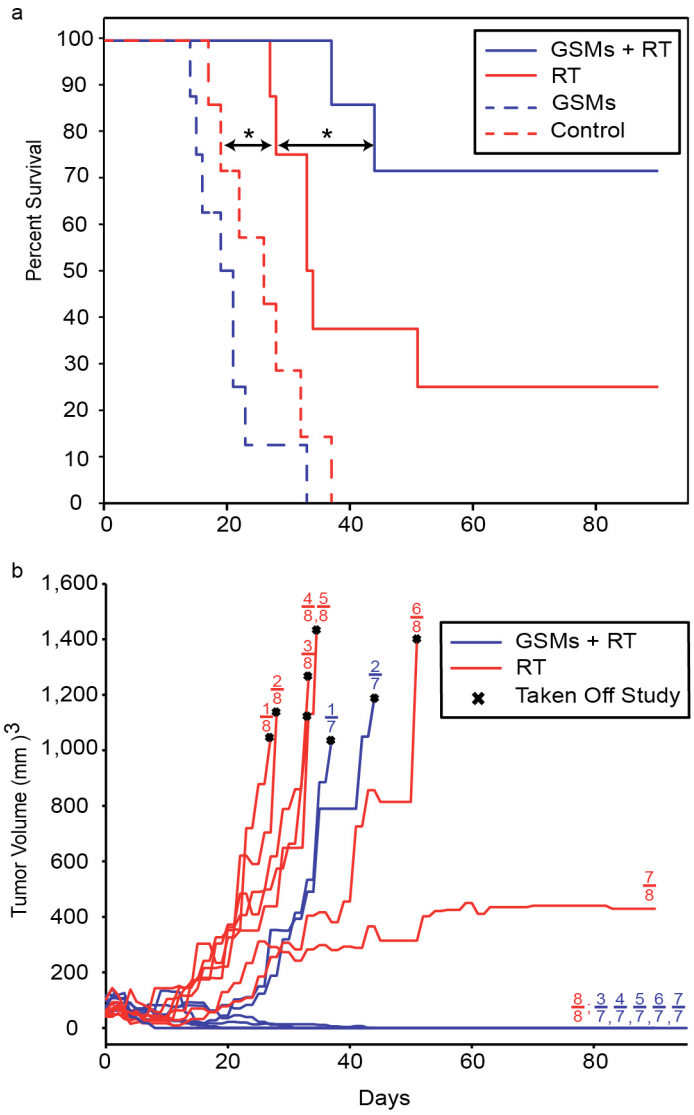

Figure 3.8. (A) A Kaplan-Meier survival analysis was performed for HT-1080 tumor-bearing mice receiving no treatment (n = 8, dotted grey line), GSMs only (n = 7); (dotted black line), radiation therapy (RT) only (n = 8, solid grey line), or radiation therapy plus 24 h intravenous injection of GSMs (n = 7, solid black line). GSMs were administered at a dose of 400 mg Au/kg. The radiation dose administered was 6 Gy at 175 kVp. The asterisk indicates statistical significance ($p < 0.05$). **(B)** Average tumor volumes over time of mice receiving GSMs with radiation therapy (solid line) or radiation therapy alone (dotted line).

To evaluate the predictive value of GSM–enhanced MR imaging, we compared the tumor contrast enhancement to the rate of tumor volume decrease following

irradiation. The analysis revealed a strong correlation (R^2 = 0.95) between contrast enhancement and tumor response (Figure 3.7d). This relationship is consistent with the *in vitro* data linking GSM dose to the efficacy of radiosensitization and provides a promising mechanism to guide follow-up treatment accordingly.

The GSMs reported here address the aforementioned disparity between the dose of gold-only particles needed to obtain therapeutic benefit and the dose needed for imaging enhancement. The MR imaging enhancement provided by GSMs was highly robust, due to their high transverse relaxivity (r_2 = 233 $mM^{-1}s^{-1}$) and consequent nanomolar sensitivity. This is similar to the characteristics of SPIO-only formulation[30] and allowed tumor boundaries to be readily identified and the extent of GSM uptake to be assessed. Therefore, GSMs could enable radiation oncologists in more accurately planning both the geometric and dosimetric aspects of radiation therapy.

Unlike many other dual imaging-treatment nanoparticles, which use chemotherapeutics as their payload,[31,32] GSMs are not inherently cytotoxic and only exert their therapeutic effects under the influence of ionizing radiation. Coupled with the need for lower concentrations to achieve imaging, these properties render GSM extraordinarily safe. Accordingly, the administration of GSMs did not result in any significant changes in weight, blood chemistry, or behavior.

At the radiation energies tested, GSMs provided a potent dose-dependent enhancement of DNA double-stranded breaks and SER *in vitro*. They also significantly increased survival and tumor response *in vivo*, compared with radiation treatment alone. The linear relationship between the contrast enhancement and therapeutic response further supports the dose dependent radiosensitization of tumor cells. The GSM-mediated

radiation enhancement effects are expected to allow physicians to increase the efficacy of a given overall dose or radiation therapy administered, with no incremental risk to normal tissues.

While MR contrast and therefore GSM localization correlated with the initial rate of tumor volume decrease, there was no correlation observed between the level of image contrast and overall therapeutic outcome. This dissociation of initial response and clinical end point may be due to differences in the tumor microenvironment (e.g. hypoxia, inflammatory reaction, heterogeneous vasculature), which predispose certain tumors to either an early, necrotic response or a delayed apoptotic response to radiation therapy. The relationship between gold-enhanced radiation therapy and the mechanism of tumor cell death bears further investigation.

The accumulation of GSMs in tumors is mediated by the EPR effect. However, EPR has been shown to vary from tumor to tumor with the level of tumor vascularization.[33-35] Differences in vascularization lead to variations in the tumoral delivery of nanoparticle-based therapeutic agents and thus a large variability in nanoparticle treatment efficacy.[36] However, because GSM-enhanced MR imaging can be used to quantify the tumor penetrance, tumor dosimetry planning can be adjusted accordingly.

While EPR alone may not be sufficient to produce widespread dissemination of GSMs throughout all tumors, the administration of GSMs over the course of a fractionated radiation therapy regiment may promote the spatially targeted delivery of GSMs into the tumor. Recent MRI studies have shown that radiation can increase the permeability of tumors to gadolinium in human patients.[39] Additionally, it has recently

been shown that radiation therapy can enhance the delivery of nanopolymers (diameter ≈ 40-70 nm),[40] pegylated near-infrared fluorescent probes,[41] and pegylated AuNPs (diameter ≈ 23 nm)[17] to tumors in murine models. These data suggest that targeted radiation therapy can enhance the uptake of circulating nanoformulations by increasing vascular and interstitial permeability.

At 150 kVp, the most likely mechanism for the dose enhancement effects of gold is the photoelectric effect,[8,9] leading to extensive DNA damage. The attenuation of X-rays with depth at this energy makes the treatment of superficial tumors by external beam radiation, the enhancement of brachytherapy, and the enhancement of intra-operative radiation therapy three possible applications for GSMs. Furthermore, other research has already illustrated the efficacy of gold nanoparticles in enhancing radiation therapy at higher, megavoltage energies (e.g. 6 MV) more commonly seen in the clinical treatment of deep-seated tumors.[24,42] As the photoelectric cross-section is nearly zero at these higher energies, the likely radiosensitization mechanism is not photoelectric, but potentially relies on the generation of reactive oxygen species to cause cellular damage or on other scattering mechanisms.[43,44] The use of platinum (atomic number $Z_{Pt} = 78$) to enhance proton beam therapy suggests that GSMs ($Z_{Au} = 79$) may also have a role in enhancing proton-mediated radiation therapy.[45]

3.5 Conclusions

In conclusion, incorporating GSMs with radiation therapy could augment cancer treatment by facilitating imaging, increasing the efficacy of therapy, and helping to predict response. Moreover, since GSMs are prepared using a highly modular synthetic pathway, additional components, including standard and alternative therapeutics could readily be incorporated into the micelle's core while targeting moieties (e.g. tumor-specific antibodies or Fab's) can be coupled onto the unobstructed micelle surface, further broadening the range and types of tumors that can be effectively treated. The extravasation properties of these particles may also make them useful in treating diseases localized to regional lymph nodes, such as Hodgkin's lymphoma. Therefore, it is envisioned that translation of GSM to oncology could have far reaching implications.

3.6 References

1. Moding, E.J., Kastan, M.B. & Kirsch, D.G. Strategies for optimizing the response of cancer and normal tissues to radiation. *Nat Rev Drug Discov* **12**, 526-542 (2013).
2. Seiwert, T.Y., Salama, J.K. & Vokes, E.E. The concurrent chemoradiation paradigm--general principles. *Nat Clin Pract Oncol* **4**, 86-100 (2007).
3. Eck, W.*, et al.* PEGylated gold nanoparticles conjugated to monoclonal F19 antibodies as targeted labeling agents for human pancreatic carcinoma tissue. *ACS Nano* **2**, 2263-2272 (2008).
4. Hainfeld, J.F., Slatkin, D.N. & Smilowitz, H.M. The use of gold nanoparticles to enhance radiotherapy in mice. *Phys Med Biol* **49**, N309-315 (2004).
5. Thakor, A.S.*, et al.* The fate and toxicity of Raman-active silica-gold nanoparticles in mice. *Sci Transl Med* **3**, 79ra33 (2011).
6. Thakor, A.S.*, et al.* Oxidative stress mediates the effects of Raman-active gold nanoparticles in human cells. *Small* **7**, 126-136 (2011).
7. Zavaleta, C.L.*, et al.* Preclinical evaluation of Raman nanoparticle biodistribution for their potential use in clinical endoscopy imaging. *Small* **7**, 2232-2240 (2011).
8. Hainfeld, J.F., Dilmanian, F.A., Slatkin, D.N. & Smilowitz, H.M. Radiotherapy enhancement with gold nanoparticles. *J Pharm Pharmacol* **60**, 977-985 (2008).
9. Rahman, W.N.*, et al.* Enhancement of radiation effects by gold nanoparticles for superficial radiation therapy. *Nanomedicine* **5**, 136-142 (2009).

10. Matsudaira, H., Ueno, A.M. & Furuno, I. Iodine contrast medium sensitizes cultured mammalian cells to X rays but not to gamma rays. *Radiat Res* **84**, 144-148 (1980).

11. Santos Mello, R., Callisen, H., Winter, J., Kagan, A.R. & Norman, A. Radiation dose enhancement in tumors with iodine. *Med Phys* **10**, 75-78 (1983).

12. Spiers, F.W. The influence of energy absorption and electron range on dosage in irradiated bone. *Br J Radiol* **22**, 521-533 (1949).

13. Cheng, N.N.*, et al.* Chemical enhancement by nanomaterials under X-ray irradiation. *J Am Chem Soc* **134**, 1950-1953 (2012).

14. McMahon, S.J.*, et al.* Nanodosimetric effects of gold nanoparticles in megavoltage radiation therapy. *Radiother Oncol* **100**, 412-416 (2011).

15. Hainfeld, J.F., Smilowitz, H.M., O'Connor, M.J., Dilmanian, F.A. & Slatkin, D.N. Gold nanoparticle imaging and radiotherapy of brain tumors in mice. *Nanomedicine* **8**, 1601-1609 (2013).

16. Joh, D.*, et al.* Theranostic gold nanoparticles modified for durable systemic circulation effectively and safely enhance the radiation therapy of human sarcoma cells and tumors. *Translational Oncology* (2013).

17. Joh, D.Y.*, et al.* Selective targeting of brain tumors with gold nanoparticle-induced radiosensitization. *PLoS One* **8**, e62425 (2013).

18. Al Zaki, A.*, et al.* Gold-Loaded Polymeric Micelles for Computed Tomography-Guided Radiation Therapy Treatment and Radiosensitization. *ACS Nano* (2014).

19. Popovtzer, R.*, et al.* Targeted gold nanoparticles enable molecular CT imaging of cancer. *Nano Lett* **8**, 4593-4596 (2008).

20. Wang, Y.J., Hussain, S.M. & Krestin, G.P. Superparamagnetic ironoxide contrast agents: physicochemical characteristics and applications in MR imaging. *Eur. Radiol.* **11**, 2319-2315 (2001).

21. Hainfeld, J.F.*, et al.* Micro-CT enables microlocalisation and quantification of Her2-targeted gold nanoparticles within tumour regions. *Br J Radiol* **84**, 526-533 (2011).

22. Illiakis, G. The role of DNA double strand breaks in ionizing radiation-induced killing of eukaryotic cells. *BioEssays* **13**, 641-648 (1987).

23. Ward, J.F. The yield of DNA double-strand breaks produced intracellularly by ionizing radiation: a review. *Int J Radiat Biol* **57**, 1141-1150 (1990).

24. Chithrani, D.B.*, et al.* Gold nanoparticles as radiation sensitizers in cancer therapy. *Radiat Res* **173**, 719-728 (2010).

25. Balasubramanian, S.K.*, et al.* Biodistribution of gold nanoparticles and gene expression changes in the liver and spleen after intravenous administration in rats. *Biomaterials* **31**, 2034-2042 (2010).

26. Cho, W.S.*, et al.* Acute toxicity and pharmacokinetics of 13 nm-sized PEG-coated gold nanoparticles. *Toxicol Appl Pharmacol* **236**, 16-24 (2009).

27. Niidome, T.*, et al.* PEG-modified gold nanorods with a stealth character for in vivo applications. *J Control Release* **114**, 343-347 (2006).

28. Sadauskas, E.*, et al.* Protracted elimination of gold nanoparticles from mouse liver. *Nanomedicine* **5**, 162-169 (2009).

29. Hainfeld, J.F., Slatkin, D.N., Focella, T.M. & Smilowitz, H.M. Gold nanoparticles: a new X-ray contrast agent. *Br J Radiol* **79**, 248-253 (2006).

30. Ai, H., *et al.* Magnetitie-loaded polymeric micelles as ultrasensitive magnetic-resonance probes. *Advanced Materials* **17**, 1949-1952 (2005).

31. Hong, G., *et al.* Folate-functionalized polymeric micelle as hepatic carcinoma-targeted, MRI-ultrasensitive delivery system of antitumor drugs. *Biomed Microdevices* **10**, 693-700 (2008).

32. Nasongkla, N., *et al.* Multifunctional polymeric micelles as cancer-targeted, MRI-ultrasensitive drug delivery systems. *Nano Lett* **6**, 2427-2430 (2006).

33. Fukumura, D. & Jain, R.K. Tumor microenvironment abnormalities: causes, consequences, and strategies to normalize. *J Cell Biochem* **101**, 937-949 (2007).

34. Hobbs, S.K., *et al.* Regulation of transport pathways in tumor vessels: role of tumor type and microenvironment. *Proc Natl Acad Sci U S A* **95**, 4607-4612 (1998).

35. Yuan, F., *et al.* Time-dependent vascular regression and permeability changes in established human tumor xenografts induced by an anti-vascular endothelial growth factor/vascular permeability factor antibody. *Proc Natl Acad Sci U S A* **93**, 14765-14770 (1996).

36. Karathanasis, E., *et al.* Imaging nanoprobe for prediction of outcome of nanoparticle chemotherapy by using mammography. *Radiology* **250**, 398-406 (2009).

37. Brizel, D.M., Sibley, G.S., Prosnitz, L.R., Scher, R.L. & Dewhirst, M.W. Tumor hypoxia adversely affects the prognosis of carcinoma of the head and neck. *Int J Radiat Oncol Biol Phys* **38**, 285-289 (1997).

38. Vaupel, P., Mayer, A. & Hockel, M. Tumor hypoxia and malignant progression. *Methods Enzymol* **381**, 335-354 (2004).

39. Cao, Y.*, et al.* Use of magnetic resonance imaging to assess blood-brain/blood-glioma barrier opening during conformal radiotherapy. *J Clin Oncol* **23**, 4127-4136 (2005).

40. Baumann, B.C.*, et al.* Enhancing the efficacy of drug-loaded nanocarriers against brain tumors by targeted radiation therapy. *Oncotarget* **4**, 64-79 (2013).

41. Baumann, B.C.*, et al.* An integrated method for reproducible and accurate image-guided stereotactic cranial irradiation of brain tumors using the small animal radiation research platform. *Transl Oncol* **5**, 230-237 (2012).

42. Jain, S.*, et al.* Cell-specific radiosensitization by gold nanoparticles at megavoltage radiation energies. *Int J Radiat Oncol Biol Phys* **79**, 531-539 (2010).

43. Kang, B., Mackey, M.A. & El-Sayed, M.A. Nuclear targeting of gold nanoparticles in cancer cells induces DNA damage, causing cytokinesis arrest and apoptosis. *J Am Chem Soc* **132**, 1517-1519 (2010).

44. Pan, Y.*, et al.* Gold nanoparticles of diameter 1.4 nm trigger necrosis by oxidative stress and mitochondrial damage. *Small* **5**, 2067-2076 (2009).

45. Porcel, E.*, et al.* Platinum nanoparticles: a promising material for future cancer therapy? *Nanotechnology* **21**, 85103 (2010).

46. Brust, M., Walker, M., Bethell, D., Schiffrin, D.J. & Whyman, R. Synthesis of Thiol-Derivatized Gold Nanoparticles in a 2-phase Liquid-Liquid System. *J. Chem. Soc. Chem. Commun.*, 801 (1994).

47. Park, J., *et al.* Ultra-large-scale syntheses of monodisperse nanocrystals. *Nat Mater* **3**, 891-895 (2004).

48. Belli, M. & Simula, S. The calculation of the mean inactivation dose by approximated methods. *Radiat Res* **128**, 112-114 (1991).

Chapter 4: Superparamagnetic Iron Oxide Nanoparticle Micelles Stabilized by Recombinant Oleosin for Targeted Magnetic Resonance Imaging

4.1 Abstract

A wide variety of nanoplatforms are being developed for the diagnosis and detection of malignancies. However, a major limitation of many of these approaches is that they exploit passive mechanisms of targeting. Passively targeted nanoparticles accumulate preferentially in tumors primarily due to the EPR effect, but nanoparticle retention is nonspecific relying primarily on high vascular permeability and poor lymphatic drainage at the tumor site. Conversely, actively targeted nanoparticles exploit targeting and binding to specific receptors present on tumor cells. Therefore the use of an actively targeted nanoplatform can achieve higher tumor retention, facilitate nanoparticle internalization for improved efficacy, and improve tumor specificity. To facilitate the introduction of targeting molecules onto micelle formulations, a naturally occurring surfactant protein oleosin was used to stabilize superparamagnetic iron oxide clusters. Functionalization of these particles with targeting ligands (e.g. Her2/neu affibody) was then achieved by simply fusing the biologically relevant motifs to oleosin using standard cloning techniques. Using this approach, nanoparticle formation and functionalization was completed in one step without the requirement of post-synthesis surface modifications. Specific targeting was confirmed through cell binding assays in the presence and absence of a competitive inhibitor and quantified using magnetic relaxation

techniques. We envision that oleosin stabilized nanoparticle micelles will represent a promising platform for therapeutic and imaging applications, since size, charge, targeting moiety, and solubility can all be easily modified with high precision and essentially no variability.

4.2 Introduction

Superparamagnetic iron oxide (SPIO) nanoparticles have gained interest for use as magnetic resonance contrast agents, with the ability to provide T_2 weighted contrast enhancement on MR imaging applications.[1-4] Their strong contrast enhancing capabilities have rendered them useful for molecular imaging applications with various targeting molecules being conjugated to the surfaces of SPIO nanoparticles.[5-8] These strategies have the potential to increase tumor accumulation, specificity, and therapeutic efficacy. The prerequisite for any targeted nanoparticles is the successful bioconjugation of ligands onto the nanoparticle surface, some which have low reaction efficiencies, require multiple conjugation steps, and often create products with poorly oriented antibodies. Developing recombinant proteins that can stabilize SPIO nanoparticles would allow for the functionalization of particles in the formulation step by directly modifying the protein through molecular biology.

We chose to engineer the naturally occurring surfactant protein oleosin.[9] Oleosin is expressed in plant seeds with the native function of stabilizing fat reservoirs called oil bodies. The protein consists of three domains, a central hydrophobic domain flanked by two hydrophilic arms on the C- and N-terminus.[9, 10] The protein resembles a hairpin structure with a proline knot embedding in the central hydrophobic domain that forces a 180° turn.[11] Recombinant oleosin has been exploited for it surfactant nature in many biotechnology applications.[12-17]

4.3 Materials and Methods

Gene synthesis

Genes were created using standard molecular biology techniques. All mutants were confirmed through DNA sequencing. Oleosin-30G(-)was created from the template Oleosin-30G[18] using sequential PCR steps with the following primers: 1S 5' – GATCAGCATGATCAACACACCGGTGACCAGCTCACCCACCCACAGGACCAGC AACAAGGCCCCTCAACCGGCGAACTCGCTCTCGGTGCGACTCC -3', 2S 5' – AATTCAATAGGATCCGAAGCCACCACAACCAACGACCAGCACCATGTCACCA CCACCCAACCCCAAGATCAGCATGATCAACACACC – 3', 1AS 5' – TATCTGCTGGCCCAAGTCGTTCGTGTTCTGGCCCGTCTGCTCCCCCACATCCT GCAATTCCCCGTTCACGTTATCCTGCCACTGAAACCCGGTAACACC – 3', 2AS 5' – TTCTGCCCTTCGTTCCCACCACCCTGACCCTGACCCTGGCCCTGGTCA CCCATTTCATGGGCCGTATGCTGTATCTGCTGGCCCAAGTCG – 3', 3AS 5' – TTTATGAATCTCGAGTCAGTCATCGTGGTGGTGGTGGTGGTGGTTCCCCCCTT CGTTCTGCCCTTCGTTCCCACC – 3'. The Oleosin-30G(-) PCR product was cloned in the expression vector pBamUK. The Her2 affibody was amplified using the primers Her2 1S 5' – GATGCGCAGGCGCCGAAAGGCGGCGGTGGCGGTAGC – 3', and Her2 fusion AS 5' – GGTTGTGGTGGATCCTTTCGGCGCCTGC – 3' and cloned into the vector pBamUK-Oleosin-30G to create pBamUK-Her2-Oleosin-30G. The gene for the expression of the Her2 affibody alone was created using the following primers: Her2 1S 5' – GATGCGCAGGCGCCGAAAGGCGGCGGTGGCGGTAGC – 3', and Her2 AS 5' – TAGATAATTCTCGAGTTTCGGCGCCTGCGCATCG – 3' and cloned into

pBamUK. pBamUK adds a 6-histidine tag onto the C-terminus of the protein to allow for immobilized metal affinity chromatography (IMAC).

Protein production and purification

Mutants were expressed under the control of the lac promoter in *E. coli* (BL21 DE3, Stratagene). The protein mutants were solubilized according to the B-PER protocol and purified using IMAC following the Hispur Ni-NTA resin protocol. Mutants were expressed under the control of the lac promoter in *E. coli* (BL21 DE3, Stratagene). Cultures were grown until OD_{600}~0.7 and induced with isopropyl β-D-1-thiogalactopyranoside to a final concentration of 1.0 mM (Fisher Scientific). Cells were pelleted at 5,000 RPM and frozen at -20°C prior to purification. Oleosin-30G(-) and the Her2 affibody were expressed solubly, whereas the fusion Her2-Oleosin-30G was expressed in inclusion bodies. The protein mutants were solubilized according to the B-PER protocol for soluble or insoluble proteins respectively. Unpurified protein solutions were added to Ni-NTA beds (Hispur Ni-NTA resin, Thermo Scientific) and allowed to bind to the column ~ 1 hour at room temperature. Protein was washed and eluted in fractions according to the Hispur protocol. Protein concentration was measured using a Nanodrop-1000 (Fisher Scientific). Buffer exchanges were completed with dialysis or with centrifugal filters (Amicon Ultra, 3 kDa, Millipore).

Protein sequences

Oleosin-30G(-)

GSEATTTNDQHHVTTTQPQDQHDQHTGDQLTHPQDQQQGPSTGELALGATPLF

GVIGFSPVIVPAMGIAIGLAGVTGFQWQDNVNGELQDVGEQTGQNTNDLGQQIQ
HTAHEMGDQGQGQGQGGGNEGQNEGGNHHHHHHDD

Her2-Oleosin-30G

VDNKFNKEMRNAYWEIALLPNLNNQQKRAFIRSLYDDPSQSANLLAEAKKLND
AQAPKGSTTTYDRHHVTTTQPQYRHDQHTGDRLTHPQRQQQGPSTGKLALGAT
PLFGVIGFSPVIVPAMGIAIGLAGVTGFQRDYVKGKLQDVGEYTGQKTKDLGQKI
QHTAHEMGDQGQGQGQGGGKEGRKEGGKLEHHHHHH

Her2

VDNKFNKEMRNAYWEIALLPNLNNQQKRAFIRSLYDDPSQSANLLAEAKKLND
AQAPKLEHHHHHH

Sodium dodecyl sulfate polyacrylamide gel electrophoresis (SDS-PAGE)

SDS-PAGE gels were run in MES buffer with NuPAGE Novex 4–12% Bis-Tris mini gels (Invitrogen). After electrophoresis, the gels were stained with SimplyBlue Safestain (Invitrogen) and destained in water overnight. The resulting gel was imaged with a Kodak Gel Logic 100 Imaging station.

Matrix assisted laser desorption/ionization time of flight mass spectroscopy (MALDI-TOF)

MALDI-TOF spectra were used to confirm the molecular weights of the mutants. Sample spots were created with 0.5 μL protein in pH 7.4 phosphate buffered saline (PBS) and 0.5 μL saturated sinapinic acid solution (50/50 acetonitrile/water + 0.1% TFE). Spectra were collected on an Ultraflextreme MALDI-TOF (Bruker, Billerica, MA).

Circular dichroism (CD)

Far-UV CD spectra were collected on an AVIV 410 spectrometer (AVIV Biomedical Inc.) at 25 °C in 1 mm quartz cuvettes. Protein concentration was 10 μM in 10 mM phosphate, 140 mM NaF due to the high signal from the Cl^- ion in PBS.

Fe_2O_3 synthesis

Superparamagnetic iron oxide nanoparticles were synthesized according to a protocol adapted from Cheon et al.[19] Briefly, 0.6 mmol of $Fe(CO)_5$ dissolved in 0.3 mL of ortho-dichlorobenzene (ODCB) was rapidly injected into a hot solution containing 1.2 mL of ODCB and 0.6 mmol of dodecylamine (DDA). The resulting mixture was maintained at 180ºC under aerobic conditions. During this process, the initial orange color of the solution gradually changed to slightly brownish black. After 9 hours, the resulting solution was cooled to room temperature and an approximately 3-fold volume excess of toluene was added to adjust the solubility of the nanocrystals. The nanoparticle solution was then centrifuged to remove nanoparticle aggregates. After adding ethanol into the remaining solution, resulting black flocculates were isolated by centrifugation.

Nanoparticle assembly and purification

Fe_2O_3-oleosin micelles were synthesized using an oil in water emulsion and purified using sequential centrifugation as previously reported.[20] Fe_2O_3-oleosin micelles were synthesized using an oil in water emulsion and stabilized with Oleosin-30G(-). Fe_2O_3 nanoparticles were dissolved in toluene at a concentration of 80 mg/mL. Protein stocks were diluted into sterile PBS to a concentration of 2 mg/mL. The FeO nanoparticles in toluene (50 μL) were directly injected to the protein solution and

sonicated until a uniform emulsion was created and no visible iron aggregates existed. The emulsion was allowed to dry overnight at room temperature. The particles were purified using sequential centrifugation. The solution was centrifuged at 380 RCF for 10 minutes and large aggregates were removed in the pellet. The supernatant was centrifuged at 4646 RCF for 30 minutes and the resulting supernatant was removed. Two pellets exist from this spin, a soft soluble pellet, and a hard, insoluble pellet of aggregates. The soft pellet was removed and used for further studies. The nanoparticles were concentrated and solution exchanges were completed using centrifugal filters (Amicon Ultra, 50 kDa MWCO, Millipore).

Dynamic light scattering

Dynamic light scattering of nanoparticle solutions was performed on samples in PBS using a Malvern Zetasizer Nano ZS (Westborough, Massachusetts). Each sample was run in triplicate.

Cryogenic transmission electron microscopy (Cryo-TEM)

Cryogenic transmission electron microscopy was performed at the University of Pennsylvania in the Nanoscale Characterization Facility (Philadelphia, PA). Lacey formvar/carbon grids (Ted Pella) were rinsed in chloroform to remove the formvar template. The resulting grids were carbon coated with a Quorum Q150T ES carbon coater (Quorum Technologies, United Kingdom). Grids were cleaned with hydrogen/oxygen plasma for 15 seconds using the Solarus Advanced Plasma System 950 (Gatan, Pleasanton, CA). A 2 μL drop of nanoparticles in PBS was deposited onto the grid and added to a Gatan Cp3 cryoplunger (Gatan, Pleasanton, CA). The samples were blotted by

hand and plunged into liquid ethane. Grids were transferred to a Gatan CT3500TR cryoholder (Gatan, Pleasanton, CA) and immediately inserted into a JEOL 2100 HRTEM (JEOL, Tokyo, Japan) operating at 200 keV. Micrographs were imaged with an Orius SC200 digital camera.

Stability

Particles were incubated at 37°C for 5 days in either PBS or DMEM plus glutamax, 10% FBS, and penicillin streptomycin. DLS measurements were taken daily to monitor for particle degradation or aggregation.

Cell lines

NIH/3T3 and T6-17 cells (i.e., NIH/3T3 cells engineered to stably express the Her2/neu receptor, kindly provided by Dr. Mark Greene, University of Pennsylvania) were maintained in Dulbecco's modified Eagle's medium (DMEM) supplemented with 10% fetal bovine serum, 1% penicillin/streptomycin at 37°C, and 5% CO_2.

Cell Viability Assay

The viability and proliferation of cells in the presence of FeO-oleosin nanoparticles were evaluated by 3-[4,5-dimethylthialzol-2-yl]-2,5-diphenyltetrazolium bromide (MTT, Sigma) assay. The assay was performed in triplicate in the following manner. NIH/3T3 cells were seeded into 96-well plates at a density of 1 **x** 10^4 cells per well in 200 μL of media and grown overnight. The cells were then incubated with various concentrations of FeO-oleosin (0, 0.025, 0.05, 0.075, 0.1, and 0.15 mg Fe/mL) for 4 hours. Following incubation, cells were incubated in media containing 0.1 mg/mL of MTT for 1 hour. Thereafter, MTT solution was removed, and precipitated violet crystals

were dissolved in 200 ìL of DMSO. The absorbance was measured at 560 nm.

Her2/neu targeting

T6-17 and NIH/3T3 cells were incubated with 100 μg Fe/mL of Her2/neu-targeted SPIO micelles for 45 minutes in full media in triplicate. The media was removed and the cells were washed with PBS two times to remove any unbound micelles. Cells were trypsinized and counted. Cell suspensions were diluted to 0.4×10^6 cells/mL and T_2 relaxation times were measured using a benchtop relaxometer (Bruker mq60).

4.4 Results and Discussion

We have previously engineered oloesin to self-assemble into vesicles, fibers or sheets by creating a family of truncation mutants thereby varying the hydrophilic/hydrophobic ratio of the surfactant protein.[21] Further truncations of the hydrophobic block have led to soluble oleosin mutants that spontaneously self-assemble in aqueous solution as a function of concentration.[22] These proteins can be highly engineered for specific applications. We present here the engineering of oleosin mutants to stabilize and target iron oxide protein micelles for enhanced magnetic resonance imaging (Figure 4.1A).

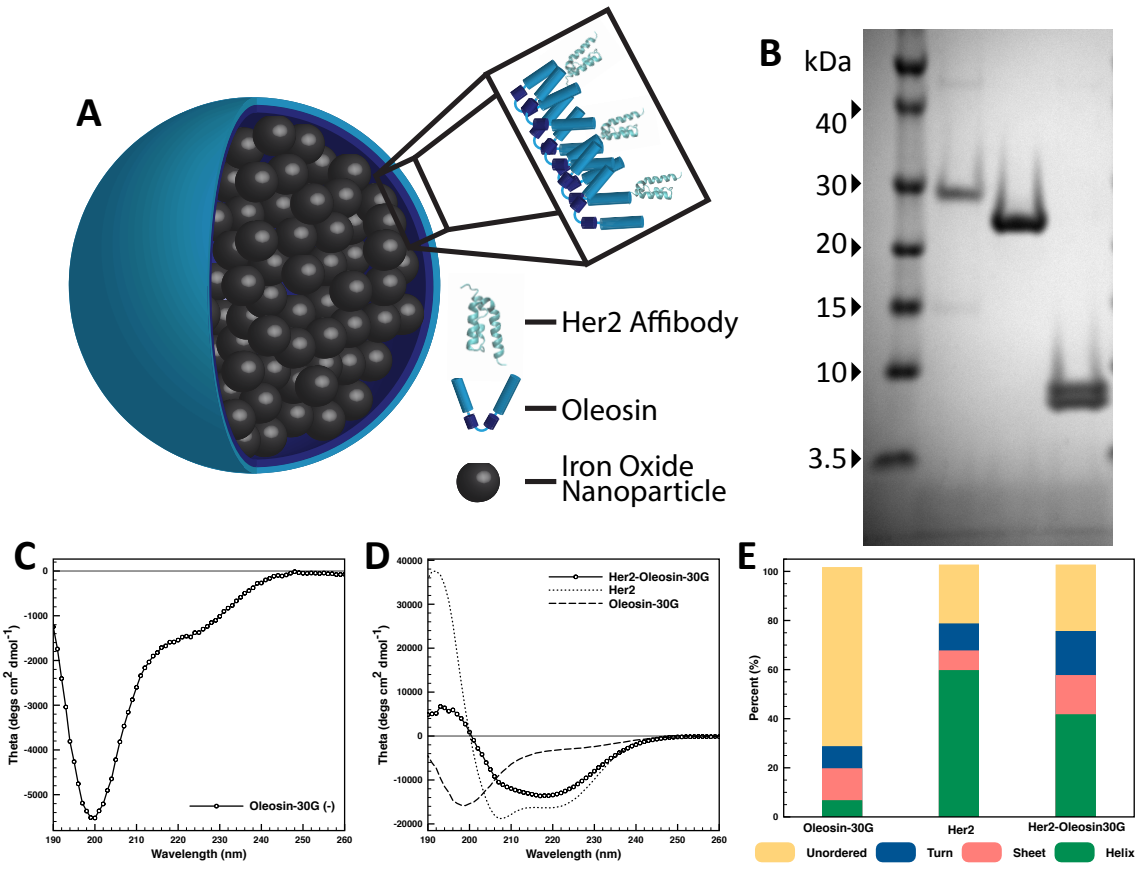

Figure 4.1. (A) Cartoon depiction of Her2/neu targeted iron oxide nanoparticle micelles stabilized by oleosin. **(B)** Protein purity is accessed to be > 95% pure by SDS-PAGE (lane 1: Oleosin-30G(-), lane 2: Her2/neu-Oleosin-30G, lane 3: Her2/neu affibody). **(C)** Circular dichroism indicates an unordered structure for the charged mutant Oleosin-30G(-). **(D)** CD spectra for the fusion Her2/neu-Oleosin-30G show contributions from the helical Her2/neu affibody and the unordered Oleosin-30G. **(E)** CDSSTR analysis of CD spectra shows increased helical structure in the fusion compared to Oleosin-30G indicating that the affibody is likely folded on the N-terminus of the oleosin mutant.

Two oleosin genes were engineered, one to stabilize the FeO micelles and a second to target the resulting clusters to Her2/neu+ cells. Previously it has been shown that oleosin can be engineered to stabilize various interfaces such as emulsion droplets[21] and bubbles.[18] In order to provide adequate repulsion between the micelles, we mutated the hydrophilic arms of oleosin-30G to be negatively charged. Negative nanoparticles

have also been shown to limit nonspecific cell targeting.[23-25] Specifically, all positive amino acids as well as any tyrosine residues in the hydrophilic arms were mutated to Q, N, D, or E depending on the location and local charge. The negative charge was spread evenly across the hydrophilic arms with an average negative amino acid every six residues. This mutant is called Oleosin-30G(-). To directly target Her2/neu+ cancer cells, we have fused a Her2/neu affibody onto the N-terminus of the oleosin mutant Oleosin-30G. This targeted mutant is named Her2/neu-Oleosin-30G. The Her2/neu affibody was expressed independently as a competitive inhibitor for cell studies. Mutants were made using standard molecular biology techniques and cloned into the expression vector pBamUK, which adds a 6-histine tag on the C-terminus of the protein for immobilized metal affinity chromatography (IMAC). Oleosin mutants were confirmed through DNA sequencing. Vectors were transformed into the *Escherichia coli* strain BL21 (DE3) for expression. Her2/neu-Oleosin-30G was insoluble and expressed in inclusion bodies whereas Oleosin-30G(-) was soluble. Mutants were purified using IMAC. Protein yields were ~ 24 mg, ~ 80 mg, and ~ 65 mg of purified protein per liter of culture for Her2/neu-Oleosin-30G, Oleosin-30G(-), and Her2/neu respectively. SDS-PAGE indicates highly purified products after IMAC (Figure 1B). The band for Oleosin-30G(-) runs much higher than expected on the gel, likely due to its highly negative charge. Molecular weights were confirmed with MALDI-TOF (Oleosin-30G(-) expected: 14956, measured: 14958; Her2/neu-Oleosin-30G: expected: 21714, measured: 21713; Her2/neu expected: 7771, measured: 7773).

Protein secondary structure was elucidated with circular dichroism. The parent molecule Oleosin-30G is a highly unordered protein.[18] CD indicates that Oleosin-30G(-)

remains unordered after the various mutations to the hydrophilic arms (Figure 4.1C). The secondary structure of Her2/neu-Oleosin-30G was investigated to ensure correct affibody folding as a fusion partner. The Her2/neu affibody is a highly helical protein (Figure 4.1D) and when fused to oleosin, the Her2/neu-Oleosin fusion displays structure from the helical affibody and the unordered oleosin backbone (Figure 4.1D). The spectra were fit with the CDSSTR analysis method using Dichroweb (Figure 4.1E).[26-28] The analysis shows clear helical structure in the fusion protein indicating that the affibody is likely folded in the fusion.

SPIO-oleosin micelles were assembled through an emulsion method. SPIO nanoparticles solubilized in toluene were injected into solutions of protein in PBS. The emulsion was sonicated and the toluene was allowed to evaporate overnight at room temperature. This led to a heterogeneous mixture of micelles. SPIO-Oleosin micelles were purified using stepwise centrifugation.[20] Cryo-TEM of the various separation fractions indicates large aggregated particles are removed in pellet after low RCF spins and excess protein and small particles in the supernatant of the high RCF spins (Figure 4.2). The mass ratio of the particles to the protein, the oil volume fraction, and the particle stabilization coat all play an important role in the formation of packed nanoclusters. The oil volume fraction and mass ratio of protein to iron was optimized. Previous studies used an oil volume fraction of 4.8% for particle formation and a 4:4 ratio of nanoparticle to surfactant (mg:mg).[20] We found that decreasing the volume fraction of toluene in the emulsion to 1.2% and increasing the protein concentration greatly affected the resulting structures. The optimal particles were created by injecting 50 uL of toluene containing 4 mg of SPIO-dodecylamine coated nanoparticle into a 4 mL solution of

protein in PBS at a concentration of 2 mg/mL (Figure 4.3).

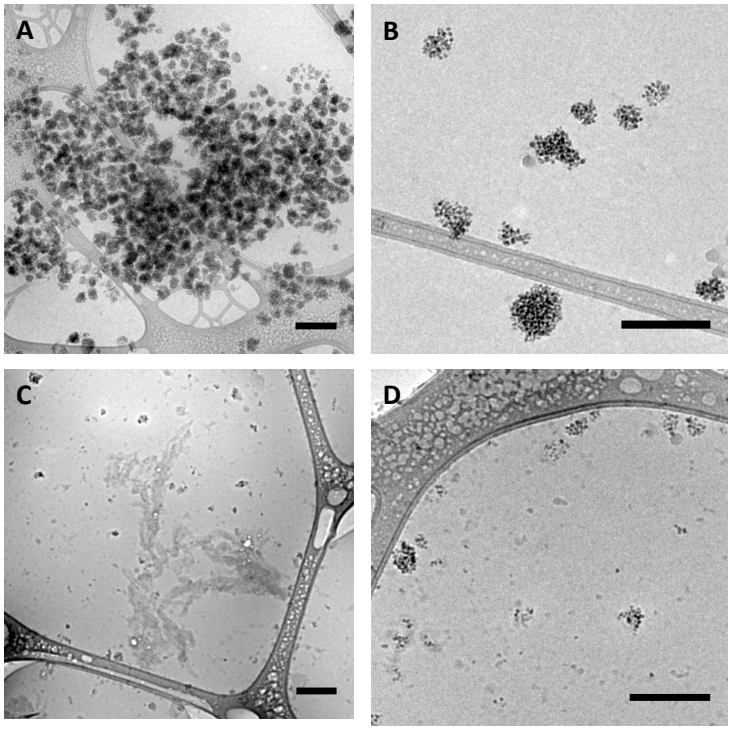

Figure 4.2. Cryo-TEM micrographs of the various fractions during purification. **(A)** The hard, insoluble pellet after the high RCF spin shows large aggregates of particles stuck together. **(B)** The soft, soluble pellet that is extracted and used for further studies shows individual nanoclusters. **(C-D)** The supernatant after the high RCF contains excess protein (C) and small nanocluster (D). All scale bars are 200 nm.

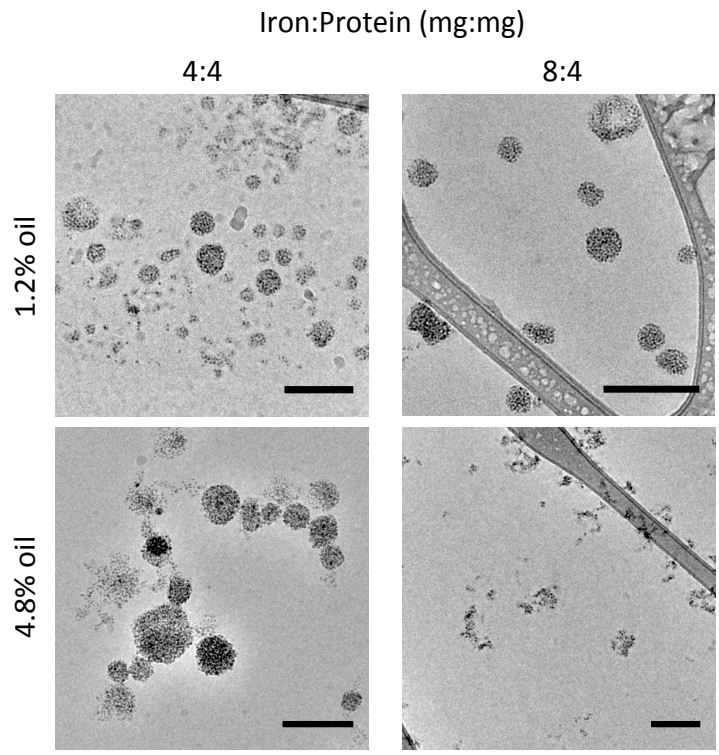

Figure 4.3. Optimization of iron-to-protein ratio and oil volume fraction. Increasing the amount of surfactant and decreasing the volume of toluene used in the emulsification led to highly packed particles with little-to-no aggregates present after purification.

Dynamic light scattering of the purified particles show a monodisperse population with an average hydrodynamic diameter of 113 nm (peak: 127 nm, PDI = 0.104) (Figure 4.4A). Purified particles were imaged using cryo-TEM (Figure 4.4B). The micrograph displays tightly packed iron oxide nanoparticles and no visible excess protein on the particles. Particles from three independent batches were directly measured from micrographs and found to have an average diameter of 74 ± 33 nm (n = 660 particles) (Figure 4.4C). As expected, the number average diameter measured in micrographs is less than the hydrodynamic diameter measured by DLS. The DLS data are skewed to higher diameters due to increased intensity of scattering from larger particles.

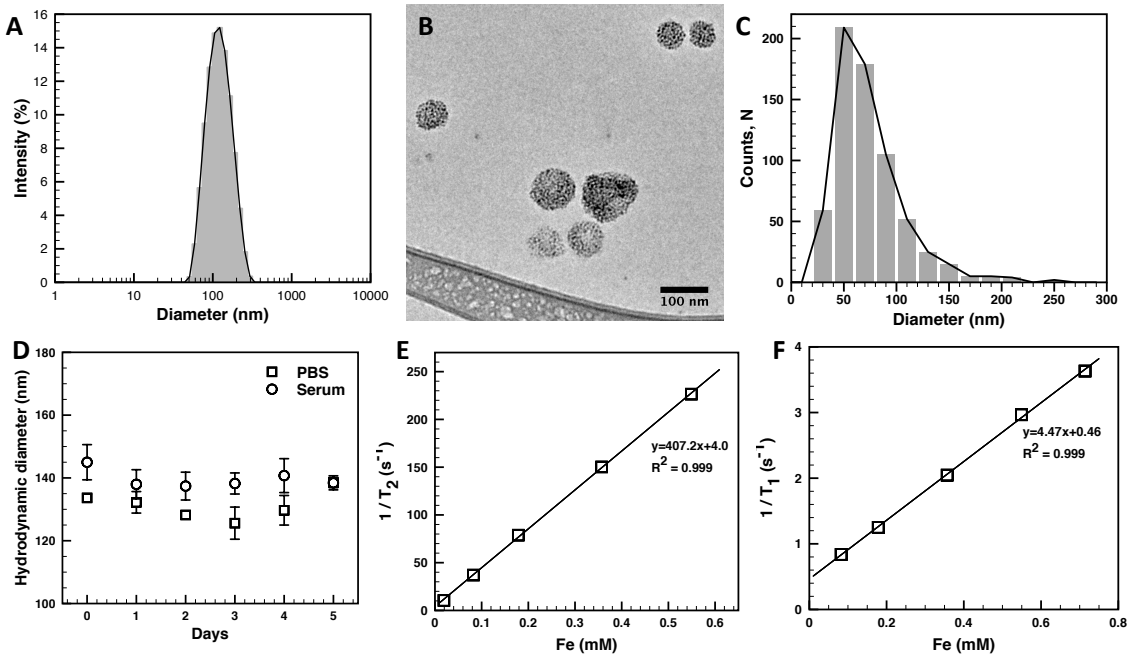

Figure 4.4. (A) Dynamic light scattering reveals a monodisperse population of micelles with an average diameter of 113 nm (PDI=.104). **(B)** Cryo-TEM micrograph of FeO micelles stabilized by Oleosin-30G(-) in PBS. **(C)** Particle size distribution measured directly from cryo-TEM images. The average particle size was found to be 74 ± 33 nm (standard deviation, n = 660 particles). This diameter is significantly lower than the hydrodynamic diameter from DLS due to the increased scattering from larger particles. **(D)** Protein stabilized particles are stable over 5 days in buffer (PBS) and serum at 37°C as measured by DLS. **(E)** Particles show high relaxivity with an r_2 value of 407.2 ± 4.0 mM^{-1} s^{-1}. **(F)** The r_1 value was found to be 4.47 ± 0.46 mM^{-1} s^{-1}.

The surface charge of SPIO particles has been shown to have significant impact in the uptake by cells.[4] Zeta potential measurements indicated a negative surface charge at of -12.5 ± 1.7 mV. The high negative charge is needed to provide repulsive electrostatic interactions between the emulsion droplets during particle formation reducing aggregation. The particles show long-term stability in buffer (PBS) and serum with no significant change in the hydrodynamic diameter over 5 days at 37°C (Figure 4.4D). The particles display extremely high relaxivity with an r_2 value of 407.2 ± 4.0 s^{-1} mM^{-1} and an

r_1 value of 4.47 ± 0.46 s^{-1} mM^{-1}. The potential cytotoxicity of the nanoparticles was assessed using an MTT assay. Over all concentrations, cell viability remained above 97% for the 4-hour incubation with particles (Figure 4.5A).

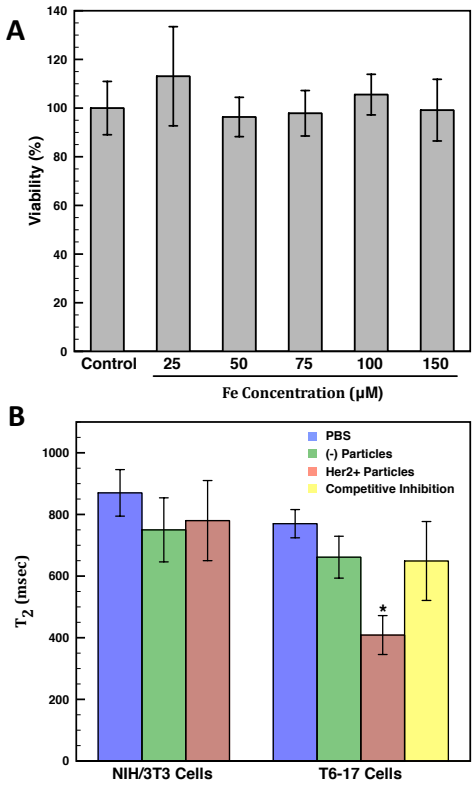

Figure 4.5. (A) Particles show no toxicity between 25 and 150 μM after 4 hours of incubation at 37°C with NIH/3T3 cells. **(B)** Functional evaluation of the Her2/neu SPIO-oleosin micelles conjugates. SPIO-oleosin and Her2/neu-SPIO-oleosin were incubated with either Her2/neu+ and Her2/neu- cells in the presence and absence of excess free affibody. Free affibody served as a competitive inhibitor to confirm specific binding of the Her2/neu receptor. Relaxivity measurements of cells incubated with SPIO-oleosin micelles or Her2/neu-SPIO-oleosin micelles were acquired.

Table 4.1. Physical and magnetic properties of oleosin stabilized nanoparticles

Hydrodynamic diameter (nm)	113 ± 36
Number diameter (nm)	74 ± 33
Zeta potential (mV)	-12.5 ± 1.7
R_2 (mM^{-1} s^{-1})	407.2 ± 4.0
R_1 (mM^{-1} s^{-1})	4.47 ± 0.46
R_2/R_1	91.1

Her2/neu+ targeted micelles were created by blending Her2/neu-Oleosin with Oleosin-30G(-) at 10% by weight in the PBS solutions (0.8 mg Her2/neu-Oleosin-30G: 7.2 mg Oleosin-30G(-)). The micelles were prepared and purified in the same manner. The blending of the targeted mutant into the micelles did not change the size of the micelles as measured by DLS (Figure 4.6A) or the stability of the particles over time (Figure 4.6B). The surface charge of the particles remains negative but slightly increased to -10.7 ± 0.8 mV.

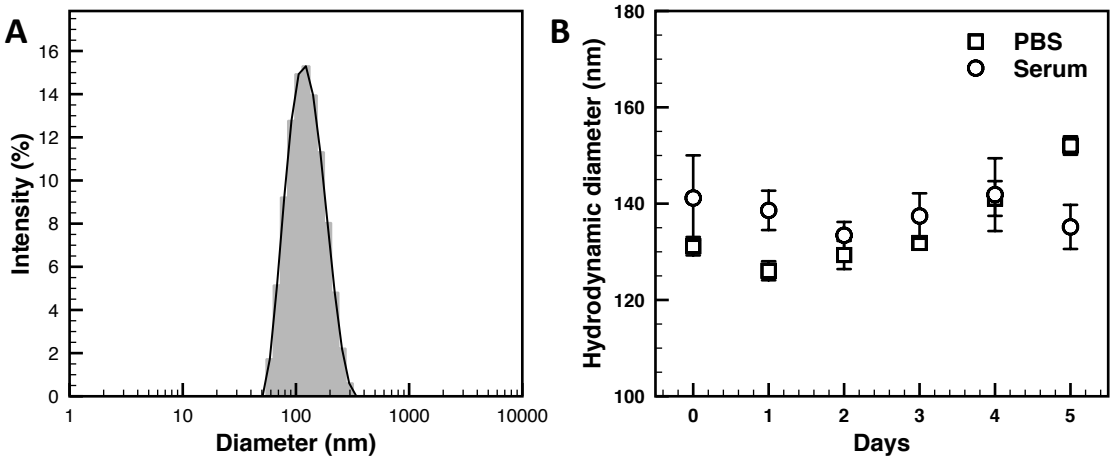

Figure 4.6. Characterization of Her2+ functional nanoparticles. **(A)** DLS spectra shows monodisperse particles with a peak at 131 nm (PDI = 0.11) indicating that the Her2-Oleosin-30G blending into the micelles does not affect the overall size. **(B)** Functionalized particles are stable in PBS and serum for up to 5 days at 37°C.

FeO micelles were incubated with Her2/neu- (NIH/3T3) and Her2/neu+ (T6-17) cells at a concentration of 100 μg/mL for 45 minutes. The T_2 relaxation time for the NIH/3T3 cells showed no difference between negative control particles, targeted particles, or cells incubated without particles, indicating little to no nonspecific binding (Figure 4.5B). In the Her2/neu+ cell line, the cells incubated with the targeted particles show a significantly lower T_2 relaxation time, consistent with the presence of SPIO, compared to cells with the negative control particles or cells incubated without particles. A competitive binding study was completed by adding excess Her2/neu affibody to the T6-17 cells before and during the incubation with the targeted particles. The affibody competition led to a significant increase in the T_2 time. Therefore, these results provide clear evidence that Her2/neu oleosin micelles provide cell specific targeting.

4.5 Conclusions

This work demonstrates the engineering of the naturally occurring surfactant protein oleosin to stabilize and target FeO nanoparticle micelles to Her2/neu+ cells. The functionalization of these particles is trivial due to the ease of incorporating biologically relevant motifs into the protein through molecular biology. These particles are extremely stable and display high relaxivity. We envision oleosin stabilized nanoparticle micelles will represent a promising platform for targeted enhanced imaging applications. Specifically, varying the surface charge and appending specific stealth ligands[29] to the particles could engineer nanoparticle shells to be nontoxic and maintain long circulation times.

4.6 References

1. Weissleder, R. et al. Superparamagnetic Iron-Oxide - Enhanced Detection of Focal Splenic Tumors with Mr Imaging. *Radiology* **169**, 399-403 (1988).
2. Weissleder, R. et al. Ultrasmall Superparamagnetic Iron-Oxide - Characterization of a New Class of Contrast Agents for Mr Imaging. *Radiology* **175**, 489-493 (1990).
3. Shapiro, E.M., Skrtic, S. & Koretsky, A.P. Sizing it up: Cellular MRI using micron-sized iron oxide particles. *Magnet Reson Med* **53**, 329-338 (2005).
4. Thorek, D.L.J. & Tsourkas, A. Size, charge and concentration dependent uptake of iron oxide particles by non-phagocytic cells. *Biomaterials* **29**, 3583-3590 (2008).
5. Wu, S.C., Chen, Y.J., Lin, Y.J., Wu, T.H. & Wang, Y.M. Development of a Mucin4-Targeting SPIO Contrast Agent for Effective Detection of Pancreatic Tumor Cells in Vitro and in Vivo. *J Med Chem* **56**, 9100-9109 (2013).
6. Petri-Fink, A. & Hofmann, H. Superparamagnetic iron oxide nanoparticles (SPIONs): From synthesis to in vivo studies - A summary of the synthesis, characterization, in vitro, and in vivo investigations of SPIONs with particular focus on surface and colloidal properties. *Ieee T Nanobiosci* **6**, 289-297 (2007).
7. Matuszewski, L. et al. Cell tagging with clinically approved iron oxides: Feasibility and effect of lipofection, particle size, and surface coating on labeling efficiency. *Radiology* **235**, 155-161 (2005).
8. Hui, J.Z. et al. Facile Method for the Site-Specific, Covalent Attachment of Full-Length IgG onto Nanoparticles. *Small*,(2014).

9. Huang, A.H.C. Oil Bodies and Oleosins in Seeds. *Annu Rev Plant Phys* **43**, 177-200 (1992).

10. Alexander, L.G. et al. Characterization and modelling of the hydrophobic domain of a sunflower oleosin. *Planta* **214**, 546-551 (2002).

11. Abell, B.M. et al. Role of the proline knot motif in oleosin endoplasmic reticulum topology and oil body targeting. *Plant Cell* **9**, 1481-1493 (1997).

12. Bhatla, S.C., Kaushik, V. & Yadav, M.K. Use of oil bodies and oleosins in recombinant protein production and other biotechnological applications. *Biotechnol Adv* **28**, 293-300 (2010).

13. Peng, C.C., Chen, J.C.F., Shyu, D.J.H., Chen, M.J. & Tzen, J.I.C. A system for purification of recombinant proteins in Escherichia coli via artificial oil bodies constituted with their oleosin-fused polypeptides. *J Biotechnol* **111**, 51-57 (2004).

14. Scott, R.W. et al. Elevation of oil body integrity and emulsion stability by polyoleosins, multiple oleosin units joined in tandem head-to-tail fusions. *Plant Biotechnol J* **8**, 912-927 (2010).

15. Chang, M.T. et al. Elevating Bioavailability of Curcumin via Encapsulation with a Novel Formulation of Artificial Oil Bodies. *J Agr Food Chem* **61**, 9666-9671 (2013).

16. Chiang, C.J., Lin, C.C., Lu, T.L. & Wang, H.F. Functionalized nanoscale oil bodies for targeted delivery of a hydrophobic drug. *Nanotechnology* **22** (2011).

17. Chiang, C.J., Lin, L.J., Lin, C.C., Chang, C.H. & Chao, Y.P. Selective internalization of self-assembled artificial oil bodies by HER2/neu-positive cells. *Nanotechnology* **22** (2011).

18. Angilè, F.E., Vargo, K.B., Sehgal, C.M., Hammer, D.A. & Lee, D. Recombinant Protein-Stabilized Monodisperse Microbubbles With Tunable Size Using a Valve-based Microfluidic Device. *Submitted for Publication* (2014).

19. Cheon, J.W. et al. Shape evolution of single-crystalline iron oxide nanocrystals. *J Am Chem Soc* **126**, 1950-1951 (2004).

20. Al Zaki, A. et al. Gold-Loaded Polymeric Micelles for Computed Tomography-Guided Radiation Therapy Treatment and Radiosensitization. *Acs Nano* **8**, 104-112 (2014).

21. Vargo, K.B., Parthasarathy, R. & Hammer, D.A. Self-assembly of tunable protein suprastructures from recombinant oleosin. *P Natl Acad Sci USA* **109**, 11657-11662 (2012).

22. Vargo, K.B., Sood, N., Moeller, T.D., Heiney, P.A. & Hammer, D.A. Characterization and Functional Targeting of Spherical Micelles Assembled from Soluble Recombinant Oleosin Mutants. *Submitted for Publication* (2014).

23. Verma, A. & Stellacci, F. Effect of Surface Properties on Nanoparticle-Cell Interactions. *Small* **6**, 12-21 (2010).

24. Cho, E.C., Au, L., Zhang, Q. & Xia, Y.N. The Effects of Size, Shape, and Surface Functional Group of Gold Nanostructures on Their Adsorption and Internalization by Cells. *Small* **6**, 517-522 (2010).

25. Cho, E.C., Xie, J.W., Wurm, P.A. & Xia, Y.N. Understanding the Role of Surface Charges in Cellular Adsorption versus Internalization by Selectively Removing Gold Nanoparticles on the Cell Surface with a I-2/KI Etchant. *Nano Lett* **9**, 1080-1084 (2009).

26. Sreerama, N., Venyaminov, S.Y. & Woody, R.W. Estimation of protein secondary structure from circular dichroism spectra: Inclusion of denatured proteins with native proteins in the analysis. *Anal Biochem* **287**, 243-251 (2000).

27. Whitmore, L. & Wallace, B.A. DICHROWEB, an online server for protein secondary structure analyses from circular dichroism spectroscopic data. *Nucleic Acids Res* **32**, W668-W673 (2004).

28. Sreerama, N. & Woody, R.W. Estimation of protein secondary structure from circular dichroism spectra: Comparison of CONTIN, SELCON, and CDSSTR methods with an expanded reference set. *Anal Biochem* **287**, 252-260 (2000).

29. Rodriguez, P.L. et al. Minimal "Self" Peptides That Inhibit Phagocytic Clearance and Enhance Delivery of Nanoparticles. *Science* **339**, 971-975 (2013).

Chapter 5: Biodistribution and Clearance of Gold Loaded Polymeric Micelles Using 0.9 and 5 nm Gold Nanoparticles

5.1 Abstract

Long-circulating gold nanoparticles (AuNPs) have garnered a great deal of interest as both imaging and therapeutic agents. However, their protracted elimination and long-term persistence within many organ systems remains a concern for clinical translation. To improve the excretion of long-circulating nanoparticles, we prepared ~80 nm biodegradable polymeric micelles with 0.9 nm or 5 nm AuNPs tightly packed within the hydrophobic core. These gold-loaded polymeric micelles (GPMs) were expected to allow for improved excretion of gold, compared with single large AuNPs, owing to the smaller size and larger surface-to-volume ratio of the individual AuNPs within the micelle. Following intravenous administration of GPMs, organs were harvested and examined for gold content using inductively coupled plasma optical emission spectrometry (ICP-OES) for up to 3 months post-injection. While both GPM formulations showed significant clearance of gold over time, micelles containing 0.9 nm AuNPs showed a 72% and 67% reduction in gold content in the liver and spleen, respectively, between 1 day and 3 months post-injection, compared with a 38% and 35% reduction in mice receiving 5 nm GPMs. Furthermore, feces and urine analysis revealed approximately 7.5 and 100 times more gold, respectively, in mice that received 0.9 nm

GPMs one day after injection. These findings suggest that the excretion profile of inorganic nanomaterials may be improved if clusters of small inorganic materials are used in favor of single solid particles.

5.2 Introduction

The use of gold nanoparticles (AuNPs) in biological applications began in 1971 when Faulk and Taylor invented the immunogold staining procedure for electron microscopy.[1] Since then, AuNPs have attracted considerable interest across a wide range of biomedical applications. For example, AuNPs have been utilized for catalysis, biosensors, cancer imaging, photothermal therapy, and drug delivery.[2, 3] The widespread interest in using AuNPs for imaging and therapeutic applications stems from their ability to be finely tuned to many different shapes and sizes, ease of surface modification, unique optical properties, high attenuation coefficient, and the strong evidence indicating that gold is nontoxic.[4, 5] In fact, aurothiolate and colloidal gold have historically been used in medical practice as a treatment for rheumatoid arthritis.[6]

Despite the beneficial aspects of using AuNPs in biomedical applications, a major lingering concern with their clinical translation is their long-term retention within many organ systems, most notably the liver and spleen. For example, it has been found that there is only a 9% drop in the content of gold in the liver from day 1 to 6 months, following the intravenous injection of 40nm AuNPs.[7] This is consistent with a number of similar studies, which saw little to no clearance of ~ 20 nm AuNPs over shorter time periods (1 to 4 months).[8, 9] As these inorganic particles are not readily biodegradable, they can potentially result in liver and immune system damage,[10] raising concerns about their long term toxicity and biosafety.[11, 12] Previous studies have shown that whole-body

clearance can be improved through the use of small AuNPs (< 6 nm), since these particles are small enough to undergo glomerular filtration.[10, 13, 14] However, smaller AuNPs possess lower blood residence times due to their rapid renal excretion.[15] As a result, they are expected to be less favorable as blood pool agents for computed tomography (CT) angiography and for tumor targeting via enhanced permeability and retention, where nanoparticle accumulation is generally governed by blood residence time.[16, 17] Moreover, larger AuNPs are also expected to be superior for receptor-targeted imaging/therapeutic studies, whereby the number of localized nanoparticles is limited by the number of cell surface receptors at the target site. Therefore, larger AuNPs would presumably allow for higher total accumulation of gold.

In this study, we examined whether a AuNP formulation could be prepared that is above the size threshold for renal clearance, but still exhibit favorable tissue clearance and excretion profiles. Specifically, we prepared ~80 nm gold-loaded polymeric micelles (GPMs) with sub-6 nm AuNPs tightly packed within the hydrophobic core (Figure 5.2 A, B). The blood clearance profile, tissue biodistribution, and excretion of gold was evaluated over a 3 month time period. Blood chemistry as well as liver and spleen histology were also examined for indications of toxicity.

5.3 Materials and Methods

Synthesis of 0.9 nm gold AuNPs

Dodecanethiol-capped 0.9nm AuNPs were prepared through the reduction of gold chloride triphenylphospine ($AuClPPh_3$) with tert-butylamine-borane ($C_4H_{14}BN$), according to the procedure described by Li *et. al*.[18] Briefly, 0.375 mmol of $AuClPPh_3$ was added to 21 mL of ethanol at room temperature. The resultant mixture was stirred and 3.75 mmol of the tert-butylamine-borane reducing agent was added. After 30 minutes, 48µL of dodecanethiol was added and the dark brown solution was stirred for at least an hour. The solvent was then evaporated in a vacuum centrifuge and the particles were resuspended in toluene followed by centrifugation to remove any insoluble material. This was repeated twice.

Synthesis of 5 nm gold AuNPs

Dodecanethiol-capped 5nm AuNPs were prepared using a two-phase reduction of tetrachloroaurate ($HAuCl_4$) with sodium borohydride ($NaBH_4$), followed by the addition of an alkanethiol, according to the procedure described by Brust et al.[19] Briefly, 25mL of an aqueous solution of 35mM hydrogen $HAuCl_4$ was mixed with 50 mM of tetraoctylammonium bromide (TOAB) in 70 mL of toluene. The solution was stirred until the $HAuCl_4$ solution transferred into the organic phase. This was followed by the drop-

wise addition of a 0.4 M aqueous solution of $NaBH_4$. Then, 0.84 mM of dodecanethiol was added to the solution while stirring. The resultant mixture was then stirred for at least 3 hours and precipitated twice at -20°C in ethanol overnight to remove excess thiols. The precipitate was collected *via* centrifugation and the supernatant was decanted. The remaining pellet was dissolved in toluene.

Synthesis of GPMs

Gold-loaded polymeric micelles were synthesized using oil-in-water emulsions and stabilized using the amphiphilic diblock copolymer polyethylene glycol (4k) – polycaprolactone (3k) (PEG-*b*-PCL).[17] AuNPs, either 0.9nm or 5nm, were dissolved in toluene at 40 mg Au/mL and PEG-*b*-PCL was also dissolved in toluene at a concentration of 40 mg/mL. A combined solution (200 μL) of the diblock (4 mg) and the AuNPs (4 mg) was added directly to a glass vial containing 4mL of dH_2O and the mixture was emulsified for approximately 3 minutes in an ultrasonic bath. The emulsions were then allowed to stand overnight in a desiccator prior to their characterization and purification. The resulting dark brown (0.9 nm) / dark purple (5 nm) solution was centrifuged at 400 RCF for 10 minutes to remove the largest micelles. The solution was then centrifuged twice at 3100 RCF for 30 minutes, after which the supernatant was removed, and the pellet was re-suspended in pH 7.4 phosphate buffered saline (PBS). Free polymer and smaller sized particles were removed by diafiltration using a MidGee hoop cross flow cartridge with 750 kDa molecular weight cutoff (GE Healthcare, Piscataway, NJ, USA). The GPMs were then filtered through a 0.2 μm cellulose acetate membrane filter (Nalgene, Thermo Scientific) to remove any oversized particles. Finally the nanoparticles

were concentrated using 50 kDa MWCO centrifugal filter units (Millipore, Billercia, MA, USA). The gold concentration was determined by inductively coupled plasma optimal emission spectroscopy (ICP-OES, Spectro Analytical Instruments GMBH; Kleve, Germany).

Tissue distribution and blood clearance

Thirty-six nude mice (n = 18 per group) were injected intravenously under anesthesia with 75 nm GPMs (containing either 0.9nm or 5nm AuNPs) in PBS at dose of 150 mg Au/kg body weight and then bled and sacrificed at various times after the injection of the agent. Specifically, three mice from each group was bled at 1 h, 2 h, 6 h, 12 h, 24 h, 3 d, 7 d, 14 d, 1 mo, and 3 mo, and the blood collected and analyzed for gold by ICP-OES. Each mouse was bled twice. Therefore, 10 uL blood samples were collected via the tail-nick method from three animals at the following times: 1 hour and 3 days, 2 hours and 7 days, 6 hours and 14 days, 24 hours and 1 month, and 1 hour and 3 months. At the second bleed time point, the mice were euthanized by CO_2 and 0.3 mL blood was removed by cardiac puncture from the right ventricle immediately after the cessation of breathing. After the final aliquot of blood was collected the brain, heart, lungs, kidneys, spleen, liver, skin, small bowel, large bowel, pancreas, thyroid, femur, and inguinal lymph nodes were removed from each animal. Three additional mice per GPM formulation were used for three additional blood collections at 5 minutes, 10 minutes, and 15 minutes and sacrificed at 24 hours and organs harvested. Organ samples were washed with PBS to minimize contamination from any nanoparticles still circulating in the blood. The blood samples and organs were then analyzed for gold content by ICP-

OES. Organ samples were weighed into Teflon PFA vials (Savillex, Minnetonka, MN, USA) and digested overnight at 60°C with 70% nitric acid to digest the organic material. HCl was added the next day and the digest continued to dissolve the inorganic material. Blood samples were dissolved directly in aqua regia. Blood GPM content was calculated as the percent of the injected dose per gram of blood analyzed (%ID/g). Organ GPM content was similarly calculated as the percent of the injected dose present per gram of tissue.

Toxicity studies

Blood samples obtained by cardiac puncture were analyzed for blood chemistry analytes (alanine aminotransferase (ALT), aspartate aminotransferase (AST), alkaline phosphatase, and total bilirubin(TBIL). All samples were analyzed by the diagnostic core laboratories at the University of Pennsylvania School of Veterinary Medicine

Hematoxylin and eosin (H&E) staining

Hematoxylin-eosin (HE) staining was performed using 5 μm thickness sections from formalin-fixed, paraffin-embedded tissue blocks. Specimens were fixed in formalin (Fisher Scientific, Waltham, MA) immediately after harvesting and followed by gradient dehydration with 70%, 95%, and 100% ethanol. Tissue were then processed in xylene (Fisher) and embedded in paraplast tissue embedding medium (Fisher). Slides were prepared using Microm HM550. Paraffin sections were deparaffinized in xylene followed by rehydration with 100%, 95%, 70% ethanol and then Milli-Q water (Millipore, Bedford, MA) before the staining. Harris hematoxylin (Fisher) was used for nuclei

staining. Excess hematoxylin was removed by dipping slides in acid alcohol (Leica Biosystems, Richmond, VA). Slides were then placed in running warm water until the nuclei turned blue. Eosin (Leica Biosystems) was used to stain for cytoplasm. Slides were later mounted using permount (Fisher) after clearing with xylene.

5.4 Results and Discussion

Characterization of 0.9 and 5 nm AuNPs

Hydrophobic AuNPs with dodecanethiol as a capping agent were prepared with low polydisperity and diameters of 0.93 ± 0.19 and 4.66 ± 0.57 nm, respectively, according to an analysis of transmission electron microscopy (TEM) images (Figure 5.1). Purity was further confirmed *via* UV–vis spectroscopy Figure 5.1).

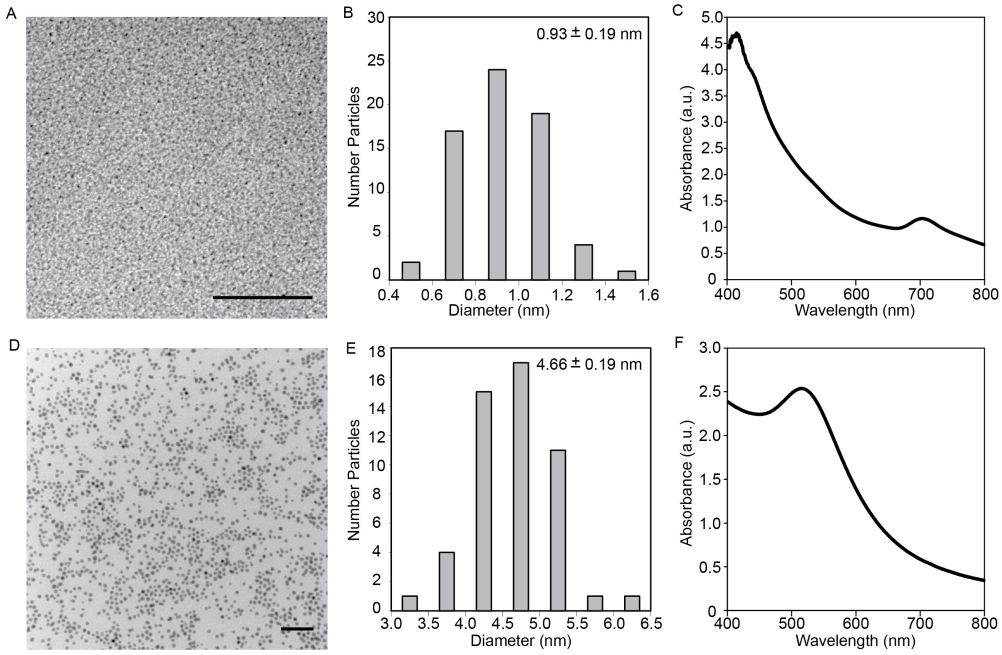

Figure 5.1. (A) Transmission electron micrograph of 0.9 nm AuNPs. Scale bar is 20 nm. (B) Core size distribution of 0.9 nm AuNPs. The mean size and standard deviation is shown. (C) UV-vis absorption spectrum of 0.9 nm AuNPs. (D) Transmission electron micrograph of 5 nm AuNPs. Scale bar is 20 nm. (E) Core size distribution of 5 nm AuNPs. The mean size and standard deviation is shown. (F) UV-vis absorption spectrum of 5 nm AuNPs.

Synthesis and Characterization of GPMs

GPMs were prepared by encapsulating either 0.9 or 5 nm AuNPs within the

diblock copolymer PEG-*b*-PCL, using a microemulsion method described previously.[17] These GPMs were soluble in aqueous solutions owing to the hydrophilic PEG corona of the diblock copolymer. Following synthesis and purification of the GPMs, ~ 80 nm GPMs were collected using differential centrifugation, as confirmed by dynamic light scattering (DLS) (Figure 5.2 C). The DLS measurements demonstrate particle measurements with a low polydispersity index for both GPM formulations (< 0.1). TEM was used to determine the morphology of the GPMs and the packing of AuNPs within the hydrophobic core. TEM micrographs revealed spherical GPMs with tightly packed clusters of AuNPs contained within the hydrophobic core of the micelles (Figure 5.2 D,E). The zeta potential of the various GPM formulations was near neutral. A summary of the GPM physical-chemical properties is provided in Table 5.1.

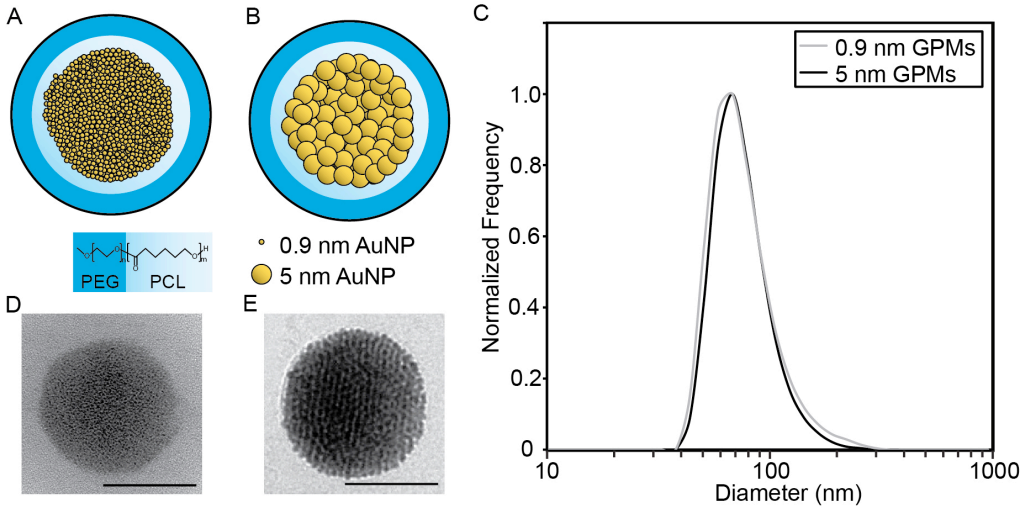

Figure 5.2. Schematic and size analysis of GPMs. Schematic of (A) 0.9 nm GPMs and (B) 5 nm GPMs. Both GPM formulations consist of AuNPs encapsulated within the hydrophobic core of micelles formed using the biodegradable diblock co-polymer PEG-b-PCL. (C) Dynamic light scattering profiles of 0.9 nm and 5 nm GPMs. Representative transmission electron microscopy (TEM) images of a (D) 0.9 nm and (E) 5 nm GPM. All scale bars = 100 nm.

Table 5.1. GPM physical-chemical properties

AuNP size (nm)	Hydrodynamic diameter (nm)	Polydispersity index	Zeta potential (mV)
0.9	79.8 ± 3.9	0.083	-1.5 ± 1.10
5	78.5 ± 2.4	0.075	-1.04 ± 0.84

GPM Pharmacokinetics

Following intravenous administration, 0.9 and 5 nm GPMs exhibited similar blood clearance profiles with circulation half-lives of ~ 1.5 hours and ~ 2.6 hours, respectively (Figure 5.3).

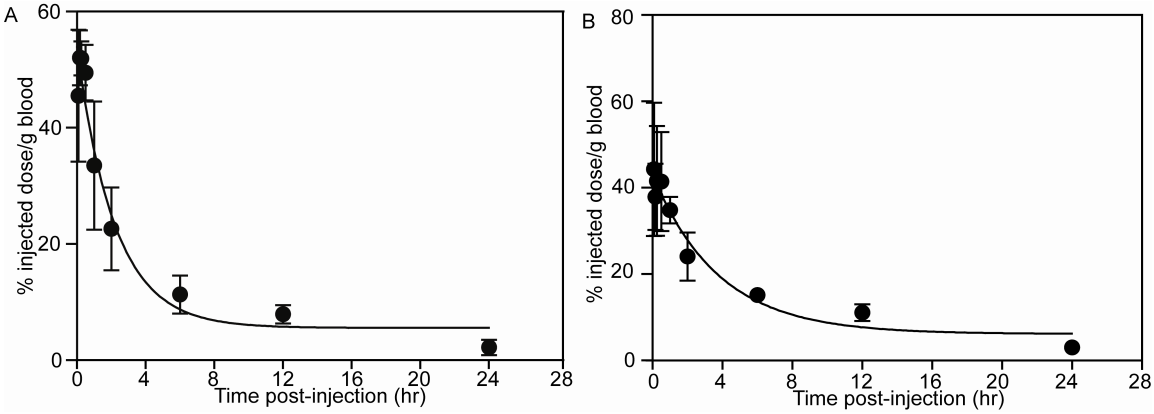

Figure 5.3. (A-B) Blood clearance profile using ICP-OES analysis of gold content in blood at various times following the intravenous administration of (A) 0.9 nm GPMs and (B) 5 nm GPM in mice (n = 3).

The biodistribution of GPMs was evaluated at 1 day, 3 days, 1 week, 2 weeks, 1 month, and 3 months post-injection (150 mg Au/kg) by performing an inductively coupled plasma–optical emission spectroscopy (ICP-OES) analysis of gold content within the brain, thyroid, lungs, heart, liver, spleen, small bowel, large bowel, kidneys,

pancreas, sublingual lymph nodes, skin, bone, muscles, feces, and urine. As expected, the largest fractions of gold were observed in the spleen and liver (Figure 5.4).

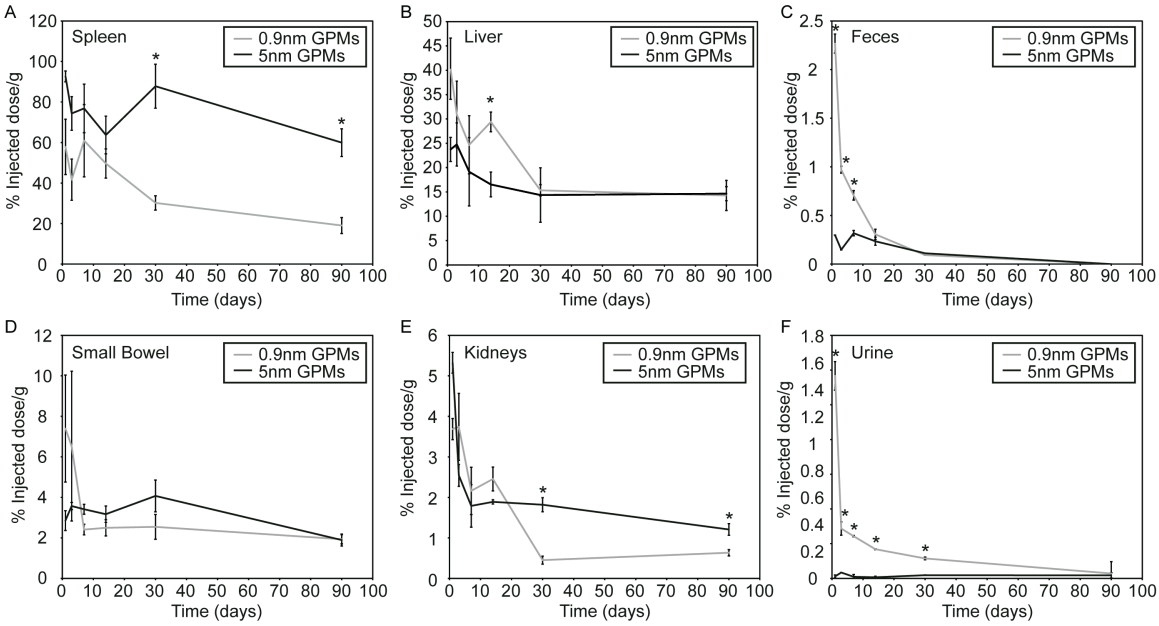

Figure 5.4. Measurement of gold content in primary excretory organs and waste. The percent injected dose of gold per gram of tissue was measured in the (A) spleen, (B) liver, (C) feces, (D) small bowel, (E) kidneys and (F) urine at various times following the intravenous administration of 0.9 nm and 5 nm GPMs. All measurements of gold were acquired via ICP-OES. Asterisk indicates statistical significance ($p < 0.05$) between 0.9 nm GPM and 5 nm GPM groups.

Higher levels of gold were observed in the spleen following intravenous injection of the 5 nm GPMs, compared with the 0.9 nm GPMs, for all time points studied. However, both groups showed a marked reduction in gold accumulation between one day and three months post-injection. Specifically, there was a 35% reduction of gold in the spleen of mice that received 5 nm GPMs and a 55% reduction of gold in the spleen of mice that received 0.9 nm GPMs.

Initially, the levels of Au within the liver were higher for the 0.9 nm GPM group (40.3 ± 6.3 %ID/g), compared with the 5 nm GPM group (23.7 ± 2.5%ID/g). However,

after 3 months the Au content dropped more dramatically in mice that received the 0.9 nm GPMs (65%) compared to the 5 nm GPMs (38%). As a result, the 0.9nm GPMs group (14.3 ± 1.5 %ID/g) and 5 nm GPMs group (14.7 ± 1.4 %ID/g) had similar levels of gold retained in the liver at this later time point.

Hepatobiliary excretion appeared to be the primary pathway for gold removal, with measureable levels of gold detected in the feces following injection of both 0.9 nm and 5 nm GPMs. However, this excretion pathway appeared to be significantly more efficient for the 0.9 nm GPMs, compared to the 5 nm GPMs, with approximately 7.5 times more gold detected in the feces one day post-injection. For both groups, the gold content in the feces decreased over the duration of the study with no detectable levels at 3 months.

Consistent with the more efficient removal of gold from 0.9 nm GPMs via the hepatobiliary system, qualitatively higher levels of gold were also found in the small bowel, although not statistically significant, one day and 3 days post-injection, compared with mice receiving 5 nm GPMs. By one week and at all subsequent time points, similar levels of gold were observed in the small bowels for both GPM formulations. Evidence of hepatobiliary excretion is consistent with previous studies, which have shown that 17 nm AuNPs that are taken up by Kupffer cells and hepatocytes are secreted primarily by hepatocytes within the first 24 hours through the hepatobiliary pathway, after which they are cleared through Kupffer cells through mechanisms that are poorly understood.[20, 21]

The quantity of gold found in the kidneys was far lower than what was found in the liver and spleen for both the 0.9 nm and 5 nm GPM groups. This is not surprising considering that GPMS are too large to undergo glomerular filtration. It was anticipated

that the GPMs would be predominantly taken up by the reticuloendothelial system (RES) prior to breakdown of the polymeric micelle and release of the encapsulated AuNPs. Nonetheless, a measureable amount of gold was detected in the kidneys, with statistically significant lower levels of gold found one day, 1 month and 3 months post-injection of the 0.9 nm GPMs, compared with 5 nm GPMs. This difference was most pronounced at the later two time points. Interestingly, there also seemed to be some renal excretion of gold from mice that received 0.9 nm GPMs. In fact, approximately 100-fold more gold was detected in the urine one day following the administration of 0.9 nm GPMs (0.29 % ID/g) compared with 5 nm GPMs (0.003 % ID/g). These urine concentrations gradually decreased to undetectable levels at 3 months. We attribute the difference between the two GPM formulations to be a direct result of the difference in the sizes of encapsulated AuNPs. Since 0.9 nm AuNPs are much smaller than the size cut-off limit for successful glomerular filtration, even if opsonized, they should enjoy more efficient excretion into the urine than the larger 5 nm AuNPs.

Two organs that appeared to exhibit somewhat surprising levels of gold following the injection of the 5 nm GPMs were the brain and heart (Figure 5.5). Specifically, in the brain we detected 2.8 ± 0.3 %ID/g one day post-injection, compared with only 0.14 ± 0.03% ID/g for 0.9 nm GPMs. Although not high per se, this level of gold is readily measureable. Nonetheless, it is likely that gold from the 5 nm GPMs did not penetrate the blood-brain barrier considering their large size and that levels of gold were at or near the detection limit after just one week post-injection. Gold would presumably not be cleared from brain in such a short timeframe if it has entered the brain parenchyma. The presence of gold does not seem to be an artifact since it was found to be at similar levels in all of

the mice at one and three days post-injection. Notably, others have also reported the presence of low levels of AuNPs (15 nm and 50 nm) in brain 24 hrs after intravenous injection.[22]

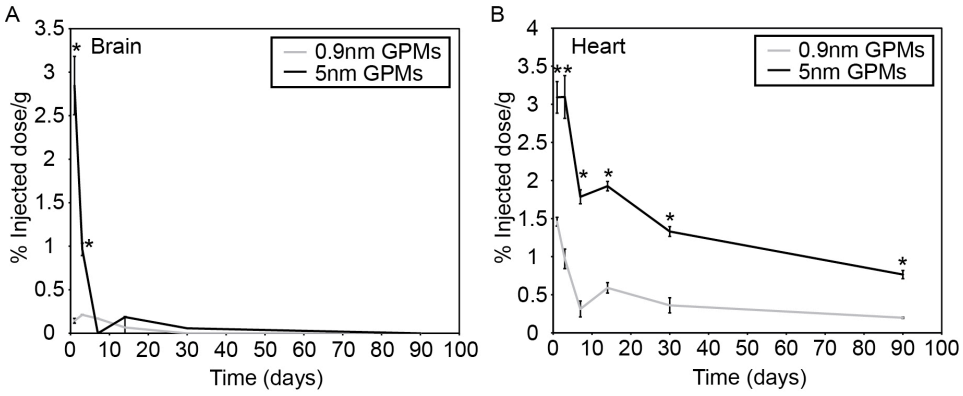

Figure 5.5. Measurement of gold content in the brain and heart. The percent injected dose of gold per gram of tissue was measured in the (A) brain and (B) heart at various times following the intravenous administration of 0.9 nm and 5 nm GPMs. All measurements of gold were acquired via ICP-OES. Asterisk indicates statistical significance ($p < 0.05$) between 0.9 nm GPM and 5 nm GPM groups.

In the heart, the gold content was 2 times greater one day following the administration of 5 nm GPMs (3.1 ± 0.2 %ID/g) compared with 0.9 nm GPMs (1.5 ± .06 %ID/g). Both groups showed a reduction in gold content (75% for 5 nm GPMs and 86% for 0.9 nm GPMs) in the heart over 3 months, however, mice receiving 5 nm GPMs possessed higher levels of gold at all time points.

In the skin, the gold content fluctuated between 2 and 12 %ID/g (on average) during the duration of the studies with no statistically significant differences between the 0.9 nm and 5 nm GPMs during the 3 month time period (Figure 5.6). The skin has long been shown to be an important site of accumulation for nanoparticles that are administered intravenously. Studies have shown that AuNPs can exit blood vessels in the

skin and be phagocytosed by dermal macrophages and dendritic cells.[23] As these phagocytes become saturated they begin to accumulate in the pericellular space of the dermis and subcutaneous tissue. In fact, this phenomenon was visible in the skin of mice injected with GPMs, which did have some discoloration. The distribution of GPMs in the skin of mice was heterogeneous with some areas exhibiting a dark purplish hue and other areas showing little to no change in skin color.

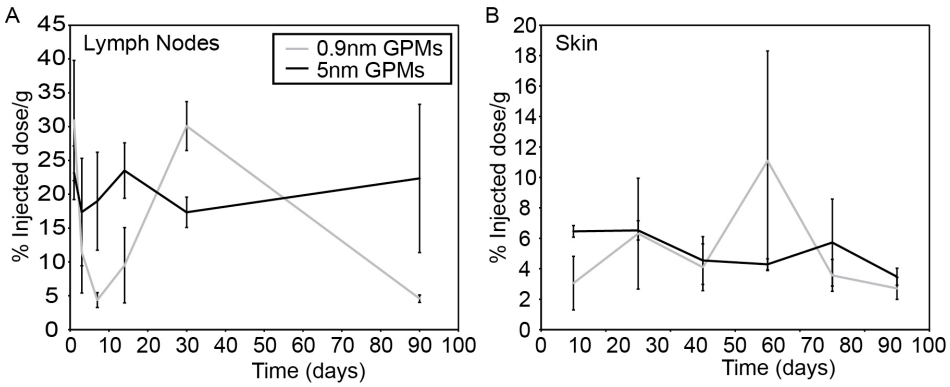

Figure 5.6. Measurement of gold content in the lymph nodes and skin. The percent injected dose of gold per gram of tissue was measured in the (A) lymph nodes and (B) skin at various times following the intravenous administration of 0.9 nm and 5 nm GPMs. All measurements of gold were acquired via ICP-OES. No statistically significant difference ($p < 0.05$) was observed between 0.9 nm and 5 nm GPM groups.

High overall levels of gold were also observed in the lymph nodes of mice following the injection of 0.9 nm and 5 nm GPMs, with levels exceeding 20 %ID/g at various time points for both groups (Figure 5.6). However, due to the high variability, no statistically significant differences were observed between the groups at any one time point. High lymph uptake was not completely unexpected considering that many studies have shown the accumulation of nanomaterials in lymph nodes, in the size range of 10 – 300 nm. [23-28] It has been postulated that nanomaterials can slowly extravasate from the

vascular to interstitial space, and are then transported to lymph nodes through the lymphatic vessels. Alternatively, it has also been suggested that nanoparticles can be taken up by the RES and trafficked to the lymph nodes.

For most of the other organs that were examined, including the thyroid, pancreas, large bowel, and muscle, there was a general trend of higher levels of gold in mice injected with 5 nm GPMs, compared with 0.9 nm GPMs (Figure 5.7). However, at most time points the differences were not statistically different and the overall levels of gold were quite low, <2.5 %ID/g (on average). Both groups showed a significant reduction in gold content over the 3-month time period in each of these organs.

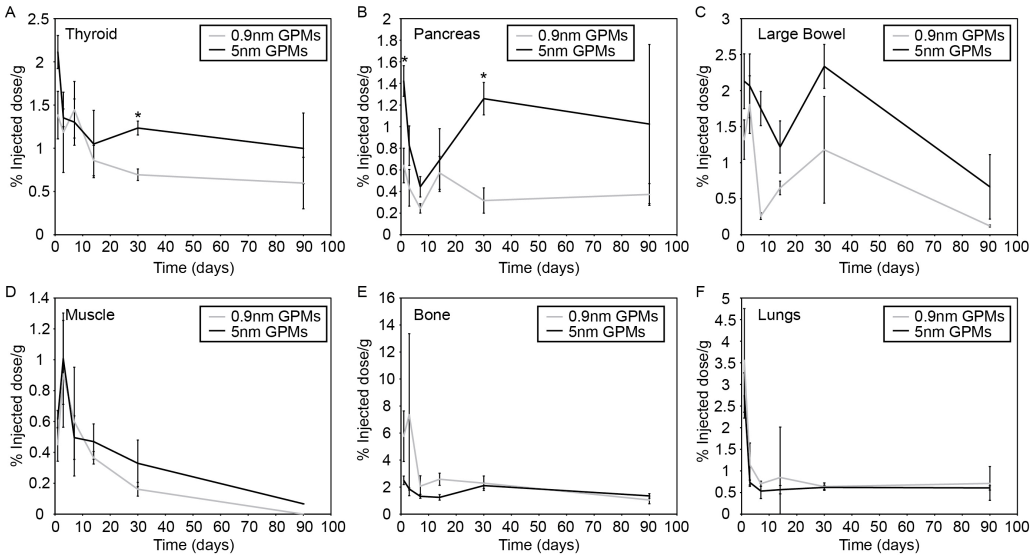

Figure 5.7. Measurement of gold content in various organs. The percent injected dose of gold per gram of tissue was measured in the (A) thyroid, (B) pancreas, (C) large bowel, (D) muscle, (E) bone and (F) lungs at various times following the intravenous administration of 0.9 nm and 5 nm GPMs. All measurements of gold were acquired via ICP-OES. Asterisk indicates statistical significance ($p < 0.05$) between 0.9 nm GPM and 5 nm GPM groups.

In bone, the levels of gold were generally higher in mice receiving 0.9 nm GPMs, particularly at early time points, but again the differences were not statistically significant (Figure 5.7). Similar levels of gold were observed in the lungs following the injection of 0.9 nm and 5 nm GPMs for all time points (Figure 5.7). A significant reduction in gold was observed in both bone and lungs following the injection of 0.9 nm and 5 nm GPMs.

Toxicity Analysis

The intravenous injection of 0.9 nm and 5 nm GPMs into healthy mice led to no signs of illness, change in activity, or weight loss (Figure 5.8). A toxicological analysis of mice 1 day, 1 week, 1 month and 3 months following the administration of GPMs revealed blood chemistry levels within normal limits, despite being highly variable (Figure 5.9). It should be noted that enzyme levels can fluctuate due to the method and rate of blood collection, time of day in which blood was collected, and level of animal physical activity and are therefore highly variable in nature.[23]

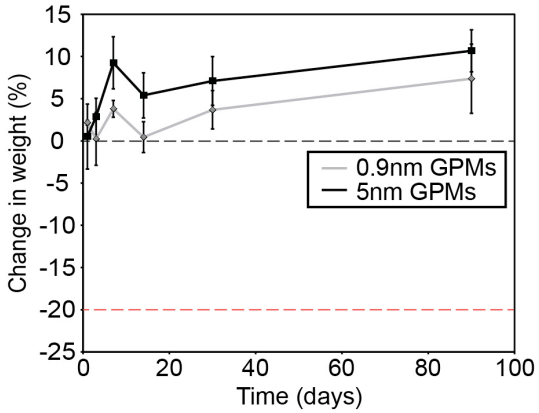

Figure 5.8. Whole animal weights of mice treated with 0.9 nm or 5 nm GPMs (150 mg Au/kg). Data reflect average weights (n = 3) for each group.

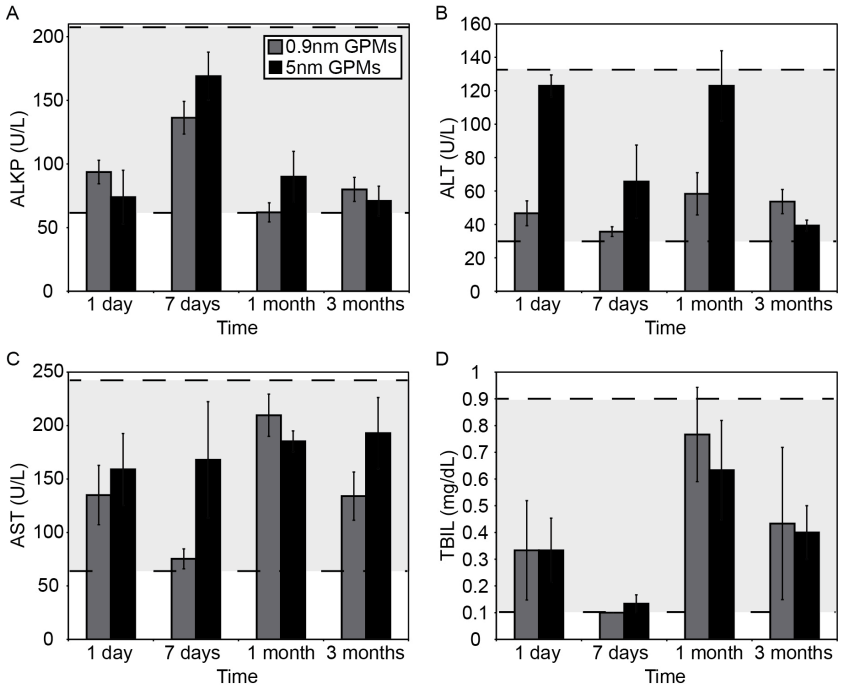

Figure 5.9. Hematological analysis of mice treated with GPMs. Blood enzyme levels of female nude athymic mice were acquired 1 day, 7 days, 1 month, and 3 months days post-injection of 150 mg Au/kg of 0.9 nm GPMs (grey) or 5 nm GPM (black). Grey dotted lines denote the "normal" analyte levels. The specific enzymes analyzed were (A) alkaline phosphatase (ALKP), (B) alanine transaminase (ALT), (C) aspartate aminotransferase (AST), and (D) total bilirubin (TBIL).

Histology of liver and spleen

To further evaluate the potential toxicity of GPMs, histological analysis was performed on the liver and spleen 1 day, 1 week, 1 month, and 3 months following the injection of 0.9 nm and 5 nm GPMs. Hematoxylin and eosin (H&E) stains of these organs showed no evidence of abnormal pathology or adverse effects (Figure 5.10). These results are consistent with previously established literature touting the safety profile of AuNPs.[11, 29-34]

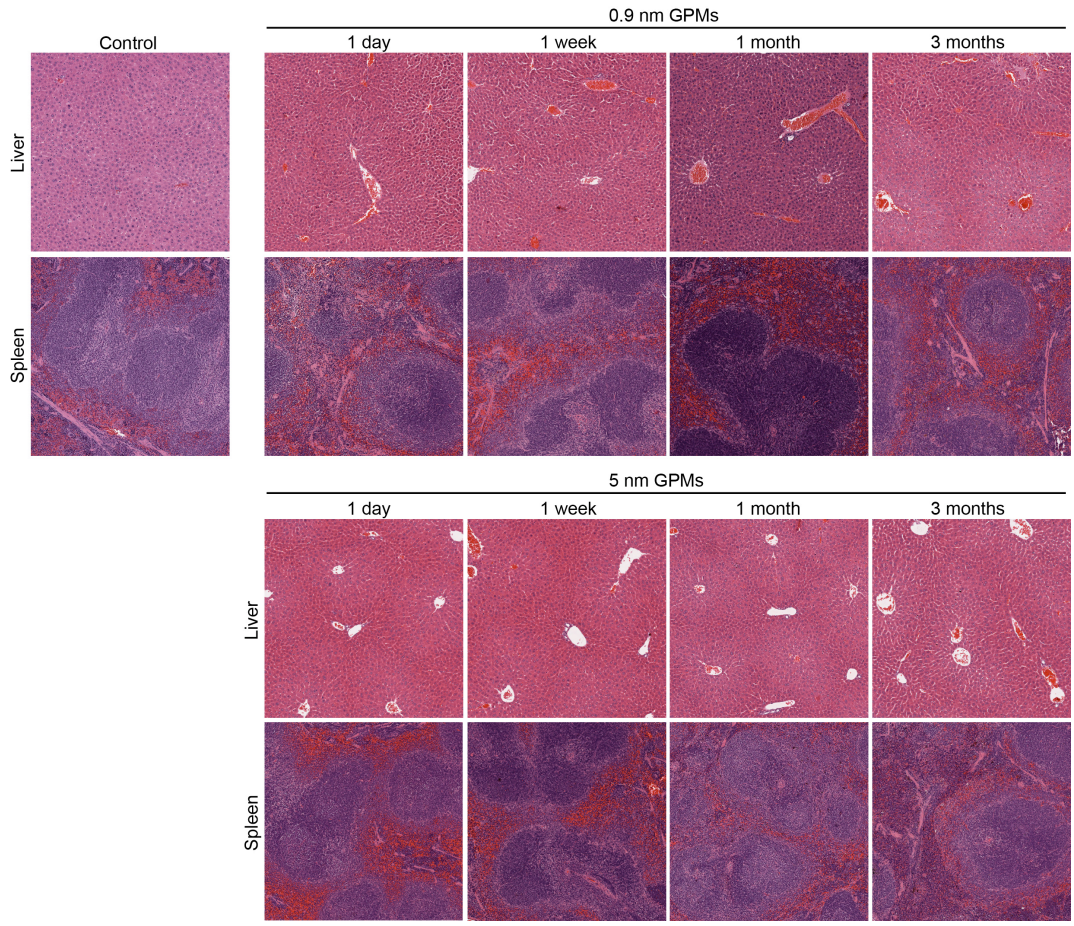

Figure 5.10. Histological of liver and spleen for mice treated with GPMs. Mice (n=3 per group) received a single intravenous injection of 0.2 mL of either PBS (control), 0.9 nm GPMs, or 5 nm GPMs (150 mg Au/kg dose in PBS) followed by dissection of the liver and spleen at the indicated times. Sections were stained with H&E and images were acquired via light microscopy at 10x magnification.

5.5 Conclusions

Numerous reports have indicated that AuNPs are poorly cleared from the reticuloendothelial system following intravenous administration. For example, Balasubramanian et al showed that in rats injected with 20 nm PEG AuNPs, gold levels in the liver and spleen remain high even at 2 months follow up (6 % reduction in gold).[8] In another study by Sadauskas et al, analysis of livers in mice injected with 40 nm AuNPs resulted in only a modest 9% reduction in gold content over a 6-month time period.[7] Goel et al found that the gold content in the liver was reduced by approximately 50% following the injection of 33 nm PEG AuNPs, but that levels of gold in the spleen remained essentially unchanged 3 months post-injection.[9] In this study we investigated the organ distribution and retention of GPMs, which consist of clusters of 0.9 or 5 nm AuNPs encapsulated within the hydrophobic micelle core, for up to three months post-injection. As expected, accumulation was highest in organs rich in macrophages (liver, spleen, lymph nodes). However, in contrast to the many studies that report inefficient clearance and a persistent accumulation of AuNPs within the reticuloendothelial system, we observed a 65% and 55% reduction in gold content in the liver and spleen, respectively, between 1 day and 3 months following the injection of 0.9 nm GPMs. A 38% and 35% reduction in gold content was observed in the liver and spleen, respectively, following injection of 5 nm GPMs. A reduction of gold in most other organs was observed as well. The primary mechanism of excretion seemed to be via the hepatobiliary systems, although some renal clearance was also observed. In general, GPMs containing 0.9 nm AuNPs seemed to exhibit more efficient excretion compared to 5 nm GPMs, with higher levels of gold detected in the feces and urine at earlier time

points (1 – 7 days). Both the 0.9 nm and 5 nm GPMs were found to be biocompatible with no evidence of toxicity as measured by blood chemistry, loss in body weight, signs of distress, and histological analysis of liver and spleen tissue sections. Overall, these findings suggest that the excretion profile of inorganic nanomaterials may be improved if nanoparticles formed from clusters of small inorganic materials are used in favor of single solid particles.

5.6 References

1. Faulk, W.P. & Taylor, G.M. An immunocolloid method for the electron microscope. *Immunochemistry* **8**, 1081-1083 (1971).
2. Ulijn, R.V. & Smith, A.M. Designing peptide based nanomaterials. *Chem Soc Rev* **37**, 664-675 (2008).
3. Giljohann, D.A. et al. Gold nanoparticles for biology and medicine. *Angew Chem Int Ed Engl* **49**, 3280-3294 (2010).
4. Jeremic, B., Aguerri, A.R. & Filipovic, N. Radiosensitization by gold nanoparticles. *Clin Transl Oncol* **15**, 593-601 (2013).
5. Dorsey, J.F. et al. Gold nanoparticles in radiation research: potential applications for imaging and radiosensitization. *Transl Can Res* **2** (2013).
6. Hebert, E.M., Debouttiere, P.J., Lepage, M., Sanche, L. & Hunting, D.J. Preferential tumour accumulation of gold nanoparticles, visualised by Magnetic Resonance Imaging: radiosensitisation studies in vivo and in vitro. *Int J Radiat Biol* **86**, 692-700 (2010).
7. Sadauskas, E. et al. Protracted elimination of gold nanoparticles from mouse liver. *Nanomedicine* **5**, 162-169 (2009).
8. Balasubramanian, S.K. et al. Biodistribution of gold nanoparticles and gene expression changes in the liver and spleen after intravenous administration in rats. *Biomaterials* **31**, 2034-2042 (2010).
9. Goel, R., Shah, N., Visaria, R., Paciotti, G.F. & Bischof, J.C. Biodistribution of TNF-alpha-coated gold nanoparticles in an in vivo model system. *Nanomedicine (Lond)* **4**, 401-410 (2009).

10. De Jong, W.H. et al. Particle size-dependent organ distribution of gold nanoparticles after intravenous administration. *Biomaterials* **29**, 1912-1919 (2008).

11. Lewinski, N., Colvin, V. & Drezek, R. Cytotoxicity of nanoparticles. *Small* **4**, 26-49 (2008).

12. Shichibu, Y., Negishi, Y., Tsukuda, T. & Teranishi, T. Large-scale synthesis of thiolated Au25 clusters via ligand exchange reactions of phosphine-stabilized Au11 clusters. *J Am Chem Soc* **127**, 13464-13465 (2005).

13. Sadauskas, E. et al. Kupffer cells are central in the removal of nanoparticles from the organism. *Part Fibre Toxicol* **4**, 10 (2007).

14. Semmler-Behnke, M. et al. Biodistribution of 1.4- and 18-nm gold particles in rats. *Small* **4**, 2108-2111 (2008).

15. Hainfeld, J.F., Slatkin, D.N., Focella, T.M. & Smilowitz, H.M. Gold nanoparticles: a new X-ray contrast agent. *Br J Radiol* **79**, 248-253 (2006).

16. Tam, J.M. et al. Controlled assembly of biodegradable plasmonic nanoclusters for near-infrared imaging and therapeutic applications. *ACS Nano* **4**, 2178-2184 (2010).

17. Al Zaki, A. et al. Gold-loaded polymeric micelles for computed tomography-guided radiation therapy treatment and radiosensitization. *ACS Nano* **8**, 104-112 (2014).

18. Li, Y. et al. Controllable synthesis of gold nanoparticles with ultrasmall size and high monodispersity via continuous supplement of precursor. *Dalton Trans* **41**, 11725-11730 (2012).

19. Brust, M., Walker, M., Bethell, D., Schiffrin, D.J. & Whyman, R. Synthesis of Thiol-Derivatized Gold Nanoparticles in a 2-phase Liquid-Liquid System. *J. Chem. Soc. Chem. Commun.*, 801 (1994).

20. Hardonk, M.J., Harms, G. & Koudstaal, J. Zonal heterogeneity of rat hepatocytes in the in vivo uptake of 17 nm colloidal gold granules. *Histochemistry* **83**, 473-477 (1985).

21. Paciotti, G.F. et al. Colloidal gold: a novel nanoparticle vector for tumor directed drug delivery. *Drug Deliv* **11**, 169-183 (2004).

22. Sonavane, G., Tomoda, K. & Makino, K. Biodistribution of colloidal gold nanoparticles after intravenous administration: effect of particle size. *Colloids Surf B Biointerfaces* **66**, 274-280 (2008).

23. Sykes, E.A., Dai, Q., Tsoi, K.M., Hwang, D.M. & Chan, W.C. Nanoparticle exposure in animals can be visualized in the skin and analysed via skin biopsy. *Nat Commun* **5**, 3796 (2014).

24. Weissleder, R., Nahrendorf, M. & Pittet, M.J. Imaging macrophages with nanoparticles. *Nat Mater* **13**, 125-138 (2014).

25. Harisinghani, M.G. et al. Noninvasive detection of clinically occult lymph-node metastases in prostate cancer. *N Engl J Med* **348**, 2491-2499 (2003).

26. Thorek, D.L. et al. Non-invasive mapping of deep-tissue lymph nodes in live animals using a multimodal PET/MRI nanoparticle. *Nat Commun* **5**, 3097 (2014).

27. Garnett, M.C. & Kallinteri, P. Nanomedicines and nanotoxicology: some physiological principles. *Occup Med (Lond)* **56**, 307-311 (2006).

28. Oh, M.H. et al. Large-scale synthesis of bioinert tantalum oxide nanoparticles for X-ray computed tomography imaging and bimodal image-guided sentinel lymph node mapping. *J Am Chem Soc* **133**, 5508-5515 (2011).

29. Tkachenko, A.G. et al. Multifunctional gold nanoparticle-peptide complexes for nuclear targeting. *J Am Chem Soc* **125**, 4700-4701 (2003).

30. Shukla, R. et al. Biocompatibility of gold nanoparticles and their endocytotic fate inside the cellular compartment: a microscopic overview. *Langmuir* **21**, 10644-10654 (2005).

31. Pan, Y. et al. Size-dependent cytotoxicity of gold nanoparticles. *Small* **3**, 1941-1949 (2007).

32. Connor, E.E., Mwamuka, J., Gole, A., Murphy, C.J. & Wyatt, M.D. Gold nanoparticles are taken up by human cells but do not cause acute cytotoxicity. *Small* **1**, 325-327 (2005).

33. Chen, P.C., Mwakwari, S.C. & Oyelere, A.K. Gold nanoparticles: From nanomedicine to nanosensing. *Nanotechnol Sci Appl* **1**, 45-65 (2008).

34. Lasagna-Reeves, C. et al. Bioaccumulation and toxicity of gold nanoparticles after repeated administration in mice. *Biochem Biophys Res Commun* **393**, 649-655 (2010).

Chapter 6: Summary Discussion, Future Directions and Concluding Remarks

6.1 Summary Discussion

6.1.1 GPMs for CT Imaging and Radiation Enhancement

Due to their unique physical, chemical and optical properties, AuNPs have been proposed for use in many diverse biomedical applications including biosensors, photo-responsive agents, drug delivery vehicles, and therapeutic agents.[1] Furthermore, the high electron density and atomic number of gold nanoparticles has proven to be valuable for electron and X-ray attenuation. Initially proposed by Hainfeld et al.,[2] the intravenous administration of AuNPs has been shown to provide blood pool contrast enhancement in X-ray imaging. Since then many studies have used AuNPs as contrast agents for X-ray imaging including metabolic disorders,[3] malignancies,[4] and cardiovascular diseases.[5] However, a limitation of Hainfeld's study is the rapid clearance of AuNPs, which can limit EPR driven accumulation necessary for successful contrast enhanced tumor imaging. We have shown that by encapsulating small AuNPs within micelles, we can significantly improve the nanoparticle blood circulation time as compared to single AuNPs and potentially improve AuNP elimination. Furthermore, this enhanced circulation was visible in CT images with GPMs remaining in the bloodstream for a much longer duration. The advantage of prolonging nanoparticle blood residence time is to increase the accumulation of nanoparticles within the tumor. When the nanoparticles first enter the tumor circulation, a small percentage will exit the vasculature due to the EPR effect while the majority will remain in the systemic circulation. The longer the

nanoparticles remain in the circulation, the higher the probability that more particles will permeate across the leaky tumor vasculature and enter the tumor interstitium. Indeed, this was shown in CT images of tumor bearing mice where gold mediated contrast was clearly visible in mice administered GPMs but not in mice receiving single 1.9 nm AuNPs. This GPM enhanced CT image was used to guide the delivery of a single 6 Gy dose of X-ray radiation therapy that yielded improved survival when compared to non-irradiated and irradiated controls. These results are truly exciting as they have the potential to spare normal healthy tissue on two fronts. First, the use of contrast enhanced image guided radiation therapy could provide a more accurate morphological representation of tumor geometry and margins for maximizing therapeutic delivery within the lesion. Second, the use of AuNPs as radiation enhancing agents could reduce the overall dose required for complete tumor eradication, and therefore reduce the exposure of adjacent healthy tissues to further radiation.

6.1.2 GSMs for MR Imaging and Radiation Enhancement

The main motivation for introducing superparamagnetic iron oxide nanoparticles (SPIO) into our micelles was the apparent mismatch between the GPM dose needed for radiation enhancement and the lower detection limit of GPMs via CT. In our GPM *in vitro* studies, we observed approximately a 2.2 fold increase in DNA-DSBs as well as a decrease in cell survival at Au concentration of 0.1 mg/ml. However, the minimum concentration of Au that can be detected using CT imaging is approximately 0.5 mg/ml. This five-fold difference in concentration means that large doses of Au are required to provide sufficient tumor contrast for guiding radiation therapy, and that the concentration of Au within the tumor exceeds the 0.1 mg/ml needed for effective radiosensitization.

The incorporation of SPIO nanoparticles with AuNPs in micelles enabled contrast enhanced imaging using MRI. As a result, MRI and CT phantoms of GSMs showed a sixty six fold improvement in sensitivity using MR. Furthremore, *in vivo* imaging demonstrated that while no tumor contrast enhancement was observed using CT imaging, MRI contrast was clearly visible producing a hypointense image within the tumor.

For each group of animals receiving radiation therapy, an MR image was acquired both pre-injection and twenty-four hours after injection of GSM prior to the administration of radiation. Intriguingly, the amount of tumor contrast generated on T_2 weighted MR imaging correlated linearly with the rate of tumor reduction therapy after therapy meaning that those tumors with the most MR contrast exhibited higher reductions in tumor volume post therapy. While image contrast did correlate with tumor response, there was no correlation with overall survival. A likely explanation could be that some cancer cells may have been excluded from the treatment volume resulting in a repopulation of cells and tumor relapse. Furthermore, as a result of the heterogeneous distribution of nanoparticles in the tumor, some areas within the tumor may experience more radiation enhancement than others resulting in differential cell death. Moreover, alternate factors that are most likely excluded during fractionation including phase of cell cycle, and tumor oxygenation may play a role in tumor recurrence.

6.1.3 GPMs for Enhanced Clearance and Improved Pharmacokinetics

A major limitation for nanoparticle technologies is their poor elimination profiles, especially for particles larger than 6 nm, which is believed to be the size cut off for successful renal clearance. Large sized particles are retained primarily in organ systems

that are particularly high in macrophages such as the liver, spleen, bones, lymph nodes, and skin. For gold, as these particles are not biodegradable, they remain there for extended periods without significant reduction in gold content. In this thesis, our approach was to form polymeric micelles with small AuNPs (0.9 and 5 nm) in their core. We evaluated various organs for gold content up to three months, while regularly measuring blood chemistries, weight changes, and monitoring for any signs of toxicity. In contrast to many other documented studies, we saw a reduction over time in many organs including the liver and the spleen. For both particle sizes, gold was detected in feces suggesting the hepatobiliary pathway to be involved in particle excretion. Furthermore, smaller AuNPs showed superior clearance to larger AuNPs with higher gold contents measured in the feces during early time-points. Similarly, in the urine, gold was detected only in mice administered 0.9 nm GPMs at very early time-points. Therefore, the use of sub-nanometer particles within micelles can facilitate gold excretion via the liver in the feces and kidneys at early time-points. It is important to note that very little or no gold was detected in the feces or urine at three months showing that gold excretion reaches a plateau at this timepoint. While AuNPs were not completely eliminated at the end of the study, there was significant reduction of gold content in the RES compared to other studies evaluating the biodistribution of AuNPs.

6.1.4 Targeted Iron Oxide Nanoparticle Oleosin Micelles

Thus far, both GPM and GSM particles used for our *in vivo* evaluations consisted of a pegylated, hydrophilic corona and relied on passive targeting, i.e. nonspecific accumulation within tumors through the EPR effect. Although some tumors may experience high permeability, multiple passes through the circulation are needed for a

substantial amount of nanoparticles to enter tumor tissue. Therefore, a critical criteria for successful passive delivery is the design of nanoparticles with long *in vivo* circulation times. Furthermore, passive targeting is non-specific relying heavily on high vascular permeability and poor lymphatic drainage at the tumor site. In contrast, active targeting arises from the direct interaction of targeting ligands with specific receptors on cancer cells. While initially receptor targeted particles are also dependent on the EPR effect for tumor penetration, there are several key advantages for targeted agents including higher tumor retention, the ability to facilitate nanoparticle internalization for improved efficacy, and improved tumor specificity. Our approach was to use a naturally occurring surfactant protein oleosin to stabilize SPIO nanoparticles. These particles displayed high r_2 relaxivity and showed cell specific targeting in cells overexpressing the Her2/neu receptor. In addition, a major advantage of this platform compared to other targeted particles is the ability to develop functionalized particles in a single step by blending in a Her2 affibody-oleosin mutant.

6.2 Future Directions

6.2.1 Improving CT Sensitivity for Molecular Imaging

For molecular and tumor imaging, a fundamental limitation of using AuNPs as CT contrast agents is the low sensitivity detection limit of X-rays compared to other imaging modalities. Specifically, studies have shown that the detection limit of gold is approximately 0.5 mg/ml. This is orders of magnitudes higher when compared to other imaging modalities such as MRI and PET. In order to overcome the sensitivity limitations of CT, highly concentrated doses need to be administered. In addition, although AuNPs attenuate X-rays better than conventionally used iodinated contrast agents, the cost of

using gold is a huge obstacle for their clinical utilization. However, recent improvements in CT technology such as multicolor spectral CT have shown that molecular imaging using CT may be possible.[5] This technique enables the simultaneous detection of multiple elements by distributing incident X-rays into various energy bins enabling significantly lower concentrations of AuNPs to be administered. Another imaging strategy to improve contrast is to use dual energy X-ray imaging that increases the signal intensity of imaging agents by the removal of the soft-tissue signal variation in the background. This is obtained by subtracting the images obtained at two energy levels that flank the k-edge of the contrast material.

6.2.2 Fractionated Studies Using GPMs and GSMs

Although there are some scenarios during which a single radiation dose exceeds 2 Gy (high grade gliomas),[6] most conventional radiation therapy treatment regimens are generally divided into multiple sessions with doses usually not exceeding 1.8 – 2 Gy. To our knowledge, there are currently no documented studies examining the radiosensitization effects of AuNPs that are administered during fractionated radiation therapy. Therefore, it would be valuable to compare the benefits AuNPs with sub-therapeutic doses of radiation therapy.

The administration of radiation to blood vessels has been shown to increase endothelial permeability.[6] This strategy could be adapted to our studies such that sub-therapeutic doses of radiation are applied to tumor volumes in order to disrupt tumor vasculature thereby increasing nanoparticle penetration for subsequent radiation therapy. AuNPs can either be injected prior to or right after the first few fractions of radiation therapy. The advantage of administering AuNPs prior to the initiation of fractionated

radiation therapy is that they can provide tumor contrast for assisting image guided and enhanced radiation therapy. However, the application of AuNPs after the first fraction of radiation would increase nanoparticle tumor accumulation, thereby increasing AuNPs mediated radiosensitization during subsequent fractions.

Lastly, most studies including our own demonstrate improved dose enhancement and radiosensitization in the less clinically relevant kilovoltage energy ranges. While a handful of studies have shown some improvement in the radiation enhancement effects at megavoltage energies, the exact mechanisms of sensitization are largely unknown. Therefore, further studies need to be carried out at these energies in order to examine the therapeutic benefits of AuNP mediated cytotoxicity.

6.2.3 *In Vivo* Use of GSMs for Evaluating Tumor Physiology

Therapeutic response is an important subject in the management of cancer patients. While some malignancies may be responsive to anticancer agents, a majority of them will relapse increasing their resistance to first line therapies. These resistances are governed by mutations in cancer cells that can alter their phenotype and expression profiles. Moreover, some regions of tumors may be poorly visible on imaging or have limited access through the blood supply for successful distribution of agents. As a result, therapies are often costly, time consuming, and unsuccessful with huge burdens on patients.

Through MR imaging, we found a direct correlation between extent of tumor contrast and response to radiation therapy. While the most likely explanation for this effect is due to the increased accumulation of nanoparticles, there are also other potential causes. Since there is heterogeneity in the vascular supply and permeability of blood

vessels supplying tumors, one must consider this to be a key barrier that limits the successful delivery of intravenously administered agents to tumor cells. In fact, we observed this in our animal studies with some tumors showing more nanoparticle accumulation than others. Increased tumor permeability to particles can also mean increased tumor oxygenation. As mentioned in the introduction section, hypoxia is a significant contributor to tumor radioresistance. With this in mind, tumors exhibiting substantial nanoparticle accumulation may experience some free radical generation from the presence of oxygen in addition to photoelectrons generated from nearby nanoparticles. Therefore the use of MR imaging, particularly nanoparticle mediated contrast enhancement, can provide some insight on tumor vascularization, permeability, oxygenation, and the likelihood to be responsive to specific therapies. This approach can be extended to other forms of cancer therapy to provide information of drug accumulation at tumor sites.

6.2.4 Improved Clearance Using Novel AuNPs

Since a micelle nanoplatform can carry a payload of small AuNPs, it can significantly increase the particle size to prolong blood circulation and avoid renal clearance. We have already seen that using smaller AuNPs can help enhance total body excretion. However despite using sub-nanometer AuNPs, there are still a number of improvements to be made using this nanoparticle formulation since gold within the organs was not completely eliminated, and levels of gold in both urine and feces were essentially undetectable at later time point. Although, this study has shown significant clearance of AuNPs over 3 months, the hydrophobic coating present on the surface of the nanoparticles may limit their complete removal. An alternative strategy would be to

develop sub-nanometer AuNPs that transition from hydrophobic to hydrophilic. Initially, these particles would be hydrophobic enabling the successful encapsulation of gold into the hydrophobic core of the micelle. However, as these cells are internalized, and experience a low pH environment within lysosomes, the biodegradable coating will be hydrolyzed exposing the hydrophobic AuNPs. These AuNPs will become water-soluble within acidic lysosomes. Once dispersed, their small size will render the individual AuNPs susceptible to excretion by glomerular filtration and/or more readily degraded by lysosomal enzymes. Alternatively, nanoformulations can be developed that can incorporate hydrophilic AuNPs directly. Previous studies have shown that AuNPs can be assembled into clusters using weakly adsorbing biodegradable triblock copolymers.[7] Once the polymer is degraded, the nanclusters can deaggregate into individual AuNPs to facilitate clearance.

6.2.5 *In Vivo* Targeting of Iron Oxide Oleosin Micelles

While we have successfully demonstrated cell specific targeting of iron micelles to cancer cells *in vitro*, a more thorough biological investigation is warranted *in vivo*. Since the protein oleosin is easily modifiable, alterations in the surface charge and appending specific stealth ligand (CD47) to the particles could engineer nanoparticles to be less immunogenic and nontoxic while maintaining long circulation times.[8] The amino acid sequence of the oleosin protein can also by modified such that particle formation and stability are improved. Further modifications to the nanoparticle surface could improve targeting. For example, the density of targeting ligand on the surface of the nanoparticle is a major determinant of cell specific binding.[9] Therefore, optimizations of ligand density will likely improve nanoparticle targeting capabilities. Linkers between oleosin

and the ligand can also be introduced to reduce the steric hindrance of targeting agents and maximize ligand receptor interactions.

6.3 Concluding Remarks

During the past decades, advancements in the field of radiation therapy have revolutionized the process of cancer treatment. New technologies that enable accurate tumor segmentation, dose specific deliveries, and specific tumoricidal agents have contributed significantly to maximizing therapeutic doses only to intended tissues. In the future, we envision a nanoplatform that can be used to actively target cancer cells via ligand-receptor mediated interactions, provide tumor specific contrast for image guided radiation therapy and prognostic information, and that is effectively cleared from both systemic circulation as well as the reiculoendothelial system. Further improvements to increase tumor specific targeting and biological clearance would inevitably facilitate the translatability of nanodevices to the clinic.

6.4 References

1. Dykman, L. & Khlebtsov, N. Gold nanoparticles in biomedical applications: recent advances and perspectives. *Chem Soc Rev* 41, 2256-2282 (2012).
2. Hainfeld, J.F., Slatkin, D.N., Focella, T.M. & Smilowitz, H.M. Gold nanoparticles: a new X-ray contrast agent. *Br J Radiol* 79, 248-253 (2006).
3. Aydogan, B. et al. AuNP-DG: deoxyglucose-labeled gold nanoparticles as X-ray computed tomography contrast agents for cancer imaging. *Mol Imaging Biol* 12, 463-467 (2010).
4. Popovtzer, R. et al. Targeted gold nanoparticles enable molecular CT imaging of cancer. *Nano Lett* 8, 4593-4596 (2008).
5. Cormode, D.P. et al. Atherosclerotic plaque composition: analysis with multicolor CT and targeted gold nanoparticles. *Radiology* 256, 774-782 (2010).
6. Joh, D.Y. et al. Selective targeting of brain tumors with gold nanoparticle-induced radiosensitization. *PLoS One* 8, e62425 (2013).
7. Tam, J.M. et al. Controlled assembly of biodegradable plasmonic nanoclusters for near-infrared imaging and therapeutic applications. *ACS Nano* 4, 2178-2184 (2010).
8. Rodriguez, P.L. et al. Minimal "Self" peptides that inhibit phagocytic clearance and enhance delivery of nanoparticles. *Science* 339, 971-975 (2013).
9. Elias, D.R., Poloukhtine, A., Popik, V. & Tsourkas, A. Effect of ligand density, receptor density, and nanoparticle size on cell targeting. *Nanomedicine* 9, 194-201 (2013).